Investigating the triggering mechanisms of palaeoceanographic disturbance across the Frasnian–Famennian, Late Permian and the Paleocene–Eocene Thermal Maximum: insights from osmium isotopes and geochemistry

ZEYANG LIU

Investigating the triggering mechanisms of palaeoceanographic disturbance across the Frasnian–Famennian, Late Permian and the Paleocene–Eocene Thermal Maximum: insights from osmium isotopes and geochemistry

Zeyang Liu

刘泽阳

St John's College

A thesis submitted in partial fulfilment of the requirements for the degree of Doctor of Philosophy at

Durham University

Department of Earth Sciences, Durham University

June, 2019

Abstract

This thesis utilizes osmium (Os) isotope, together with other geochemical proxies, to investigate the paleoclimate and palaeoceanography of three Earth history intervals: the Wuchiapingian–Changhsing boundary (WCB), the Frasnian–Famennian (F–F) boundary and the Paleocene–Eocene (P–E) boundary.

High-resolution Os isotope chemostratigraphy of four globally correlated WCB sections show two separate Os isotope excursions to less radiogenic compositions that are coincident with the carbon isotope excursions (CIEs). The Os isotope shift is interpreted to reflect increased unradiogenic Os input from basaltic magmatism in South China, possibly related to the Emeishan large igneous province. Volcanism may have provided the isotopically light carbon that drove the negative carbon isotope excursions across the WCB.

Organic petrology, Os isotope stratigraphy, major and trace element analyses, and programmed pyrolysis analysis from five F–F sections from western New York, USA show evidence of a wildfire event at the F–F boundary and yield an estimated pO_2 level of ~25% for the Late Devonian. Furthermore, the Os isotope records does not support an extra-terrestrial impact or volcanic event as a trigger for the F–F mass extinction. The inferred high O_2 level supports the hypothesis that pCO_2 drawdown and climate cooling may have caused the F–F mass extinction.

A multiproxy geochemical study (Os isotope, mercury, sulfur, platinum group elements) on two P–E boundary North Atlantic Ocean records suggests that both a comet impact and major volcanic activity likely contributed to the environmental perturbations during the P–E interval. Approximately 0.4 Gt of carbon is estimated to have been derived from the comet, thus the impact cannot have been responsible for the full manifestation of the P–E CIE. Other sources of carbon may have jointly driven the P–E thermal maximum. Climate simulations indicate that stratospheric sulfate aerosols from the impact may have caused transient cooling and reduced precipitation prior to the onset of substantial P–E warming.

Contents

List of Figures

Declaration

I declare that this thesis, which I submit for the degree of Doctor of Philosophy at Durham University, is my own work and not substantially the same as any which has previously been submitted at this or any other university.

Zeyang Liu

St John's College

Durham University

2019

Acknowledgement

I would like to thank my supervisors Prof. David Selby and Prof. Chris Greenwell. In particular, I would like to thank Prof. David Selby for his academic and financial support. He always gave me a quick response to my questions and constantly encourage me to think independently. He is indeed an excellent supervisor.

I would like to thank Shuzhong Shen, Hua Zhang, Bradley Sageman, Lawrence Percival, Jeffrey Over, Clay Tabor, Daniel Horton, Ben Gill, Steve Grasby for supporting my study. I would like to thank Paul Hackley for mentoring my organic petrology work in the USGS. I would also like to thank David Bausman and Sandra Clark for hosting my stay in Reston when I was doing lab work at the USGS. It was always a nice experience every time I visited you.

I would like to thank my friends and colleagues in Durham. In particular, I would like to thank Wenyan Luo, Yang Li, Junjie Liu, Li Li, Xiang Ge, Yufeng Cui, and Guang Hu. I would like to thank the rest of the Selby group and the lab staff for making the lab a nice place to work. I would also like to thank the supporting staff in Earth Science department and Durham University.

I would like to thank the funding bodies for my PhD study: Durham University, China Scholarship Council, the Geological Society of London, the Society of Organic Petrology, Universities' China Committee in London, St John's college of Durham University, Nature and Environment Research Council, and Prof. David Selby. None of my research would have been possible without their financial support.

Last but not least, I would like to thank my parents. I wouldn't have been here without their support through all these years.

Chapter 1

Introduction

The Earth experienced several catastrophic events during its evolution history, such as ocean anoxic events, snowball glaciations, meteorite impact events, hydrothermal pulses and synchronous/associated mass extinctions (Bond and Grasby, 2017). Many isotope systems in seawater are sensitive to the processes mentioned above, making them a powerful toolbox to reconstruct paleoclimate and paleoceanography. Of these isotope systems, the rhenium-osmium (Re–Os) isotope system has been widely applied to the understanding of earth processes. The Os isotope composition ($^{187}Os/^{188}Os$) of seawater reflects the balance of radiogenic input from weathering of the ancient continent (~1.4) and unradiogenic inputs from mantle and extraterrestrial sources (~0.13) (Peucker-Ehrenbrink and Ravizza, 2000). The short residence time of seawater osmium (≤ 50 kyrs; Rooney et al., 2016) provides the ability of osmium isotopes to track changes on seawater chemistry across short time intervals (few 100 kyrs) to assess the isotope composition temporal relationship to global events. The osmium isotope tool has provide vital information about multiple Earth system processes throughout geological history, such as: volcanism (Cohen and Coe, 2002; Du Vivier et al., 2014; Ravizza and Peucker-Ehrenbrink, 2003; Turgeon and Creaser, 2008), glaciation/ snowball Earth events (Finlay et al., 2010; Rooney et al., 2016), hydrothermal events and weathering (Dickson et al., 2015; Ravizza et al., 2001; Schmitz et al., 2004; Wieczorek et al., 2013), basin connectivity (Poirier and Hillaire-Marcel, 2009), and meteorite impacts (Paquay et al., 2008).

In this thesis, Osmium isotope stratigraphy, coupled with other proxies, is applied to study the paleoclimate and paleoceanography changes of three critical time intervals in Earth history: the Frasnian–Famennian boundary (~372 Ma, Late Devonian; Percival et al., 2018), the Wuchiapingian–Changhsingian boundary (~254 Ma, Late Permian; Shen et al., 2019), and

the Paleocene–Eocene boundary (~55.9 Ma, Early Paleogene; Charles et al., 2011). In Chapter 2, the Re–Os isotope systematics are used to investigate the mechanisms causing the carbon isotope excursions around the Wuchiapingian–Changhsingian boundary. In Chapter 3, the Re–Os isotope tool, together with organic petrology, programmed pyrolysis, total organic carbon (TOC) and major and trace elements are used to investigate the atmospheric oxygen (O_2) level during Late Devonian and possible mechanisms that caused the mass extinction at the Frasnian–Famennian boundary. In Chapter 4, the Re–Os isotope system, coupled with platinum group elements (PGEs: Ir-Pt-Pd-Ru), mercury (Hg), pyrite sulfur (S) and TOC, is applied to examine the possible roles of volcanism and meteorite impact in driving the climate perturbations during the Paleocene–Eocene boundary. An Earth system model (Community Earth System Model, CESM) is also used to simulate climate fluctuations around the Paleocene–Eocene boundary related to a meteorite impact.

1.1 Carbon isotope perturbations and biotic crises during Middle–Late Permian

Three large carbon isotope excursions (CIEs) are detected during Middle–Late Permian: the Guadalupian–Lopingian boundary (~259 Ma), the Wuchiapingian–Changhsingian boundary (~254 Ma) and the Permian–Triassic boundary (~251 Ma) (Shen et al., 2019). Both the Permian–Triassic boundary and the Guadalupian–Lopingian boundary are associated with volcanism and severe biotic crises (Shen et al., 2013b). The large negative CIE in both carbonate ($\delta^{13}C_{carb}$) and organic matter ($\delta^{13}C_{org}$) is globally documented within the interval immediately below the Permian–Triassic boundary (Korte and Kozur, 2010). This CIE is interpreted to be driven by degassing of CO_2 from widespread volcanism in Siberia and South China (Payne and Kump, 2007; Shen et al., 2013a; Svensen et al., 2009) and/or associated carbon release from sedimentary strata (Saunders and Reichow, 2009; Shen et al., 2011). The negative CIE of the Guadalupian–Lopingian boundary is documented at several sections (e.g., South China, Iran, Spitsbergen) (Bond et al., 2015; Jin et al., 2006a; Shen et al., 2013b; Wang

et al., 2004; Wignall et al., 2009). This CIE coincides with the main phase of the Emeishan volcanism in South China, and is associated with the end-Guadalupian mass extinction (Wignall, 2001; Wignall et al., 2009).

Distinctive negative CIEs across the WCB interval are observed in several sections including South China (Bagherpour et al., 2018; Bai et al., 2008; Jin et al., 2006b; Shao et al., 2000; Shen et al., 2013b; Shen et al., 2010; Wei et al., 2015; Ye and Jiang, 2016), Iran (Liu et al., 2013; Shen et al., 2013b) and the Canadian Arctic (Beauchamp et al., 2009). However, currently there is no geologic or biotic event known during this time interval and the mechanism causing this CIE is still unclear (Shao et al., 2000; Shen et al., 2013b; Wei et al., 2015). To further investigate the mechanisms that caused the WCB CIE, Os isotope stratigraphy is applied on four Wuchiapingian–Changhsingian boundary sections.

Chapter 2 presents Os isotope stratigraphy of three sections in South China (Lianyuan, Meishan and Shangsi) and one section in the Canadian Arctic (Buchanan Lake), together with carbon isotope stratigraphy. These profiles record two pulses of unradiogenic Os_i shifts that correlate with the carbon isotope excursions. The Os isotope excursions are interpreted to be driven by regional scale volcanism and that the small extent of the volcanism explains why there is no mass extinction event during this time interval. This study also demonstrates the ability of osmium isotope to investigate the scale of historical volcanism.

All sample preparation, laboratory work, data collection and evaluation for the Re-Os geochronology study was carried out by the author. Professor Bradly B. Sageman carried out the organic carbon isotope analysis at the Northwestern University. The chapter was written by the author with professor Selby providing editorial comments and suggestions. A version of this chapter is currently in review in Earth and Planetary Science Letters, co-authored by David Selby of Durham University, Hua Zhang and Quanfeng Zheng of China Academy of

Science, Shuzhong Shen of Nanjing University, Stephen E. Grasby of Canadian Geological Survey, and Benoit Beauchamp of University of Calgary.

1.2 O_2 level during Late Devonian and the Frasnian–Famennian mass extinction

The level of atmospheric O_2 is considered to have fluctuated significantly as a result of the diversification and radiation of terrestrial plant during the Devonian Period (Dahl et al., 2010). Reconstructions of the O_2 level throughout Earth's history have been made with geochemical models of carbon and sulfur cycling (Berner, 2006; Berner, 2009; Berner et al., 2003). However, these models vary widely in the Late Devonian time. The O_2 levels are estimated to have dropped from ~25 % to ~13 % during the Devonian and then steadily rose again, achieving present atmospheric levels (21 %) during the mid-Mississippian Epoch (Berner, 2006; Rimmer et al., 2015; Scott and Glasspool, 2006). In contrast, other models suggest that O_2 levels dropped from ~25 % (Early Devonian) to ~17% (early Late Devonian), and then rose to ~22 % during the Late Devonian (Berner, 2009; Berner et al., 2003). Fossilized charcoal (inertinite) provides a record of wildfire events, which in turn can be used to study the ancient atmospheric O_2 levels (Glasspool and Scott, 2010; Scott and Glasspool, 2007). As no record of inertinite has been reported for the Frasnian–Famennian, despite the fuel availability as vegetation already developed (Stein et al., 2012), this period is thought to have a low pO_2 level (~13 %; Berner, 2006; Rimmer et al., 2015; Scott and Glasspool, 2006).

In addition to the fluctuation of atmospheric oxygen level, the Late Devonian also contains the Frasnian–Famennian (F–F) mass extinction, which is one of the five largest biotic crises in the Phanerozoic era (Stanley, 2016). Proposed mechanism causing this event include ocean anoxic or euxinic conditions (Bond et al., 2004), climate cooling (Huang et al., 2018; Joachimski et al., 2009; Joachimski and Buggisch, 2002), sea-level change (Bond and Wignall, 2008; Johnson et al., 1985), bolide impact (Claeys et al., 1992; Claeys and Casier, 1994), and volcanism (Racki et al., 2018).

In Chapter 3, Os isotope stratigraphy, organic petrology, total organic carbon, programmed pyrolysis, and major and trace element analyses were performed on five sections from western New York that containing the F–F boundary. Inertinite is found around the Frasnian–Famennian interval, indicating a wildfire event and a high O_2 level (~25 %) during this time. The Os isotope data does not provide support for volcanism or evidence for an impact scenario during the F–F boundary interval. Alternatively, the high O_2 level supports the hypothesis that pCO_2 drawdown and associated climate cooling may be linked with the Frasnian–Famennian mass extinction event.

All sample preparation, laboratory work, data collection and evaluation for the Re–Os analysis was carried out by the author. Organic petrology work was carried by the author at USGS (Reston, Virginia) under the supervision of Paul C. Hackley. Programmed pyrolysis and TOC analyses were carried out by Augusta Warden at USGS lab in Denver, Colorado. Major and trace element analyses were carried out by the author, with the samples prepared at the Department of Archaeology and analysed at the Department of Geography of Durham University. The chapter was written by the author with professor Selby providing editorial comments and suggestions. A version of this chapter is currently in review in Earth and Planetary Science Letters, co-authored by David Selby of Durham University, Paul C. Hackley of USGS and D. Jeffrey Over of State University of New York at Geneseo.

1.3 The Paleocene–Eocene thermal maximum

The Paleocene–Eocene thermal maximum (PETM) is characterized by large negative carbon isotope excursions caused by the injection of large amounts of isotopically light carbon (≥ 3,000–10,000 Gt) in to the ocean and atmosphere, rapidly escalating the global temperature (Gingerich, 2003; Gutjahr et al., 2017; Schmitz and Pujalte, 2003; Wing et al., 2005; Wright and Schaller, 2013; Zachos et al., 2001; Zeebe et al., 2009). Commonly proposed sources of the carbon include volcanic degassing related to the emplacement of the North Atlantic Igneous

Province (NAIP; Saunders, 2016; Gutjahr et al. 2017), thermal alteration of organic-rich sedimentary rocks by intrusions of magmatic sills (Svensen et al., 2004), melting of gas hydrates and/or permafrost (Dickens et al., 1995; DeConto et al., 2012), and weathering of marine sedimentary organic matter (Higgins and Schrag, 2006). In previous studies, small magnitude of osmium isotope excursions has been reported (Dickson et al., 2015; Schmitz et al., 2004; Wieczorek et al., 2013). However, due to the lack in impact evidence, all the unradiogenic excursions were linked with volcanism associated with the North Atlantic igneous province (NAIP), which has dating results overlap with the Paleocene–Eocene boundary (Charles et al., 2011; Storey et al., 2007; Svensen et al., 2010). A meteorite impact event was also proposed as a trigger for the event, based on the evidence from glass spherules (microtektites and microkrystites) and shocked-quartz found with the negative carbon isotope excursion at three P–E sections from North Atlantic Ocean (Schaller et al., 2016).

Chapter 4 investigates the potential roles of meteorite and volcanism in driving the climate perturbations during the P–E boundary. This chapter presents Os isotope, platinum group elements (Pt-Pd-Ir-Ru), mercury (Hg), TOC and pyrite S data on two North Atlantic core samples. This study suggests that both comet impact and volcanism occurred at the P–E boundary. The size of the comet is estimated to be ~3.3 km. The cometary carbon is estimated to be ~0.4 Gt and thus cannot account for the climate warming. This chapter also presents the climate simulation results of the climatic disruptions driven by the comet impact.

All sample preparation, laboratory work, data collection and evaluation for the Re–Os analysis and Platinum Group Element analysis were carried out by the author. Professor Bradley B. Sageman carried out the TOC analysis at Northwestern University. Mercury analysis was carried out by Lawrence M. E. Percival at University of Lausanne. Pyrite sulphur was analysed by Benjamin C. Gill at Virginia Polytechnic Institute and State University. Climate modelling was carried out by the author, Clay Tabor at University of Connecticut and

Dan E. Horton at Northwestern University. The chapter was written by the author with professor Selby providing editorial comments and suggestions. A version of this chapter is currently in review in Geology, co-authored by David Selby of Durham University, Lawrence M. E. Percival of University of Lausanne and Vrije Universiteit Brussel, Clay Tabor of University of Connecticut, Dan E. Horton of Northwestern University, Bradly B. Sageman of Northwestern University and Benjamin C. Gill of Virginia Polytechnic Institute and State University.

1.4 Methodology

1.4.1 Modern geochemical cycles of Re and Os

In seawater, Re exists as the perrhenate ion (ReO_4^-), which is the only significant Re species found in ocean waters (Koide et al., 1986). The Re concentration depth profile measured in the Pacific Ocean demonstrates that the behaviour of Re in the ocean is conservative (Anbar et al., 1992). The residence time of Re is estimated to be ~750 kyrs (Colodner et al., 1993). Under redox environment, Re is reduced and removed from the seawater at or below the sediment water interface (Colodner et al., 1993).

Osmium in the seawater is suggested to present as oxyanions (H_2OsO_5 or $H_3OsO_6^-$) or organically complexed (Peucker-Ehrenbrink and Ravizza, 2000). The present-day seawater $^{187}Os/^{188}Os$ value (~1.06) reflects the balance of radiogenic input from weathering of ancient continent (~1.4) and unradiogenic input from mantle-derived sources (~0.13) of Os (Peucker-Ehrenbrink and Ravizza, 2000). Unradiogenic input from the dissolution of the background flux of extraterrestrial matter is considered to be negligible (~30,000 t yr^{-1}: Esser and Turekian, 1993; Love and Brownlee, 1993; Peucker-Ehrenbrink, 1996). Osmium is readily removed to the sediments under anoxic or suboxic environments (Yamashita et al., 2007). Osmium is considered to exists in the sediments as Os(III) or Os(IV) and may be complexed with organic matter in the reducing sediment (Yamashita et al., 2007).

1.4.2 Re and Os analytical protocol

Before crushing, all samples (20–70 g) were polished to eliminate contamination from cutting and drilling marks. The samples were then air dried at 60 °C for ~12 hours, and broken into chips with no metal contact. Samples were crushed to a fine powder (~30 μm) in a Zirconia ceramic dish using a shatterbox. The sample analytical protocol and Re–Os isotope analysis were carried out at the Durham Geochemistry Centre (Laboratory for Sulfide and Source Rock Geochronology and Geochemistry, and Arthur Holmes Laboratory) at Durham University. Given that organic-rich sedimentary rocks have highly variable Re abundance, the Re abundance of the samples were pre-determined via ID-ICP-MS on a Thermo X-Series Mass Spectrometer prior to the full Re-Os analysis. Sample powder weights of ~ 1 g with a known amount of ^{190}Os and ^{185}Re tracer (spike) solution and 8 mL of 0.25 g/g Cr^{VI}–H_2SO_4 solution were reacted in a sealed carius tube for 48 h at 220 °C (Selby and Creaser, 2003). For sample digestion, a Cr^{VI}–H_2SO_4 solution was employed to preferentially liberate hydrogenous Re and Os from the organic matter, limiting any contamination from Re and Os in the detritus (Selby and Creaser, 2003). Osmium was purified from the acid solution using solvent extraction ($CHCl_3$) and subsequently back extracted with hydrobromic acid (HBr). After a further purification by micro-distillation (CrO_3-H_2SO_4-HBr) method, the isolated Os fractions were loaded onto clean, degassed Pt filaments for isotopic analysis using a ThermoElectron TRITON mass spectrometer with secondary electron multiplier in peak-hopping mode. Instrumental mass fractionation was corrected by internal normalisation to a $^{192}Os/^{188}Os$ ratio of 3.09202.

From the osmium extracted solution, rhenium was isolated using solvent extraction (NaOH-C_3H_6O) and then purified by anion chromatography. The isolated Re fractions were loaded onto Ni filaments. Isotopic measurements were determined using a ThermoElectron TRITON mass spectrometer with static Faraday collection. The difference between the

measured Re standard solution $^{185}Re/^{187}Re$ values and the accepted $^{185}Re/^{187}Re$ value (0.5974) is used for instrumental mass fractionation correction of the Re sample data. The initial $^{187}Os/^{188}Os$ values were calculated using the equation:

$$^{187}Os/^{188}Os_{initial} = {}^{187}Os/^{188}Os_{measured} - (^{187}Re/^{188}Os_{measured} * (EXP(\lambda * t) - 1))$$

Where λ is ^{187}Re decay constant $1.666e^{-11}a^{-1}$ (Smoliar et al., 1996) and t is the depositional age. The uncertainty of $^{187}Os/^{188}Os_i$ has been estimated from separate digestions of an in-house mudrock standard (USGS SBC–1, USGS SDO–1) as ±0.05 (in-house unpublished data, Selby 2019).

1.4.3 Trace and major elements

Aliquots of the sample powder prepared for Re–Os analysis were also used for major and trace element analysis. Major and trace elements were analysed with fused bead and pressed pellet, respectively. For the former, 0.6 g of sample powder and 6 g of flux were used to fuse the bead. The pressed pellet was prepared with 12 g of sample and 3 g of binder. Major and trace element abundance were determined using a Panalytical Zetium X–ray fluorescence (XRF) spectrometer at Department of Geography at Durham University. Reproducibility and precision were demonstrated through the repeated analysis of standards (USGS SBC–1, USGS SDO–1). Ranges of uncertainty were less than 1 % for major elements (Si, Al and Ti), less than 10 % for trace elements (Mn, Vi and Ni), and 20 % for Mo.

1.4.4 Organic petrography analysis

Crushed samples were mounted into polished circular briquettes one inch in diameter following the standard procedure of ASTM D2797 at the U.S. Geological Survey (USGS) in Reston, Virginia. The thermoset plastic briquette mount was ground and polished with successively finer abrasives until a 0.05-micrometer (μm) finishing stage. Sample briquettes were imaged under oil immersion on a Zeiss AxioImager microscope in white and blue incident light at 500x magnification. Samples were point-counted (300 – 500 points per sample) to

determine relative abundances of mineral matter and macerals, which are inertinite, solid bitumen and *Tasmanites* that presented in our sample sets. A Leica DM4000 microscope equipped with LED illumination and monochrome camera detection was used for solid bitumen reflectance analysis with the computer program DISKUS-FOSSIL by Hilgers Technisches Buero. A YAG calibration standard (0.908% Ro) from Klein and Becker was used. Solid bitumen reflectance analyses (BRo, %) were collected according to ASTM D7708. Generally, at least 20 measurements of solid bitumen reflectance were collected for each sample, with only 1 measurement per individual rock fragment. Inertinite reflectance (IRo, %) was measured with the same method as solid bitumen.

1.4.5 Total organic carbon analysis

Powdered samples were analysed for weight percent concentration of total carbon (TC) by combustion at 950 °C in a stream of O_2. Total inorganic carbon (TIC) was analysed by acidification using 10% phosphoric acid. Sample carbon converted to CO_2 by each preparation method is quantified by coulometric titration (Huffman, 1977; Engleman et al., 1985). TOC is calculated as the difference between wt% TC and TIC. The TIC value is converted to wt% calcium carbonate by stoichiometric calculation (wt% TIC × 8.333), with the assumption that negligible quantities of inorganic carbon were present as minerals other than calcium carbonate. Analysis of standards and replicates indicates average uncertainty less than ±1%.

1.5 References

Anbar, A.D., Creaser, R.A., Papanastassiou, D.A., Wasserburg, G.J., 1992. Rhenium in seawater: Confirmation of generally conservative behavior. Geochimica et Cosmochimica Acta 56, 4099-4103.

Bagherpour, B., Bucher, H., Schneebeli-Hermann, E., Vennemann, T., Chiaradia, M., Shen, S.-z., 2018. Early Late Permian coupled carbon and strontium isotope

chemostratigraphy from South China: Extended Emeishan volcanism? Gondwana Research 58, 58-70.

Bai, X., Luo, G., Wu, X., Wang, Y., Huang, J., Wang, X., 2008. Carbon Isotope Records Indicative of Paleoceanographical Events at the Latest Permian Dalong Formation at Shangsi, Northeast Sichuan, China. Journal of China University of Geosciences 19, 481-487.

Beauchamp, B., Henderson, C.M., Grasby, S.E., Gates, L.T., Beatty, T.W., Utting, J., James, N.P., 2009. Late Permian Sedimentation in the Sverdrup Basin, Canadian Arctic: The Lindstrom and Black Stripe Formations. Bulletin of Canadian Petroleum Geology 57, 167-191.

Berner, R.A., 2006. GEOCARBSULF: A combined model for Phanerozoic atmospheric O_2 and CO_2. Geochimica et Cosmochimica Acta 70, 5653-5664.

Berner, R.A., 2009. Phanerozoic atmospheric oxygen: New results using the GEOCARBSULF model. American Journal of Science 309, 603-606.

Berner, R.A., Beerling, D.J., Dudley, R., Robinson, J.M., Wildman, R.A., 2003. Phanerozoic atmospheric oxygen. Annual Review of Earth and Planetary Sciences 31, 105-134.

Bond, D., Wignall, P.B., Racki, G., 2004. Extent and duration of marine anoxia during the Frasnian–Famennian (Late Devonian) mass extinction in Poland, Germany, Austria and France. Geological Magazine 141, 173-193.

Bond, D.P.G., Grasby, S.E., 2017. On the causes of mass extinctions. Palaeogeography, Palaeoclimatology, Palaeoecology 478, 3-29.

Bond, D.P.G., Savov, I., Wignall, P.B., Joachimski, M.M., Sun, Y., Grasby, S.E., Beauchamp, B., Blomeier, D.P.G., 2015. An abrupt extinction in the Middle Permian (Capitanian) of the Boreal Realm (Spitsbergen) and its link to anoxia and acidification. GSA Bulletin 127, 1411-1421.

Bond, D.P.G., Wignall, P.B., 2008. The role of sea-level change and marine anoxia in the Frasnian–Famennian (Late Devonian) mass extinction. Palaeogeography, Palaeoclimatology, Palaeoecology 263, 107-118.

Charles, A.J., Condon, D.J., Harding, I.C., Pälike, H., Marshall, J.E.A., Cui, Y., Kump, L., Croudace, I.W., 2011. Constraints on the numerical age of the Paleocene-Eocene boundary. Geochemistry, Geophysics, Geosystems 12, n/a-n/a.

Claeys, P., Casier, J.-G., Margolis, S.V., 1992. Microtektites and Mass Extinctions: Evidence for a Late Devonian Asteroid Impact. Science 257, 1102-1104.

Claeys, P., Casier, J.G., 1994. Microtektite-like impact glass associated with the Frasnian-Famennian boundary mass extinction. Earth and Planetary Science Letters 122, 303-315.

Cohen, A.S., Coe, A.L., 2002. New geochemical evidence for the onset of volcanism in the Central Atlantic magmatic province and environmental change at the Triassic-Jurassic boundary. Geology 30, 267-270.

Colodner, D., Sachs, J., Ravizza, G., Turekian, K., Edmond, J., Boyle, E., 1993. The geochemical cycle of rhenium: a reconnaissance. Earth and Planetary Science Letters 117, 205-221.

Dahl, T.W., Hammarlund, E.U., Anbar, A.D., Bond, D.P.G., Gill, B.C., Gordon, G.W., Knoll, A.H., Nielsen, A.T., Schovsbo, N.H., Canfield, D.E., 2010. Devonian rise in atmospheric oxygen correlated to the radiations of terrestrial plants and large predatory fish. Proceedings of the National Academy of Sciences 107, 17911-17915.

DeConto, R.M., Galeotti, S., Pagani, M., Tracy, D., Schaefer, K., Zhang, T., Pollard, D., Beerling, D.J., 2012. Past extreme warming events linked to massive carbon release from thawing permafrost. Nature 484, 87.

Dickens, G.R., O'Neil, J.R., Rea, D.K., Owen, R.M., 1995. Dissociation of oceanic methane hydrate as a cause of the carbon isotope excursion at the end of the Paleocene. Paleoceanography 10, 965-971.

Dickson, A.J., Cohen, A.S., Coe, A.L., Davies, M., Shcherbinina, E.A., Gavrilov, Y.O., 2015. Evidence for weathering and volcanism during the PETM from Arctic Ocean and Peri-Tethys osmium isotope records. Palaeogeography, Palaeoclimatology, Palaeoecology 438, 300-307.

Du Vivier, A.D.C., Selby, D., Sageman, B.B., Jarvis, I., Gröcke, D.R., Voigt, S., 2014. Marine 187Os/188Os isotope stratigraphy reveals the interaction of volcanism and ocean circulation during Oceanic Anoxic Event 2. Earth and Planetary Science Letters 389, 23-33.

Engleman, E.E., Jackson, L.L., Norton, D.R., 1985. Determination of carbonate carbon in geological materials by coulometric titration. Chemical Geology 53, 125-128.

Esser, B.K., Turekian, K.K., 1993. The osmium isotopic composition of the continental crust. Geochimica et Cosmochimica Acta 57, 3093-3104.

Finlay, A.J., Selby, D., Gröcke, D.R., 2010. Tracking the Hirnantian glaciation using Os isotopes. Earth and Planetary Science Letters 293, 339-348.

Gingerich, P.D., 2003. Mammalian responses to climate change at the Paleocene-Eocene boundary: Polecat Bench record in the northern Bighorn Basin, Wyoming.

Glasspool, I.J., Scott, A.C., 2010. Phanerozoic concentrations of atmospheric oxygen reconstructed from sedimentary charcoal. Nature Geoscience 3, 627.

Gutjahr, M., Ridgwell, A., Sexton, P.F., Anagnostou, E., Pearson, P.N., Pälike, H., Norris, R.D., Thomas, E., Foster, G.L., 2017. Very large release of mostly volcanic carbon during the Palaeocene–Eocene Thermal Maximum. Nature 548, 573.

Higgins, J.A., Schrag, D.P., 2006. Beyond methane: Towards a theory for the Paleocene–Eocene Thermal Maximum. Earth and Planetary Science Letters 245, 523-537.

Huang, C., Joachimski, M.M., Gong, Y., 2018. Did climate changes trigger the Late Devonian Kellwasser Crisis? Evidence from a high-resolution conodont $\delta^{18}O_{PO4}$ record from South China. Earth and Planetary Science Letters 495, 174-184.

Huffman, E.W.D., 1977. Performance of a new automatic carbon dioxide coulometer. Microchemical Journal 22, 567-573.

Jin, Y., Shen, S., Henderson, C.M., Wang, X., Wang, W., Wang, Y., Cao, C., Shang, Q., 2006a. The Global Stratotype Section and Point (GSSP) for the boundary between the Capitanian and Wuchiapingian Stage (Permian). Episodes 29, 253-262.

Jin, Y., Wang, Y., Henderson, C., Wardlaw, B.R., Shen, S., Cao, C., 2006b. The Global Boundary Stratotype Section and Point (GSSP) for the base of Changhsingian Stage (Upper Permian). Episodes 29, 175-182.

Joachimski, M.M., Breisig, S., Buggisch, W., Talent, J.A., Mawson, R., Gereke, M., Morrow, J.R., Day, J., Weddige, K., 2009. Devonian climate and reef evolution: Insights from oxygen isotopes in apatite. Earth and Planetary Science Letters 284, 599-609.

Joachimski, M.M., Buggisch, W., 2002. Conodont apatite δ18O signatures indicate climatic cooling as a trigger of the Late Devonian mass extinction. Geology 30, 711-714.

Johnson, J.G., KLAPPER, G., SANDBERG, C.A., 1985. Devonian eustatic fluctuations in Euramerica. Geological Society of America Bulletin 96, 567-587.

Koide, M., Hodge, V.F., Yang, J.S., Stallard, M., Goldberg, E.G., Calhoun, J., Bertine, K.K., 1986. Some comparative marine chemistries of rhenium, gold, silver and molybdenum. Applied Geochemistry 1, 705-714.

Korte, C., Kozur, H.W., 2010. Carbon-isotope stratigraphy across the Permian–Triassic boundary: A review. Journal of Asian Earth Sciences 39, 215-235.

Liu, X.-c., Wang, W., Shen, S.-z., Gorgij, M.N., Ye, F.-c., Zhang, Y.-c., Furuyama, S., Kano, A., Chen, X.-z., 2013. Late Guadalupian to Lopingian (Permian) carbon and strontium isotopic chemostratigraphy in the Abadeh section, central Iran. Gondwana Research 24, 222-232.

Love, S.G., Brownlee, D.E., 1993. A Direct Measurement of the Terrestrial Mass Accretion Rate of Cosmic Dust. 262, 550-553.

Paquay, F.S., Ravizza, G.E., Dalai, T.K., Peucker-Ehrenbrink, B., 2008. Determining Chondritic Impactor Size from the Marine Osmium Isotope Record. Science 320, 214-218.

Payne, J.L., Kump, L.R., 2007. Evidence for recurrent Early Triassic massive volcanism from quantitative interpretation of carbon isotope fluctuations. Earth and Planetary Science Letters 256, 264-277.

Percival, L.M.E., Davies, J.H.F.L., Schaltegger, U., De Vleeschouwer, D., Da Silva, A.C., Föllmi, K.B., 2018. Precisely dating the Frasnian–Famennian boundary: implications for the cause of the Late Devonian mass extinction. Scientific Reports 8, 9578.

Peucker-Ehrenbrink, B., Ravizza, G., 2000. The marine osmium isotope record. Terra Nova 12, 205-219.

Peucker-Ehrenbrink, B., 1996. Accretion of extraterrestrial matter during the last 80 million years and its effect on the marine osmium isotope record. Geochimica et Cosmochimica Acta 60, 3187-3196.

Poirier, A., Hillaire-Marcel, C., 2009. Os-isotope insights into major environmental changes of the Arctic Ocean during the Cenozoic. Geophysical Research Letters 36.

Racki, G., Rakociński, M., Marynowski, L., Wignall, P.B., 2018. Mercury enrichments and the Frasnian-Famennian biotic crisis: A volcanic trigger proved? Geology 46, 543-546.

Ravizza, G., Norris, R.N., Blusztajn, J., Aubry, M.P., 2001. An osmium isotope excursion associated with the Late Paleocene thermal maximum: Evidence of intensified chemical weathering. Paleoceanography 16, 155-163.

Ravizza, G., Peucker-Ehrenbrink, B., 2003. Chemostratigraphic Evidence of Deccan Volcanism from the Marine Osmium Isotope Record. Science 302, 1392-1395.

Rimmer, S.M., Hawkins, S.J., Scott, A.C., Cressler, W.L., 2015. The rise of fire: Fossil charcoal in late Devonian marine shales as an indicator of expanding terrestrial ecosystems, fire, and atmospheric change. American Journal of Science 315, 713-733.

Rooney, A.D., Selby, D., Lloyd, J.M., Roberts, D.H., Lückge, A., Sageman, B.B., Prouty, N.G., 2016. Tracking millennial-scale Holocene glacial advance and retreat using osmium isotopes: Insights from the Greenland ice sheet. Quaternary Science Reviews 138, 49-61.

Saunders, A., Reichow, M., 2009. The Siberian Traps and the End-Permian mass extinction: a critical review. Chinese Science Bulletin 54, 20-37.

Saunders, A.D., 2016. Two LIPs and two Earth-system crises: the impact of the North Atlantic Igneous Province and the Siberian Traps on the Earth-surface carbon cycle. Geological Magazine 153, 201-222.

Schaller, M.F., Fung, M.K., Wright, J.D., Katz, M.E., Kent, D.V., 2016. Impact ejecta at the Paleocene-Eocene boundary. Science 354, 225-229.

Schmitz, B., Peucker-Ehrenbrink, B., Heilmann-Clausen, C., Åberg, G., Asaro, F., Lee, C.-T.A., 2004. Basaltic explosive volcanism, but no comet impact, at the Paleocene–Eocene boundary: high-resolution chemical and isotopic records from Egypt, Spain and Denmark. Earth and Planetary Science Letters 225, 1-17.

Schmitz, B., Pujalte, V., 2003. Sea-level, humidity, and land-erosion records across the initial Eocene thermal maximum from a continental-marine transect in northern Spain. Geology 31, 689-692.

Scott, A.C., Glasspool, I.J., 2006. The diversification of Paleozoic fire systems and fluctuations in atmospheric oxygen concentration. Proceedings of the National Academy of Sciences 103, 10861-10865.

Scott, A.C., Glasspool, I.J., 2007. Observations and experiments on the origin and formation of inertinite group macerals. International Journal of Coal Geology 70, 53-66.

Selby, D., Creaser, R.A., 2003. Re–Os geochronology of organic rich sediments: an evaluation of organic matter analysis methods. Chemical Geology 200, 225-240.

Shao, L., Zhang, P., Dou, J., Shen, S., 2000. Carbon isotope compositions of the Late Permian carbonate rocks in southern China: their variations between the Wujiaping and Changxing formations. Palaeogeography, Palaeoclimatology, Palaeoecology 161, 179-192.

Shen, J., Algeo, T.J., Hu, Q., Xu, G., Zhou, L., Feng, Q., 2013a. Volcanism in South China during the Late Permian and its relationship to marine ecosystem and environmental changes. Global and Planetary Change 105, 121-134.

Shen, S., Zhang, H., Zhang, Y., Yuan, D., Chen, B., He, W., Mu, L., Lin, W., Wang, W., Chen, J., Wu, Q., Cao, C., Wang, Y., Wang, X.J.S.C.E.S., 2019. Permian integrative stratigraphy and timescale of China. Science China-Earth Sciences 62, 154-188.

Shen, S.-z., Cao, C.-q., Zhang, H., Bowring, S.A., Henderson, C.M., Payne, J.L., Davydov, V.I., Chen, B., Yuan, D.-x., Zhang, Y.-c., Wang, W., Zheng, Q.-f., 2013b. High-resolution δ13Ccarb chemostratigraphy from latest Guadalupian through earliest Triassic in South China and Iran. Earth and Planetary Science Letters 375, 156-165.

Shen, S.-z., Crowley, J.L., Wang, Y., Bowring, S.A., Erwin, D.H., Sadler, P.M., Cao, C.-q., Rothman, D.H., Henderson, C.M., Ramezani, J., Zhang, H., Shen, Y., Wang, X.-d., Wang, W., Mu, L., Li, W.-z., Tang, Y.-g., Liu, X.-l., Liu, L.-j., Zeng, Y., Jiang, Y.-f., Jin, Y.-g., 2011. Calibrating the End-Permian Mass Extinction. Science 334, 1367-1372.

Shen, S.-Z., Henderson, C.M., Bowring, S.A., Cao, C.-Q., Wang, Y., Wang, W., Zhang, H., Zhang, Y.-C., Mu, L., 2010. High-resolution Lopingian (Late Permian) timescale of South China. Geological Journal 45, 122-134.

Smoliar, M.I., Walker, R.J., Morgan, J.W., 1996. Re-Os ages of group IIA, IIIA, IVA, and IVB iron meteorites. Science 271, 1099.

Stanley, S. M., 2016. Estimates of the magnitudes of major marine mass extinctions in earth history. Proceedings of the National Academy of Sciences 113, E6325-E6334.

Stein, W.E., Berry, C.M., Hernick, L.V., Mannolini, F., 2012. Surprisingly complex community discovered in the mid-Devonian fossil forest at Gilboa. Nature 483, 78.

Storey, M., Duncan, R.A., Swisher, C.C., 2007. Paleocene-Eocene Thermal Maximum and the Opening of the Northeast Atlantic. Science 316, 587-589.

Svensen, H., Planke, S., Corfu, F., 2010. Zircon dating ties NE Atlantic sill emplacement to initial Eocene global warming. Journal of the Geological Society 167, 433-436.

Svensen, H., Planke, S., Malthe-Sørenssen, A., Jamtveit, B., Myklebust, R., Rasmussen Eidem, T., Rey, S.S., 2004. Release of methane from a volcanic basin as a mechanism for initial Eocene global warming. Nature 429, 542.

Svensen, H., Planke, S., Polozov, A.G., Schmidbauer, N., Corfu, F., Podladchikov, Y.Y., Jamtveit, B., 2009. Siberian gas venting and the end-Permian environmental crisis. Earth and Planetary Science Letters 277, 490-500.

Turgeon, S.C., Creaser, R.A., 2008. Cretaceous oceanic anoxic event 2 triggered by a massive magmatic episode. Nature 454, 323-326.

Wang, W., Cao, C., Wang, Y., 2004. The carbon isotope excursion on GSSP candidate section of Lopingian–Guadalupian boundary. Earth and Planetary Science Letters 220, 57-67.

Wei, H., Yu, H., Wang, J., Qiu, Z., Xiang, L., Shi, G., 2015. Carbon isotopic shift and its cause at the Wuchiapingian–Changhsingian boundary in the Upper Permian at the Zhaojiaba section, South China: Evidences from multiple geochemical proxies. Journal of Asian Earth Sciences 105, 270-285.

Wieczorek, R., Fantle, M.S., Kump, L.R., Ravizza, G., 2013. Geochemical evidence for volcanic activity prior to and enhanced terrestrial weathering during the Paleocene Eocene Thermal Maximum. Geochimica et Cosmochimica Acta 119, 391-410.

Wignall, P.B., 2001. Large igneous provinces and mass extinctions. Earth-Science Reviews 53, 1-33.

Wignall, P.B., Sun, Y., Bond, D.P.G., Izon, G., Newton, R.J., Védrine, S., Widdowson, M., Ali, J.R., Lai, X., Jiang, H., Cope, H., Bottrell, S.H., 2009. Volcanism, Mass Extinction, and Carbon Isotope Fluctuations in the Middle Permian of China. Science 324, 1179-1182.

Wing, S.L., Harrington, G.J., Smith, F.A., Bloch, J.I., Boyer, D.M., Freeman, K.H., 2005. Transient Floral Change and Rapid Global Warming at the Paleocene-Eocene Boundary. Science 310, 993-996.

Wright, J.D., Schaller, M.F., 2013. Evidence for a rapid release of carbon at the Paleocene-Eocene thermal maximum. Proceedings of the National Academy of Sciences 110, 15908-15913.

Yamashita, Y., Takahashi, Y., Haba, H., Enomoto, S., Shimizu, H., 2007. Comparison of reductive accumulation of Re and Os in seawater–sediment systems. Geochimica et Cosmochimica Acta 71, 3458-3475.

Ye, Q., Jiang H., 2016. Conodont Biostratigraphy and a Negative Excursion in Carbonate Carbon Isotopes across the Wuchiapingian–Changhsingian Boundary at the Dawoling Section，Hunan Province. Earth Science 41, 1883-1892. (in Chinese)

Zachos, J., Pagani, M., Sloan, L., Thomas, E., Billups, K., 2001. Trends, Rhythms, and Aberrations in Global Climate 65 Ma to Present. Science 292, 686-693.

Zeebe, R.E., Zachos, J.C., Dickens, G.R., 2009. Carbon dioxide forcing alone insufficient to explain Palaeocene–Eocene Thermal Maximum warming. Nature Geoscience 2, 576.

Chapter 2

Osmium-isotope evidence for volcanism across the Wuchiapingian–Changhsingian boundary interval*

*A version of this chapter has been submitted to Earth and Planetary Science Letters co-authored with David Selby, Hua Zhang, Quanfeng Zheng, Shuzhong Shen, Bradley B. Sageman, Stephen E. Grasby and Benoit Beauchamp.

2.1 Introduction

Carbon isotope excursions (CIEs) temporally coincide with geological and biological crises throughout Earth history, e.g., end-Ordovician, Frasnian–Famennian, end-Permian, end-Triassic and end-Cretaceous mass extinction events (Bond and Grasby, 2017). Although the mechanisms driving CIEs remain debated, some are thought to be caused directly by the release of isotopically light carbon gas arising from the disruption of the global carbon cycle (e.g. reduced organic carbon burial, collapse of the biological pump, increase in organic-carbon weathering, CO_2 released from Large Igneous Provinces (LIPs), etc.: Kump and Arthur, 1999; Payne and Kump, 2007, and references therein). Three CIEs are documented during the Late Permian (Korte and Kozur, 2010) that span the Guadalupian–Lopingian boundary (GLB – ~259 Ma) (Shen et al., 2019b), the Wuchiapingian–Changhsingian boundary (WCB – ~254 Ma) (Shao et al., 2000; Shen et al., 2013), and the Permian–Triassic boundary (PTB – ~252 Ma) (Korte and Kozur, 2010). The latter coincides with the end-Permian mass extinction, which is the largest mass extinction event of the Phanerozoic (Erwin, 2006).

The large negative CIE globally documented by analysis of carbonate ($\delta^{13}C_{carb}$) and organic matter ($\delta^{13}C_{org}$) within the interval immediately below the Permian–Triassic boundary (Korte and Kozur, 2010) is interpreted to be caused by the emission of volcanic CO_2 from

widespread volcanism in Siberia and South China (Payne and Kump, 2007; Shen et al., 2013; Shen et al., 2019a; Svenson et al., 2009) and/or associated carbon release from sedimentary strata (Saunders and Reichow, 2009; Shen et al., 2011). Similarly, the negative CIE (1.7–8‰) of the Guadalupian–Lopingian boundary documented at several sections (e.g., South China, Iran, Spitsbergen) (Bond et al., 2015; Jin et al., 2006a; Shen et al., 2013; Wang et al., 2004; Wignall et al., 2009) coincides with the timing of the Emeishan volcanism in South China, which is ultimately linked with the end-Guadalupian mass extinction (Wignall, 2001; Wignall et al., 2009).

In contrast, distinctive negative CIEs across the WCB are not known in all sections, which has been considered to be a reflection of sampling resolution of previous studies (Shen et al., 2013). However, sections that do exhibit two negative CIEs across the WCB interval, although with different patterns, are observed in several sections in South China (Bagherpour et al., 2018; Bai et al., 2008; Jin et al., 2006b; Shao et al., 2000; Shen et al., 2013, 2010; Wei et al., 2015; Ye and Jiang, 2016), Iran (Liu et al., 2013; Shen et al., 2013) and one section in the Canadian Arctic (Beauchamp et al., 2009) (Fig. 2.1). Unlike the PTB and the GLB, which also have CIEs that are globally recorded, no geological or biological events are linked to the WCB negative CIEs (Shen et al., 2013). Moreover, the driving mechanism of the WCB CIEs have not been linked to volcanism, but in contrast, they have been linked to low primary productivity (Wei et al., 2015) and/or oxidation of exposed organic carbon within peat/coal formations of dry climatic regions (Shao et al., 2000). Other such mechanisms that can cause negative CIEs, for example rapid methane release from the sea floor and / or the heating of organic matter through magma interaction, have been dismissed based on the gradual nature of the negative CIEs across the WCB (Wei et al., 2015).

In this study, we present high-resolution initial osmium isotope ($^{187}Os/^{188}Os$, Os_i) stratigraphy across the correlative WCB sections of Lianyuan, Meishan and Shangsi in South

China and the Buchanan Lake section in the Canadian Arctic to examine the relationship between carbon isotope and osmium isotope records as a means to better elucidate the potential cause and global extent of the CIEs. The Os data exhibit two marked nonradiogenic shifts in Os_i that coincide with the carbon isotope perturbations across the WCB interval, but only the Os_i shift within the earliest Changhsingian is represented globally (Fig. 2). The Os_i shifts are interpreted to be a result of short-lived (700 kyrs) Emeishan volcanism (Shellnutt, 2014), which we argue may explain the lack of any global biological crisis across the WCB interval. We consider this volcanism to have been only regional in extent during the Late Wuchiapingian, but generated enough isotopically light carbon to perturb the global carbon cycle. Volcanism may have been more extensive during the Early Changhsingian, thus affecting both the global seawater $^{187}Os/^{188}Os$ composition and the carbon cycle.

2.2 Geology of the studied interval

South China was situated in the eastern part of the Palaeotethys Ocean during the Late Wuchiapingian to Early Changhsingian (Fig. 2.1). Three sections (Lianyuan, Meishan, Shangsi) spanning the WCB were sampled that record deposition from deltaic and shallow nearshore to progressively more offshore open marine environments, respectively (Li and Shen, 2008; Wang and Jin, 2000). The section from the Canadian Arctic (Buchanan Lake) records deposition on the north-western margin of Pangea during the Late Wuchiapingian to Early Changhsingian (Fig. 2.1). The section represents deep shelf, and slope to basin environments (Beauchamp et al., 2009; Grasby and Beauchamp, 2008). Correlations between the sections are based on high-resolution carbon isotope records, conodont biozones, CA-TIMS U-Pb zircon ages and the Os_i data from this study (Fig. 2.2).

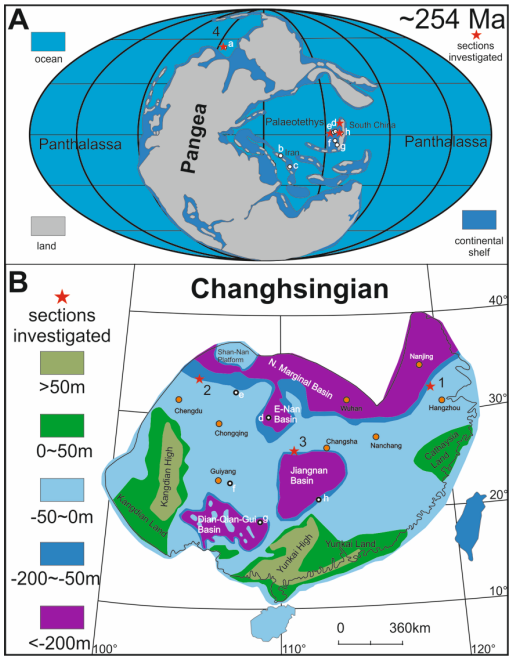

Figure 2.1 Late Permian paleogeographic maps showing the studied areas. (A) Changhsingian global paleogeographic reconstruction map showing the position of the studied sections; base map after Ziegler et al. (1997). (B) South China: 1, Meishan; 2, Shangsi; 3, Lianyuan; base map modified from Wang and Jin (2000). White circles represent other Wuchiapingian–Changhsingian boundary sections where negative carbon isotope excursions are detected: Canada Arctic: (a) Buchanan Lake; Iran: (b) Kuh-e-Ali Bashi, (c) Abadeh; South China: (d) Zhaojiaba, (e) Dukou, (f), Wenjiangsi, (g) Matan, (h) Dawoling.

2.2.1 Lianyuan

The most proximal depositional setting is represented by the Lianyuan locality in the Hunan Province (27.8911°N, 111.8618°E), where both the Upper Lungtan and Lower Talung Formations record the WCB interval in a fresh road-cut. The formations record a transgressive depositional sequence from a deltaic environment to an open marine basin setting across the WCB interval (Li and Shen, 2008; Wang and Jin, 2000). The Lungtan Formation comprises black silty sandstone, which gradually transitions into the Talung Formation, itself characterized by interbedded shale/mudstone with a ~30 cm coal bed. Overlying the coal bed, the Talung Formation is mainly composed of marine facies including black shale/mudstone, siliceous mudstone, calcareous mudstone and chert. The Upper Lungtan Formation contains brachiopods (*Tyloplecta yangtzeensis*, *Permophricodothyris grandis*, *Haydenella kiangsiensis*)

and bivalves (*Schizodus pinguis*, *S. guizhouensis*, *Gujocardita cura*) that only constrain the timing of deposition to Wuchiapingian or Changhsingian. Fossil flora (*Gigantopteris nicotianaefolia-Lobatannularia multifolia* Zone) suggests a similar age range. However, the first occurrence of the conodont *Clarkina wangi* occurs in the lower part of the Talung Formation (Ye and Jiang, 2016). Based on this, the WCB is placed within the Lower Talung Formation, as noted for the Shangsi Section, permitting correlation with the Meishan and Shangsi sections of South China (Fig. 2.2; Jin et al., 2006b; Shen et al., 2013; Yuan et al., 2019).

2.2.2 Meishan

The Meishan section in Changxing County, hosts the Global Stratotype Section and Point (GSSP) for the Wuchiapingian–Changhsingian boundary (Jin et al., 2006b). It represents a transition from a shallow marine, possibly dysoxic (organic-rich) environment in the upper part of the Lungtan Formation to a slope carbonate setting across the WCB. The Lungtan Formation is predominantly characterized by silty sandstone, mudstone, and shale, and contains abundant brachiopods (Li and Shen, 2008). The overlying Changhsing Formation is dominated by limestone with abundant ammonoids and some fusulinids, and is also characterised by multiple ash beds. The basal boundary of the Changhsingian Stage is defined by the first appearance datum (FAD) of *Clarkina wangi* (Jin et al., 2006b). Zircon CA-TIMS U-Pb dating of Beds 6 and 7 (4.9 m and 5.4 m above the FAD of *Clarkina wangi*) yield an age of 253.49 ± 0.07 Ma and 253.45 ± 0.08 Ma, respectively (Shen et al., 2011). The $\delta^{13}C_{carb}$ profile for this interval appears to shift to a more positive baseline in the uppermost part of the Lungtan Formation (Fig. 2.2), but also exhibits two negative shifts of ~2–3 ‰ that bracket the WCB (Fig. 2.2; see Results for detail).

2.2.3 Shangsi

The Shangsi location near Guangyuan, Sichuan Province is an intensively studied Permian section (Riccardi et al., 2007; Shen et al., 2011; Yuan et al., 2019). At Shangsi the

Wuchiaping Formation is composed of organic-rich carbonate, and is overlain by the predominantly siliceous or cherty carbonate of the Talung Formation. The Talung Formation, from the latest Wuchiapingian through the Early Changhsingian, represents the facies with the deepest depositional environment (shelf-slope) of the studied sites. Both formations include beds rich in organic content (total organic carbon, or TOC = 0.87 – 5 wt. %) and contain abundant ammonoids and conodonts (Yuan et al., 2019). Zircon CA-TIMS U-Pb dating from tuff units at 0.9 m below and 3.4 m above the first occurrence of *Clarkina wangi* yield an age of 254.31 ± 0.07 Ma and 253.60 ± 0.08 Ma, respectively (Shen et al., 2011). The $\delta^{13}C_{carb}$ profile differs from Meishan, showing a broad trend toward more negative, and then more positive values (Fig. 2.2), but also includes possible shorter term negative excursions that bracket the WCB (see "Results" below).

2.2.4 Buchanan Lake

The Buchanan Lake section is situated in the Sverdrup Basin of the Canadian Arctic (Grasby and Beauchamp, 2008). This section records a transgressive sequence from a deep shelf-slope environment during the Wuchiapingian Stage to a slope-basin setting during the Changhsingian. The Wuchiapingian–Changhsingian boundary is located within the Black Stripe Formation (Beauchamp et al., 2009). The formation stratigraphically consists of dark grey to black chert and black siliceous shale. Upper Permian conodonts are rare in the Sverdrup Basin and strong provincialism exists because of large latitudinal gradients in water temperature (Mei and Henderson, 2001). Nonetheless, correlation with tropical regions can still be made by the occurrence of *Mesogondolella rosenkrantzi*, possibly associated with *M. sheni,* that suggests a Late Permian age for the Black Stripe Formation (Mei and Henderson, 2001). The $\delta^{13}C_{org}$ profile for this interval also displays two negative shifts of ~2 ‰ that bracket the WCB within the basal part of the Black Stripe Formation (Beauchamp et al., 2009) (Fig. 2.2). Previous work has shown that the $\delta^{13}C_{org}$ record of the Sverdrup Basin closely matches

global organic and inorganic carbon isotope records and can be easily correlated (Grasby et al., 2013).

2.3 Methods

Samples (n = 24) from the Lianyuan section were collected from 0 to 15 m (Fig. 2) for both organic carbon isotope ($\delta^{13}C_{org}$) and rhenium–osmium (Re–Os) analysis. Samples for the Meishan, Shangsi, and Buchanan Lake sections were only collected for Re-Os analysis using archived sample material from previous studies. For the Meishan section, samples (n = 16) from 12 m below to 8 m above the WCB were obtained from archived drill core that had been utilised for $\delta^{13}C_{carb}$ isotope analysis (Cao et al., 2009). For the Shangsi section, the only remaining archived outcrop samples (n = 16; Shen et al., 2013) were obtained from 9 m above to 11 m below the WCB. Lastly, for the Buchanan Lake section, sub-samples (n = 16) from 75 m to 105 m collected during a prior $\delta^{13}C_{org}$ study (Beauchamp et al., 2009) were used.

2.3.1 Re–Os analysis

Before crushing, all samples (20–70 g) were polished to eliminate contamination from cutting and drilling marks. The samples were then air dried at 60 °C for ~12 hours, and broken into chips with no metal contact. Samples were crushed to a fine powder (~30 μm) in a Zirconia ceramic dish using a shatterbox. The sample analytical protocol and Re-Os isotope analysis were carried out at the Durham Geochemistry Centre (Laboratory for Sulfide and Source Rock Geochronology and Geochemistry, and Arthur Holmes Laboratory) at Durham University. For sample digestion, a Cr^{VI}–H_2SO_4 solution was employed to preferentially liberate hydrogenous Re and Os from the organic matter, limiting any contamination from Re and Os in the detritus (Selby and Creaser, 2003). Sample powder weights of ~0.3 to 1 g with a known amount of ^{190}Os and ^{185}Re tracer (spike) solution and 8 mL of 0.25 g/g Cr^{VI}–H_2SO_4 solution were reacted in a sealed carius tube for 48 h at 220 °C (Selby and Creaser, 2003). Osmium was purified using solvent extraction ($CHCl_3$) and micro-distillation methods. From the osmium extracted

solution, rhenium was isolated using solvent extraction ($NaOH$-C_3H_6O) and then purified by anion chromatography. The isolated Re and Os fractions were loaded onto Ni and Pt filaments, respectively. Isotopic measurements were determined using a ThermoElectron TRITON mass spectrometer with static Faraday collection for Re and secondary electron multiplier in peak-hopping mode for Os. Total procedural blanks during this study were 12.5 ± 4.5 pg and 0.12 ± 0.06 pg (1σ S.D., n = 3) for Re and Os, respectively, with an average $^{187}Os/^{188}Os$ value of 0.34 ± 0.20 (n = 3). The initial $^{187}Os/^{188}Os$ values were calculated using the equation:

$$^{187}Os/^{188}Os_{initial} = {}^{187}Os/^{188}Os_{measured} - (^{187}Re/^{188}Os_{measured} * (EXP(\lambda * t)-1))$$

Where λ is ^{187}Re decay constant $1.666e^{-11}a^{-1}$ (Smoliar et al., 1996) and t is the depositional age. The Permian timescale of China constrains the WCB at 254.14 Ma (Shen et al., 2019b). This age is in agreement with that constrained by U-Pb zircon ages from the studied sections and the available biostratigraphy. In this study, Os_i values are calculated using 254.14 Ma.

2.3.2 Organic carbon isotope analysis

Organic carbon isotopic data were established for the Lianyuan section at the Stable Isotope Laboratory at Northwestern University. Prior to analysis, samples were acidified: ~1 g of powder was mixed with 15 mL 2 N HCl and left for 24 hours. Acid was decanted and then the samples were repeatedly rinsed with Milli-Q water until acid was neutralised. Samples were then dried down in an oven at 50 ˚C for 2–3 days until samples are completely dry. The samples were ground to fine powder and loaded into tin capsules. Carbon isotope values ($\delta^{13}C_{org}$) were analysed using a Costech ECS4010 Elemental Analyser coupled to a Thermo Delta V Plus isotope ratio mass spectrometer. To correct for instrument mass fractionation and adjust to the VPBD per mil scale, raw results were calibrated using acetanilide and urea (Indiana University - IU) standards (Schimmelmann et al., 2009). The average precision (1s) on IU-acetanilide standards throughout the analytical run was ±0.09 ‰ (n = 10), and the range of precision on sample duplicates (n = 3) is (±0.14 to ±0.26 ‰, mean ±0.21 ‰).

2.4 Results

2.4.1 Carbon isotope profile

The $\delta^{13}C_{org}$ data established for the Lianyuan section from this study yield values ranging from -22 to -26 ‰ (Fig. 2.2). The $\delta^{13}C_{org}$ values show a steady decline from -22 to -24 ‰ in the Upper Lungtan to Lower Talung Formations, with a one-point excursion to -25 ‰ at 4.5 m below the WCB. From here the $\delta^{13}C_{org}$ values return to ~-23 ‰ and remain relatively stable until the WCB. At 2 m above the WCB the $\delta^{13}C_{org}$ values exhibit a sharp negative excursion to -26 ‰, and then return to less negative values (~24 ‰).

The $\delta^{13}C_{org}$ profile of the Lianyuan section is similar to carbon isotope profiles for the Meishan, Shangsi, and Buchanan Lake sections (Fig. 2.2; Beauchamp et al., 2009; Shen et al., 2013), which we also briefly describe below. At the Meishan section, the $\delta^{13}C_{carb}$ profile for this interval exhibits two negative shifts (2 – 3 ‰). Within the Upper Wuchiapingian Lungtan Formation $\delta^{13}C_{carb}$ shifts from ~0 to -2 ‰, and then to ~4 ‰. Remaining at ~4 ‰, $\delta^{13}C_{carb}$ shows a 3 ‰ negative excursion within the basal part of the Changhsingian Stage in the Changhsing Formation, and then returns to values of ~3 ‰. At Shangsi, the $\delta^{13}C_{carb}$ profile shows a steady trend to more negative values through the Talung Formation, to a nadir of -3 ‰ just below the WCB, which is followed by a trend to 1.5 ‰ at the WCB. The $\delta^{13}C_{carb}$ values then remain similar until a ~3 ‰ negative excursion within the basal part of Changhsingian Stage. At Buchanan Lake, the $\delta^{13}C_{org}$ profile for this interval exhibits two negative shifts. The $\delta^{13}C_{org}$ values decrease from ~ -26 ‰ to -27 ‰ at the basal part of the Black Stripe Formation, which then return to the pre-excursion values around the WCB. Above the WCB, $\delta^{13}C_{org}$ values decline to ~ -27 ‰ and then increase to ~ -26 ‰.

2.4.2 Rhenium and osmium abundance and $^{187}Os/^{188}Os$ isotope stratigraphy

At the Lianyuan section, Re and Os abundances range from 0.15 to 30.63 ppb and 18.4 to 296.1 ppt (^{192}Os = ~10 – 95 ppt). The Os_i in the Lungtan Formation is radiogenic (1.2) and

becomes gradually unradiogenic to a nadir of 0.20 (coinciding with the lower $\delta^{13}C_{org}$ negative excursion) within the coal interval of the Talung Formation. The Os_i values then increase steadily to ~0.5 at ~2 m below the WCB, then decline steadily to ~0.16 within the basal Changhsingian (overlapping with the upper $\delta^{13}C_{org}$ negative excursion), and finally return to more radiogenic Os_i values of ~0.5 coincident with $\delta^{13}C_{org}$ returning to more stable values. Changes in the common Os budget, represented by ^{192}Os, broadly follow that shown by Os_i (Fig. 2.2). For example, in the basal part of the Lungtan Formation ^{192}Os increases dramatically to ~95 ppt (coeval with the decline in Os_i) and then declines gradually to ~40 ppt (where Os_i increases to ~0.5), and again increases to the base of the WCB (where Os_i trends to more non-radiogenic). Within the basal Changhsingian ^{192}Os remains at ~10 ppt.

At the Meishan section, Re and Os values range from 1.35 to 131.02 ppb and 22.2 to 887.5 ppt, respectively (^{192}Os = ~11 to 200 ppt). In contrast to Lianyuan, there is no apparent relationship between ^{192}Os and Os_i (Fig. 2.2). The ^{192}Os abundance is predominantly ~11 ppt, with higher abundances within the Lungtan Formation at ~50 m (up to 186 ppt), and then within the basal Changhsingian within the lower Changhsing Formation (up to 207 ppt). The Os_i in the basal part of the Lungtan Formation is ~0.6 and then abruptly drops to an unradiogenic value of ~0.2 close to the top of the Lungtan Formation, coincident with the lower $\delta^{13}C_{carb}$ excursion (Fig. 2.2). The Os_i values then gradually shift to more radiogenic (~0.8) at ~0.5 m below the WCB, and then decline to ~0.4 at the base of the Changhsing Formation, coincident with the upper $\delta^{13}C_{carb}$ excursion. The Os_i then returns to more radiogenic values of ~0.5.

At the Shangsi section, Re and Os range from 0.78 to 1017.76 ppb and 10.9 to 3932.2 ppt, respectively (^{192}Os = ~3.5 – 483.6 ppt). Like the Meishan section, no apparent relationship between ^{192}Os and Os_i is observed (Fig. 2.2). The Os_i values (~0.5) through the Late Wuchiapingian, prior to the lower $\delta^{13}C_{carb}$ excursion, are similar within uncertainty. In contrast to the other sections coincident with the lower $\delta^{13}C_{carb}$ excursion, Os_i becomes slightly more

radiogenic (~0.70), and then exhibits a single-point shift to less radiogenic values (~0.35) within the basal Changhsingian, which then abruptly returns to more radiogenic values of ~0.5. In this case, however, the Os_i change to less radiogenic values occurs prior to the upper $\delta^{13}C_{carb}$ excursion (Fig. 2.2).

At the Buchanan Lake section, Re and Os abundances range from 0.11 to 25.91 ppb and 72.9 to 240.9 ppt, respectively (^{192}Os = ~38 to 73 ppt). The Os_i values in the basal part of the Black Stripe Formation (Upper Wuchiapingian) are relatively invariant (~0.55), and specifically show no change in composition within the lower $\delta^{13}C_{org}$ negative excursion, as was observed for the Shangsi section. In contrast, and coincident with the upper $\delta^{13}C_{org}$ negative excursion, Os_i values decrease sharply to ~0.33 during the earliest Changhsingian and then increase to pre-excursion values of up to ~0.80.

Figure 2.2 (next page) Carbon isotope (black), Os_i (red) and ^{192}Os (blue) stratigraphy. Initial $^{187}Os/^{188}Os$ data are calculated at 254.14 Ma (Shen et al., 2019b). The $\delta^{13}C_{carb}$ data of Meishan and Shangsi are from Shen et al. (2013). Conodont zones for South China sections are from Shen et al. (2013b). The U-Pb zircon ages are from Shen et al. (2011). The $\delta^{13}C_{org}$ data of Lianyuan are from this study. The $\delta^{13}C_{org}$ and conodont data of the Buchanan Lake section are from Beauchamp et al. (2009) and Mei and Henderson (2001). Grey zones represent the correlation between sections based on the carbon isotope stratigraphy (Beauchamp et al., 2009; Shen et al., 2013).

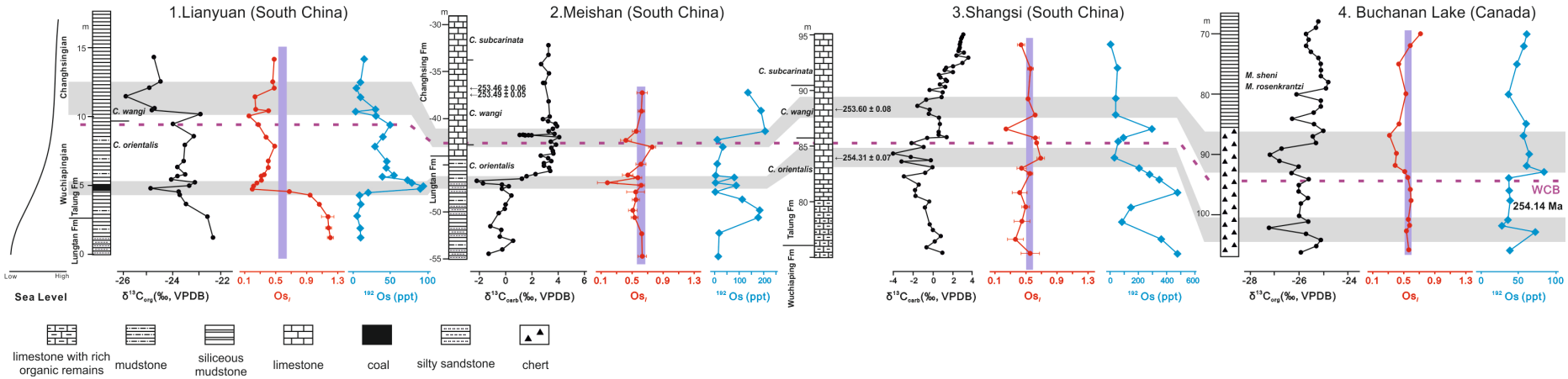
1.Lianyuan (South China)
2.Meishan (South China)
3.Shangsi (South China)
4. Buchanan Lake (Canada)
Changhsingian
Wuchiapingian
Talung Fm
Lungtan Fm
Changhsing Fm
C. wangi
C. orientalis
C. subcarinata
253.46 ± 0.06
253.49 ± 0.05
253.60 ± 0.08
254.31 ± 0.07
M. sheni
M. rosenkrantzi
WCB
254.14 Ma
Sea Level
Low
High
δ13Corg(‰, VPDB)
δ13Ccarb(‰, VPDB)
Osi
192Os (ppt)
limestone with rich organic remains
mudstone
siliceous mudstone
limestone
coal
silty sandstone
chert

2.5 Discussion

2.5.1 Seawater Os_i during Late Wuchiapingian

Trends in Os_i toward less radiogenic values in the Lianyuan and Meishan sections, although of different magnitude, are coincident with the carbon isotope profiles, and thus considered time-correlative (Fig. 2.2). For the Shangsi and Buchanan Lake sections, however, trends to less radiogenic Os_i that coincide with the temporal period of the carbon isotope excursion are only observed within the Early Changhsingian (Fig. 2.2).

The Os_i values in the Late Wuchiapingian part of the Lianyuan section are much more radiogenic (~1.20) than those from the same time interval in the Meishan (~0.60), Shangsi (~0.55) and Buchanan Lake (~0.55) sites. The highly radiogenic Os_i values of Lianyuan are attributed to the dominant delivery of weathered crustal materials in response to the more proximal depositional setting (e.g., deltaic plain; Wang and Jin, 2000) that the Lianyuan strata record. In contrast, the moderately radiogenic Os_i values (~0.5–0.6) from the Meishan, Shangsi, and Buchanan Lake sections likely represent a more distal marine depositional setting (e.g., shallow marine, slope-shelf, and open marine; Jin et al., 2006b; Shen et al., 2013; Beauchamp et al., 2009) and given the similarity of the Os_i values, potentially a more global representation of the ocean $^{187}Os/^{188}Os$ composition.

2.5.2 Unradiogenic Os_i excursions and the link with volcanism

The first unradiogenic Os_i shift, which is only observed in the Lianyuan and Meishan sections, occurred concurrently with a sea-level rise event (Li and Shen, 2008; Wang and Jin, 2000). If this unradiogenic shift were caused simply by a shift in the local water column to more fully marine conditions, an Os_i value intermediate between contemporaneous seawater Os_i and local radiogenic Os_i values would be expected. However, the Os_i at Lianyuan (~0.2) and Meishan (~0.17) is more non-radiogenic than that of open marine seawater (~0.55), as inferred from the open marine sections of Shangsi and Buchanan Lake. We conclude that the

shift to non-radiogenic Os_i reveals an actual perturbation in the seawater Os reservoir within the Paleo-Tethys Ocean, but not the entire Paleo-Tethys and the global Panthalassa Ocean. The absence of any change to more non-radiogenic Os_i for the more open marine setting represented by the Shangsi section, where Os_i becomes slightly more radiogenic (Fig. 2), suggests that the $^{187}Os/^{188}Os$ of the Paleo-Tethys Ocean is controlled by the site's palaeoceanographic setting. As such, the mechanism driving the change in the seawater $^{187}Os/^{188}Os$ composition observed at Lianyuan and Meishan was only capable of affecting the more proximal depositional settings.

The observed non-radiogenic Os_i shifts may be caused by (1) reduced radiogenic Os input from weathered continental material, (2) increased non-radiogenic Os flux from enhanced hydrothermal activity and/or meteorite impact events, or (3) the Os isotope composition of weathered material being less radiogenic due to erosion of different hinterland strata (Peucker-Ehrenbrink and Ravizza, 2000). Climatic cooling is capable of diminishing the weathering rate of ancient crust. Given the extent of the non-radiogenic Os_i shifts (~0.16 and 0.20 at Lianyuan), a nearly complete shutdown of the weathering process (e.g., due to glaciation) would be required to cause the magnitude of the observed non-radiogenic Os_i shift (Finlay et al., 2010). It has been argued that the Permian climate experienced a cooling during the earliest Wuchiapingian in response to weathering of the Emeishan continental flood basalts (Yang et al., 2018). Cooling based on oxygen isotope proxies has also been invoked for the Changhsingian, however it is unclear whether this cooling was due to glaciation (Chen et al., 2013). The termination age of the youngest known Permian glaciation (P4) is 254.5 Ma (Metcalfe et al., 2015). Given the timing of the known P4 glaciation and uncertainty in the extent of climate cooling, a cooling event is unlikely to be the mechanism causing the non-radiogenic Os_i shifts observed across the WCB.

No extraterrestrial impact event is known to be associated with the WCB, therefore we attribute the source of non-radiogenic Os to magmatic activity and the associated weathering

of newly erupted/fresh basaltic units. Two large igneous provinces (LIPs) are known in the Middle and Late Permian: the Emeishan and the Siberian Traps LIPs. Even though dating results have linked the Emeishan LIP with the end-Guadalupian mass extinction (Zhong et al., 2014; Bond et al., 2015; Wignall et al., 2009; Grasby et al., 2015), and the Siberian Traps LIP with the end-Permian mass extinction (Burgess et al., 2014, 2017; Saunders and Reichow, 2009), the age of the Emeishan LIP does overlap, in part, with the Wuchiapingian–Changhsingian boundary age (254.14 Ma; Shen et al., 2019b). However, it is not certain if the magmatism at the WCB, as suggested here, is associated with the Emeishan LIP (based on available data). Although the first non-radiogenic pulse is only recorded in the Lianyuan and Meishan sections, the second is detected in all four sections. The difference in magnitude of the two negative Os_i excursions may suggest that the second pulse of volcanism was more intense and had a more significant global impact on the $^{187}Os/^{188}Os$ composition of the ocean.

The Os_i values in the Lianyuan section recover to more radiogenic levels following the excursions to non-radiogenic Os_i values. Yet, background Os_i values at Lianyuan are significantly more non-radiogenic than the Os_i values recorded for the more open marine sites observed at Meishan, Shangsi, and Buchanan Lake. The long-lasting non-radiogenic Os_i signature in the Lianyuan section likely suggests that the Lianyuan section remained relatively restricted, or in a proximal depositional setting, following the marine transgression. It is probable that Os in the local water mass at Lianyuan was dominated by a non-radiogenic Os input from the weathering of fresh mafic igneous rocks or continued mafic volcanism.

2.5.3 LIP events and mass extinction

Magmatism associated with LIPs is often implicated in rapid environmental destabilization and severe biological crises, such as the Siberian Traps LIP and end-Permian mass extinction, Emeishan volcanism and the end-Guadalupian mass extinction, Deccan Traps and the end-Cretaceous mass extinction, North Atlantic Igneous Province and the Palaeocene

–Eocene Thermal Maximum, Karoo-Ferrar Traps and the Early Jurassic ocean anoxic event, etc. (Bond and Grasby, 2017; Courtillot and Renne, 2003; Wignall, 2001). Nonetheless, not all LIP events have driven environmental change and mass extinction (Wignall, 2001). Several factors may affect the impact of LIP magmatism. The emplacement style of the LIP (i.e., vertical or lateral; intrusive or extrusive) appears to play a critical role in determining the magnitude of environmental impact (Burgess et al., 2017; Renne et al., 2015). A recent study of the end-Permian mass extinction and Siberian LIP suggests that catastrophic global environmental change is more likely caused by sill complexes rather than flood basalts and/or dike components (Burgess et al., 2017). The composition of the strata into which sills are intruded also plays an important role on volatile generation (Burgess et al., 2017). Further, a small volume volcanic eruption may not have a notable effect on global Earth systems. Moreover, a large volume eruption over a long period may also have less effect than a small but rapid eruption (Renne et al., 2015). As there was no discernible mass extinction event associated with WCB volcanism, it was likely associated with a small-volume eruption. Even if it was a LIP, it might have erupted through volatile-poor substrates. Thus, generation of only a limited amount of climate-altering volatiles may have permitted the biosphere to overcome the effects of volcanic gas emission. As such, WCB volcanism may have only had a regional impact, with any climate perturbation rapidly overturned back to pre-eruption-like conditions.

2.5.4 WCB carbon isotope excursions

The cause(s) of the WCB carbon isotope excursions remain unclear. Previous research has suggested a reduction of primary production, based on the correlation between total organic carbon (TOC) and $\delta^{13}C_{org}$ (Wei et al., 2015). However, sea level fall is also considered to have exposed coal/peat formations that released ^{12}C enriched CO_2 through the weathering of organic matter (Shao et al., 2010). Enhanced continental weathering should increase radiogenic Os input to the ocean and thus lead to a radiogenic shift in Os_i, which is apparent in the data.

Further, there is no sea-level regression documented around the WCB. In contrast, a regional transgression is documented in South China (Li and Shen, 2008; Wang and Jin, 2000). Previously, the role of volcanic outgassing was ruled out as no such event was known for this time interval (Wei et al., 2015). But our new Os_i data, which is consistent with increased volcanism, suggests that input to the atmosphere of isotopically light carbon may have contributed to the negative CIEs spanning the WCB. This would be similar to the even larger CIEs associated with the Siberian Trap Eruptions of the Late Permian and Early Triassic (Payne and Kump, 2007). Such volcanism may also have disturbed the environment sufficiently to cause decreases in primary production (Wei et al., 2015). The first pulse of volcanism during the Late Wuchiapingian was probably regional in scale, and only perturbed local $^{187}Os/^{188}Os$ in South China, but was capable of affecting the global carbon cycle. In contrast, the second pulse of volcanism during the Late Changhsingian may have been more intense and affected both the global carbon and seawater $^{187}Os/^{188}Os$ record.

2.6 Conclusion

The first shift to non-radiogenic Os_i during the latest Wuchiapingian is only detected at two sections in South China (Lianyuan and Meishan), whereas the second excursion to non-radiogenic Os_i values during the earliest Changhsingian is observed in all four studied sections. The two excursions to unradiogenic Os_i correlate with two negative carbon isotope excursions across the WCB interval. The Os_i shifts are interpreted to reflect volcanic events, with only the Early Changhsingian event able to perturb the global ocean $^{187}Os/^{188}Os$. Volcanism has long been proposed as a killing mechanism associated with mass extinctions. The volcanism associated with the WCB, however, appears to have been insufficient to drive massive environmental change to disrupt the biosphere. The injection of isotopically light carbon from volcanic outgassing may have been an additional mechanism that caused the CIEs across the WCB. This study demonstrates how Os geochemistry may be used to assess the relative

magnitude of ancient volcanic events, which are proving to be one of the most common drivers of major biogeochemical perturbations in Earth history.

2.7 References

Bagherpour, B., Bucher, H., Schneebeli-Hermann, E., Vennemann, T., Chiaradia, M., Shen, S.-z., 2018. Early Late Permian coupled carbon and strontium isotope chemostratigraphy from South China: Extended Emeishan volcanism? Gondwana Research 58, 58-70.

Bai, X., Luo, G., Wu, X., Wang, Y., Huang, J., Wang, X., 2008. Carbon Isotope Records Indicative of Paleoceanographical Events at the Latest Permian Dalong Formation at Shangsi, Northeast Sichuan, China. Journal of China University of Geosciences 19, 481-487.

Beauchamp, B., Henderson, C.M., Grasby, S.E., Gates, L.T., Beatty, T.W., Utting, J., James, N.P., 2009. Late Permian Sedimentation in the Sverdrup Basin, Canadian Arctic: The Lindstrom and Black Stripe Formations. Bulletin of Canadian Petroleum Geology 57, 167-191.

Bond, D.P.G., Grasby, S.E., 2017. On the causes of mass extinctions. Palaeogeography, Palaeoclimatology, Palaeoecology 478, 3-29.

Bond, D. P. G., Savov, I., Wignall, P. B., Joachimski, M. M., Sun, Y., Grasby, S. E., Beauchamp, B., Blomeier, D. P. G., 2015. An abrupt extinction in the Middle Permian (Capitanian) of the Boreal Realm (Spitsbergen) and its link to anoxia and acidification. GSA Bulletin 127, 1411-1421.

Burgess, S.D., Bowring, S., Shen, S.-z., 2014. High-precision timeline for Earth's most severe extinction. Proceedings of the National Academy of Sciences 111, 3316-3321.

Burgess, S.D., Muirhead, J.D., Bowring, S.A., 2017. Initial pulse of Siberian Traps sills as the trigger of the end-Permian mass extinction. Nature Communications 8, 164.

Cao, C., Love, G.D., Hays, L.E., Wang, W., Shen, S., Summons, R.E., 2009. Biogeochemical evidence for euxinic oceans and ecological disturbance presaging the end-Permian mass extinction event. Earth and Planetary Science Letters 281, 188-201.

Chen, B., Joachimski, M.M., Shen, S.-z., Lambert, L.L., Lai, X.-l., Wang, X.-d., Chen, J., Yuan, D.-x., 2013. Permian ice volume and palaeoclimate history: Oxygen isotope proxies revisited. Gondwana Research 24, 77-89.

Courtillot, V.E., Renne, P.R., 2003. On the ages of flood basalt events. Comptes Rendus Geoscience 335, 113-140.

Erwin, D.H., 2006. Extinction: How Life on Earth Nearly Ended 250 Million Years Ago. Princeton University Press, Princeton.

Finlay, A.J., Selby, D., Gröcke, D.R., 2010. Tracking the Hirnantian glaciation using Os isotopes. Earth and Planetary Science Letters 293, 339-348.

Grasby, S. E., Beauchamp, B., Bond, D. P. G., Wignall, P. B., Sanei, H., 2015, Mercury anomalies associated with three extinction events (Capitanian Crisis, Latest Permian Extinction and the Smithian/Spathian Extinction) in NW Pangea. Geological Magazine 153, 285-297.

Grasby, S. E., Beauchamp, B., Embry, A. F., Sanei, H., 2013. Recurrent Early Triassic ocean anoxia. Geology41,175-178.

Grasby, S. E., Beauchamp, B., 2008. Intrabasin variability of the carbon-isotope record across the Permian-Triassic transition, Sverdrup Basin, Arctic Canada. Chemical Geology 253, 141-150.

Jin, Y., Shen, S., Henderson, C.M., Wang, X., Wang, W., Wang, Y., Cao, C., Shang, Q., 2006a. The Global Stratotype Section and Point (GSSP) for the boundary between the Capitanian and Wuchiapingian Stage (Permian). Episodes 29, 253-262.

Jin, Y., Wang, Y., Henderson, C., Wardlaw, B.R., Shen, S., Cao, C., 2006b. The Global Boundary Stratotype Section and Point (GSSP) for the base of Changhsingian Stage (Upper Permian). Episodes 29, 175-182.

Korte, C., Kozur, H.W., 2010. Carbon-isotope stratigraphy across the Permian–Triassic boundary: A review. Journal of Asian Earth Sciences 39, 215-235.

Kump, L.R., Arthur, M.A., 1999. Interpreting carbon-isotope excursions: carbonates and organic matter. Chemical Geology 161, 181-198.

Li, W.-Z., Shen, S.-Z., 2008. Lopingian (Late Permian) brachiopods around the Wuchiapingian-Changhsingian boundary at the Meishan Sections C and D, Changxing, South China. Geobios 41, 307-320.

Liu, X.-c., Wang, W., Shen, S.-z., Gorgij, M.N., Ye, F.-c., Zhang, Y.-c., Furuyama, S., Kano, A., Chen, X.-z., 2013. Late Guadalupian to Lopingian (Permian) carbon and strontium isotopic chemostratigraphy in the Abadeh section, central Iran. Gondwana Research 24, 222-232.

Mei, S., Henderson, C.M., 2001. Evolution of Permian conodont provincialism and its significance in global correlation and paleoclimate implication. Palaeogeography, Palaeoclimatology, Palaeoecology 170, 237-260.

Metcalfe, I., Crowley, J.L., Nicoll, R.S., Schmitz, M., 2015. High-precision U-Pb CA-TIMS calibration of Middle Permian to Lower Triassic sequences, mass extinction and extreme climate-change in eastern Australian Gondwana. Gondwana Research 28, 61-81.

Payne, J.L., Kump, L.R., 2007. Evidence for recurrent Early Triassic massive volcanism from quantitative interpretation of carbon isotope fluctuations. Earth and Planetary Science Letters 256, 264-277.

Peucker-Ehrenbrink, B., Ravizza, G., 2000. The marine osmium isotope record. Terra Nova 12, 205-219.

Renne, P.R., Sprain, C.J., Richards, M.A., Self, S., Vanderkluysen, L., Pande, K., 2015. State shift in Deccan volcanism at the Cretaceous-Paleogene boundary, possibly induced by impact. Science 350, 76-78.

Riccardi, A., Kump, L.R., Arthur, M.A., D'Hondt, S., 2007. Carbon isotopic evidence for chemocline upward excursions during the end-Permian event. Palaeogeography, Palaeoclimatology, Palaeoecology 248, 73-81.

Saunders, A., Reichow, M., 2009. The Siberian Traps and the End-Permian mass extinction: a critical review. Chinese Science Bulletin 54, 20-37.

Schimmelmann, A., Albertino, A., Sauer, P.E., Qi, H., Molinie, R., Mesnard, F., 2009. Nicotine, acetanilide and urea multi-level ^{2}H-, ^{13}C- and ^{15}N-abundance reference materials for continuous-flow isotope ratio mass spectrometry. Rapid Communications in Mass Spectrometry 23, 3513-3521.

Selby, D., Creaser, R.A., 2003. Re–Os geochronology of organic rich sediments: an evaluation of organic matter analysis methods. Chemical Geology 200, 225-240.

Shao, L., Zhang, P., Dou, J., Shen, S., 2000. Carbon isotope compositions of the Late Permian carbonate rocks in southern China: their variations between the Wujiaping and Changxing formations. Palaeogeography, Palaeoclimatology, Palaeoecology 161, 179-192.

Shellnutt, J.G., 2014. The Emeishan large igneous province: A synthesis. Geoscience Frontiers 5, 369-394.

Shen, S.-z., Cao, C.-q., Zhang, H., Bowring, S.A., Henderson, C.M., Payne, J.L., Davydov, V.I., Chen, B., Yuan, D.-x., Zhang, Y.-c., Wang, W., Zheng, Q.-f., 2013. High-

resolution δ13Ccarb chemostratigraphy from latest Guadalupian through earliest Triassic in South China and Iran. Earth and Planetary Science Letters 375, 156-165.

Shen, S.-z., Crowley, J.L., Wang, Y., Bowring, S.A., Erwin, D.H., Sadler, P.M., Cao, C.-q., Rothman, D.H., Henderson, C.M., Ramezani, J., Zhang, H., Shen, Y., Wang, X.-d., Wang, W., Mu, L., Li, W.-z., Tang, Y.-g., Liu, X.-l., Liu, L.-j., Zeng, Y., Jiang, Y.-f., Jin, Y.-g., 2011. Calibrating the End-Permian Mass Extinction. Science 334, 1367-1372.

Shen, S.-Z., Henderson, C.M., Bowring, S.A., Cao, C.-Q., Wang, Y., Wang, W., Zhang, H., Zhang, Y.-C., Mu, L., 2010. High-resolution Lopingian (Late Permian) timescale of South China. Geological Journal 45, 122-134.

Shen, S., Ramezani, J., Chen, J., Cao, C., Erwin, D., Zhang, H., Xiang, L., Schoepfer, S., Henderson, C., Zheng, Q., A. Bowring, S., Wang, Y., Li, X.-H., Wang, X.-D., Yuan, D., Zhang, Y., Lin, M., Wang, J., Wu, Y.S., 2019a. A sudden end-Permian mass extinction in South China. Geological Society of America Bulletin 131, 205-223.

Shen, S., Zhang, H., Zhang, Y., Yuan, D., Chen, B., He, W., Mu, L., Lin, W., Wang, W., Chen, J., Wu, Q., Cao, C., Wang, Y., Wang, X., 2019b. Permian integrative stratigraphy and timescale of China. Science China: Earth Sciences 62, 154-188.

Smoliar, M.I., Walker, R.J., Morgan, J.W., 1996. Re-Os ages of group IIA, IIIA, IVA, and IVB iron meteorites. Science 271, 1099.

Svensen, H., Planke, S., Polozov, A.G., Schmidbauer, N., Corfu, F., Podladchikov, Y.Y., Jamtveit, B., 2009. Siberian gas venting and the end-Permian environmental crisis. Earth and Planetary Science Letters 277, 490-500.

Wang, W., Cao, C., Wang, Y., 2004. The carbon isotope excursion on GSSP candidate section of Lopingian–Guadalupian boundary. Earth and Planetary Science Letters 220, 57-67.

Wang, Y., Jin, Y., 2000. Permian palaeogeographic evolution of the Jiangnan Basin, South China. Palaeogeography, Palaeoclimatology, Palaeoecology 160, 35-44.

Wei, H., Yu, H., Wang, J., Qiu, Z., Xiang, L., Shi, G., 2015. Carbon isotopic shift and its cause at the Wuchiapingian–Changhsingian boundary in the Upper Permian at the Zhaojiaba section, South China: Evidences from multiple geochemical proxies. Journal of Asian Earth Sciences 105, 270-285.

Wignall, P.B., 2001. Large igneous provinces and mass extinctions. Earth-Science Reviews 53, 1-33.

Wignall, P.B., Sun, Y., Bond, D.P.G., Izon, G., Newton, R.J., Védrine, S., Widdowson, M., Ali, J.R., Lai, X., Jiang, H., Cope, H., Bottrell, S.H., 2009. Volcanism, Mass Extinction, and Carbon Isotope Fluctuations in the Middle Permian of China. Science 324, 1179-1182.

Yang, J., Cawood, P.A., Du, Y., Condon, D.J., Yan, J., Liu, J., Huang, Y., Yuan, D., 2018. Early Wuchiapingian cooling linked to Emeishan basaltic weathering? Earth and Planetary Science Letters 492, 102-111.

Ye, Q., Jiang H., 2016. Conodont Biostratigraphy and a Negative Excursion in Carbonate Carbon Isotopes across the Wuchiapingian–Changhsingian Boundary at the Dawoling Section，Hunan Province. Earth Science 41, 1883-1892. (in Chinese)

Yuan, D.-X., Shen, S.-z., Henderson, C.M., Chen, J., Zhang, H., Zheng, Q.-f., Wu, H., 2019. Integrative timescale for the Lopingian (Late Permian): A review and update from Shangsi, South China. Earth-Science Reviews 188, 190-209.

Zhong, Y.-T., He, B., Mundil, R., Xu, Y.-G., 2014. CA-TIMS zircon U–Pb dating of felsic ignimbrite from the Binchuan section: Implications for the termination age of Emeishan large igneous province. Lithos 204, 14-19.

Ziegler, A.M., Hulver, M.L., Rowley, D.B., 1997. Permian world topography and climate. In: Martini, I.P. (Ed.), Late Glacial and Postglacial Environmental Changes–Quaternary,

Carboniferous–Permian and Proterozoic. Oxford University Press, New York, pp. 111–146.

Chapter 3

Evidence of Wildfires and Elevated Atmospheric Oxygen at the Frasnian–Famennian Boundary in New York (USA): Implications for the Late Devonian Mass Extinction*

*A version of this chapter has been submitted to Earth and Planetary Science Letters co-authored with David Selby, Paul C. Hackley, and D. Jeffrey Over.

3.1 Introduction

During the Devonian Period the level of atmospheric O_2 is considered to have significantly fluctuated in response to the diversification and radiation of terrestrial plant life, and to have caused an increase in size of fauna (Dahl et al., 2010). Currently debated is the timing and amount of O_2 change throughout the Devonian into the Carboniferous. For example, O_2 levels are estimated to have dropped from ~25 % to ~13 % during the Devonian, with the O_2 levels then steadily rising to present atmospheric levels (21 %) by the mid-Mississippian Epoch (Berner, 2006; Rimmer et al., 2015; Scott and Glasspool, 2006). In contrast, O_2 levels are also suggested to have dropped from ~25 % during the Early Devonian to ~17% in the early Late Devonian, and then increased to ~22 % during Late Devonian (Berner et al., 2003; Berner, 2009). In addition to the atmospheric O_2 response related to the evolution of flora and fauna, a positive feedback between atmospheric O_2 and episodes of fire has been proposed whereby higher O_2 concentrations are related to higher frequencies of fire events that result in charcoal production and burial (Berner et al., 2003). This burial of black carbon creates a further increase in atmospheric O_2 by drawing down the pCO_2 (Berner et al., 2003). Inertinite macerals, the preserved charred remains of woody material, provides a record of wildfire events and its

presence in the sedimentary record has been used to infer ancient atmospheric O_2 levels (Scott and Glasspool, 2007; Glasspool and Scott, 2010).

In addition to fluctuations in atmospheric O_2, the Devonian Period also witnessed the Frasnian–Famennian (F–F) mass extinction, which is one of the Phanerozoic 'big five' mass extinction events (Stanley, 2016). Proposed extinction mechanisms for this Devonian extinction include ocean anoxic or euxinic conditions (Bond et al., 2004), climate cooling (Joachimski and Buggisch, 2002; Joachimski et al., 2009), sea-level change (Johnson et al., 1985; Bond and Wignall, 2008), bolide impact (Claeys et al., 1992), and volcanism (Racki et al., 2018).

This paper presents new organic petrology and initial osmium isotope ($^{187}Os/^{188}Os_i$, Os_i) stratigraphy, major and trace element analyses, and programmed pyrolysis analysis of samples from five Upper Devonian (F–F interval) sections from western New York, USA and discusses the evidence for wildfire events at the F–F boundary and, by inference, the level of atmospheric O_2 (and inference for pCO_2 levels) and the possible mechanisms that led to the F–F mass extinction.

3.2. Geological background

In western New York State (USA), the sedimentary record of the F–F interval consists of siliciclastic mudstones and sandstones that are interpreted as slope to basin deposits in the northern Appalachian foreland basin (Fig. 3.1; Sageman et al., 2003; Over, 1997). This study focuses on five measured sections (Fig. 3.1), four of which are from outcrops (Irish Gulf, IG; Beaver Meadow Creek, BMC; Walnut Creek Bank, WCB; and Joint Creek, JC) and one is from a drill core (West Valley, WV). These sections are interpreted as proximal to distal deposits (JC, BMC, WV, IG and WCB, respectively; Fig. 3.1).

In all sections, the Frasnian–Famennian (F–F) interval is mapped as Late Frasnian and earliest Famennian Hanover Formation and the Early Famennian Dunkirk Formation. The

Hanover Formation comprises light gray, silty shale and interbedded black silty shale that is rich in organic matter (~0.5–5 wt. % TOC), which is of low thermal maturity (%BR_o ~ 0.6, solid bitumen reflectance). The gray shale is intensively bioturbated and contains poorly preserved brachiopods and bivalves. The black shale is pyrite-rich, finely laminated (except the base parts where bioturbation is observed), and is interpreted as having accumulated in anoxic/dysoxic conditions. The Hanover Formation is overlain by the Dunkirk Formation, which contains distinctive beds of black shale. In all sections the F–F boundary is defined by the first occurrence of the conodont *Palmatolepsis triangularis* (Fig. 3.2; Klapper et al., 1993; Over, 1997; 2002), and this boundary occurs in a regionally continuous bed of black shale that is correlated with the upper Kellwasser Horizon.

Figure 3.1 Inset map showing present day sample locations – 1: Walnut Creek Bank, 2: Irish Gulf, 3: West Valley, 4: Beaver Meadow Creek, 5: Joint Creek. Paleogeography map after Joachimski et al. (2009) showing location of the Appalachian Basin in North America, and the Belgium Frasnian–Famennian (F–F) sections where organic geochemistry is used to infer a wildfire event at F–F boundary (black square; Kahio et al., 2013).

3.3 Methods

The black shale beds that contains the F–F boundary were collected at a 2 – 5 cm stratigraphic interval spacing. The black shale beds above and below the F–F boundary were sampled at a lower resolution of approximately 5 – 10 cm.

3.3.1 Organic petrology, programmed pyrolysis, and total organic carbon analysis

Eighty-seven samples were prepared for petrographic analyses by ASTM D2797 at the U.S. Geological Survey (USGS) in Reston, Virginia using a thermoset plastic briquette mount, which was ground and polished with successively finer abrasives until a 0.05-micrometer (μm) finishing stage. Solid bitumen reflectance analyses (BR_o, %) were collected according to ASTM D7708. Generally, at least 20 measurements of solid bitumen reflectance were collected for each sample, with only 1 measurement per individual rock fragment. Sample briquettes were imaged under oil immersion on a Zeiss AxioImager microscope in white and blue incident light at 500x magnification. A Leica DM4000 microscope equipped with LED illumination and monochrome camera detection was used for solid bitumen reflectance analysis with the computer program DISKUS-FOSSIL by Hilgers Technisches Buero. A YAG calibration standard (0.908% R_o) from Klein and Becker was used. Inertinite reflectance (IR_o, %) was measured with the same method as solid bitumen. Samples were point-counted (300 – 500 points per sample) to determine relative abundances of mineral matter and macerals, which are inertinite, solid bitumen and *Tasmanites* that presented in our sample sets. Bulk geochemical analyses were determined on the powdered samples after crushing with a shatterbox. Bulk analyses included total organic carbon (TOC) content by LECO and Hawk programmed pyrolysis (analyzed at the USGS in Denver, Colorado) using methods outlined in Espitalié et al. (1985).

3.3.2 Re–Os analysis

Rhenium–osmium (Re–Os) analysis was undertaken at the Laboratory for Sulphide and Source Rock Geochronology and Geochemistry of Durham University (UK). Samples were polished to remove any potential weathered surface and drilling marks. All samples were powdered in a Zirconium dish using a shatterbox. Powdered sample (~1 g) and a known amount of spike (^{185}Re and ^{190}Os) were digested in a carius tube with 8 ml of 0.25 g/g CrO_3 in 4 N

H_2SO_4 at 220 °C for 48 h. Rhenium was isolated using NaOH–acetone extraction and anion chromatography. Osmium was isolated by solvent (chloroform) extraction and purified by micro–distillation. The purified Re and Os fractions were analysed via negative thermal ionization mass spectrometry using a Thermo Finnigan TRITON mass spectrometer in the Arthur Holmes Laboratory at Durham University via static Faraday cup for Re and secondary electron multiplier for Os. Total procedural blanks during this study were 12.5 ± 4.5 pg and 0.12 ± 0.06 pg (1σ S.D., n = 3) for Re and Os, respectively, with an average $^{187}Os/^{188}Os$ value of 0.34 ± 0.20 (n = 3). The initial $^{187}Os/^{188}Os$ values were calculated using the following equation:

$$^{187}Os/^{188}Os_{initial} = {}^{187}Os/^{188}Os_{measured} - (^{187}Re/^{188}Os_{measured}*(EXP(\lambda * t)-1))$$

where λ is ^{187}Re decay constant $1.666e^{-11}$ a^{-1} (Smoliar et al., 1996), and t is the F–F boundary age (371.93 Ma; Percival et al., 2018).

3.3.3 Major and trace element analysis

Aliquots of the sample powder prepared for Re–Os analysis were also used for major and trace element analysis. Major and trace element abundance were determined using a Panalytical Zetium X–ray fluorescence (XRF) spectrometer at Department of Geography at Durham University. Major and trace elements were analysed with fused bead and pressed pellet, respectively. For the former, 0.6 g of sample powder and 6 g of flux were used to fuse the bead. The pressed pellet was prepared with 12 g of sample and 3 g of binder. Reproducibility and precision were demonstrated through the repeated analysis of standards (USGS SBC–1, USGS SDO–1). Ranges of uncertainty were less than 1 % for major elements (Si, Al and Ti), less than 10 % for trace elements (Mn, Vi and Ni), and 20 % for Mo.

3.4 Results

3.4.1 Organic petrology and pyrolysis data

Three types of macerals (inertinite, *Tasmanites*, and solid bitumen) were identified in

the samples (Fig. 3.4). Pyrolysis data suggests the dominance of marine organic matter in the samples (Fig. 3.3). Inertinite is observed in all studied sections (Fig. 3.2). Traces of inertinite are identified in samples from the JC section below and above the F–F boundary, however, none were counted due to the low abundance (lower than 0.2 %, volume percent of whole rock, here and after). In the BMC section that represents the second-most proximal paleo-setting in the Appalachian Basin studied herein, the first occurrence of inertinite is within Upper Frasnian strata (0.6 %) and continued upward, reaching a maximum (2.2 %) just below the F–F boundary, after which the inertinite concentration decreased to 0.2 % above the F–F boundary. For the remaining WV, WCB, IG sections that represent a more basinward depositional environment, the first occurrence of inertinite is within the lowest Famennian strata. Inertinite abundance is the WV, IG, and WCB section is 0.2 to 0.4 %, 0.2 to 1 % and 0.2 to 1.2 %, respectively.

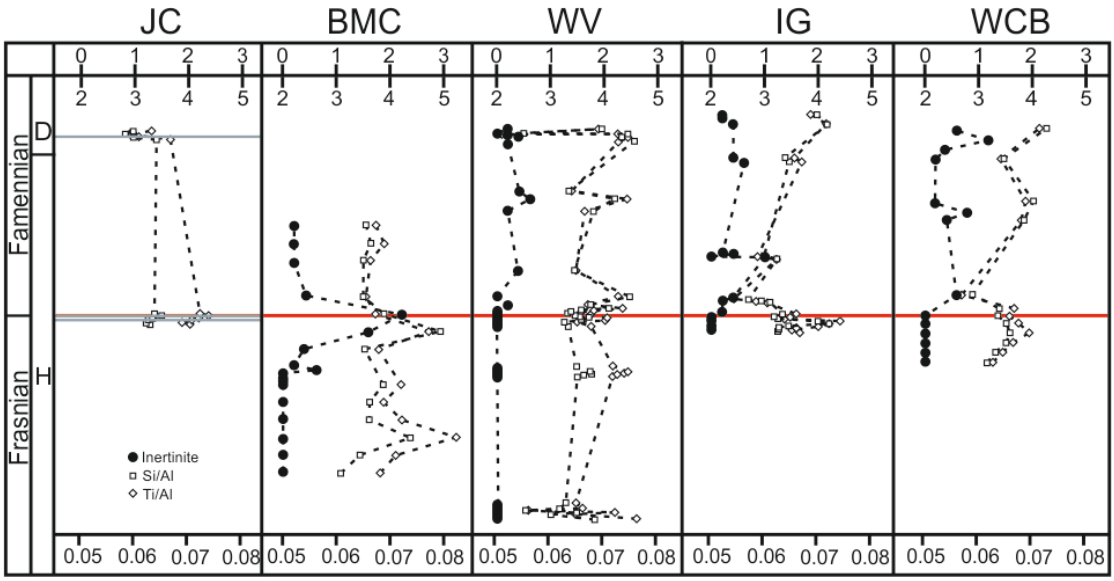

Figure 3.2 Inertinite abundance (black circles) and clastic input proxies (Si/Al, open square; Ti/Al, open diamonds). Inertinite abundance is calculated as volume percent of whole rock basis. H: Hanover Formation, D: Dunkirk Formation; Stratigraphic sections are presented in order of proximity to the paleoshoreline = JC: Joint Creek, BMC: Beaver Meadow Creek, WCB: Walnut Creek Bank, IG: Irish Gulf, WV: West Valley; from proximal to distal: JC, BMC, WV, IG, WCB. Gray bars in the Joint Creek section represent samples that contain inertinite, but the inertinite abundance is too low to be counted. Numbers above the upper scale are for inertinite bundance. Numbers below the upper are for Si/Al. Numbers below the lower scale are for Ti/Al.

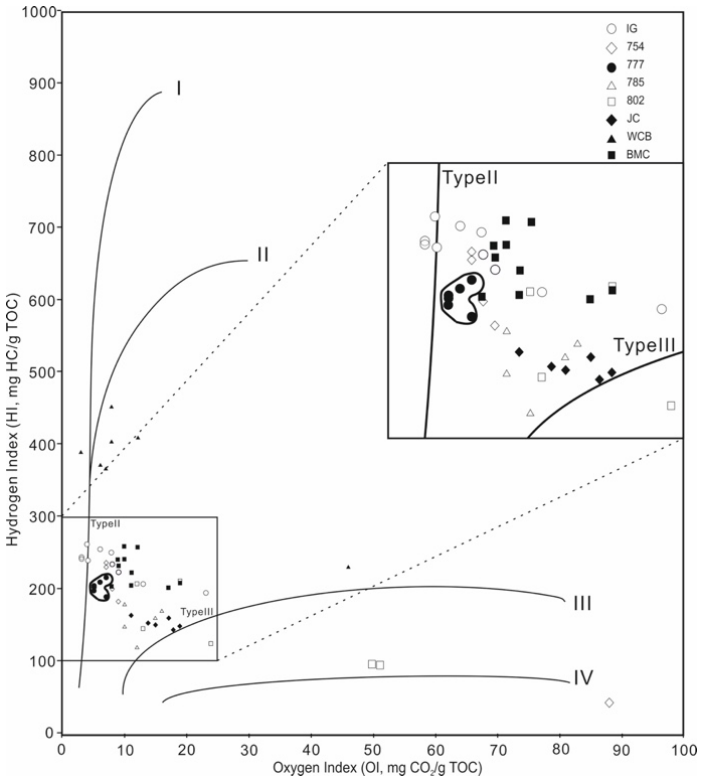

Figure 3.3 Pseudo-Van Krevelen plot (hydrogen index vs. oxygen index) showing kerogen types. Note that for the majority of the samples, the dominant organic matter is solid bitumen, which is not a kerogen.

Solid bitumen reflectance (BR_o, %) and T_{max} data suggest that the samples record a low thermal maturity (%BR_o ~ 0.6, T_{max} ~ 445 °C; appx. Table 3.7 and 3.8). Inertinite reflectance (IR_o) values range from 1.74 – 3.16 % (appx. Table 3.3), and relates to originating from burning temperatures between 400 – 500 °C (Scott and Glasspool, 2007). In hydrogen and oxygen index space (pseudo Van Krevelen plot; Fig. 3.3), the majority of samples are characterized by Type II-III kerogen.

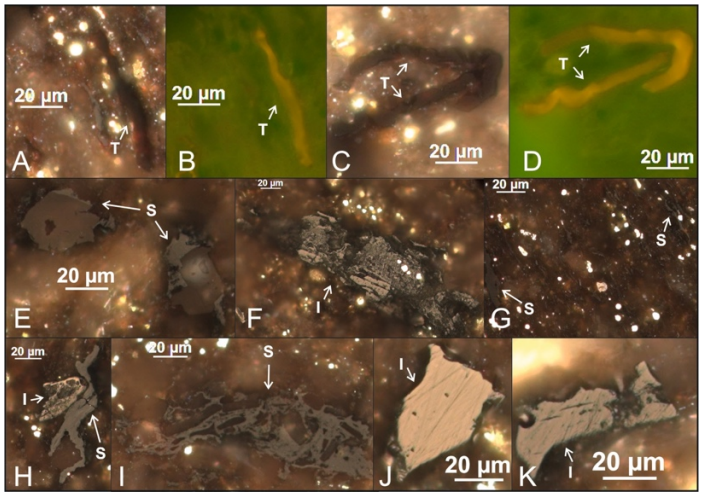

Figure 3.4 Microscopic petrography of macerals through oil immersion. All images, except B and D, are under white light. Images B and D are under blue light. T: *Tasmanites*, S: Solid Bitumen, I: Inertinite.

3.4.2 Results of major and trace element analysis

Trace element abundance and ratios can be reliable proxies for paleo-redox environment (e.g., Mn, Mo, and V/[V+Ni]). The Mn values of all of the samples range from 210 to 630 ppm with a mean value of 322 ppm. The majority of the samples have Mn values ranging from 200 to 400 ppm (Fig. 3.5). The Mo/Al ratio ($2.53 – 34.09 \times 10^{-4}$) exceeds the average shale value (0.32×10^{-4}; Wedepohl, 1971), suggesting authigenic enrichment. Average V/Al ratio (14.41×10^{-4}) and Ni/Al (7.78×10^{-4}) ratios are comparable to those of average shale (14.62×10^{-4} and 7.65×10^{-4} respectively; Wedepohl, 1971). Only a few samples from the F–F interval of BMC and WV sections have Mn values between 400 – 630 ppm, indicating decreased anoxia for the F–F interval relative to the other intervals. The Mo abundance values (4 to 42 ppm, average 18 ppm) represent a non-euxinic to euxinic depositional environment (Fig. 3.5; Scott and Lyons, 2012). The Mo values for the F–F interval were typically less than 15 ppm, suggesting a non-euxinic environment. The V/(V+Ni) values range from 0.50 to 0.74, indicating dysoxic to anoxic conditions (Fig. 3.5; Hatch and Leventhal, 1992). The Mo abundance (4 to 42 ppm, average 18 ppm) across the F–F section coupled the V/(V+Ni) values of 0.50 to 0.74 and intervals of elevated Mn (400 – 630 ppm) are suggestive of decreased anoxia (Fig. 3.5; Hatch and Leventhal, 1992; Scott and Lyons, 2012).

3.4.3 Results of Re–Os analysis

The Re and Os (^{192}Os) abundances, and ^{187}Re/^{188}Os and ^{187}Os/^{188}Os ratios, range from 0.9 to 32 ppb and 48 to 460 ppt (18 to 145 ppt), and 97.46 to 658 and 0.80 to 4.85, respectively, across all the sections. Stratigraphically, no relationships are observed between trace metal redox proxies, Re and Os abundances, ^{187}Re/^{188}Os and initial ^{187}Os/^{188}Os ratios, and TOC values (Fig. 3.5). Further, there is no apparent correlation between the abundance of Re and Os and TOC values

(Fig. 3.6). Initial $^{187}Os/^{188}Os$ (Os_i) compositions are broadly the same across the F–F boundary (Fig. 3.7).

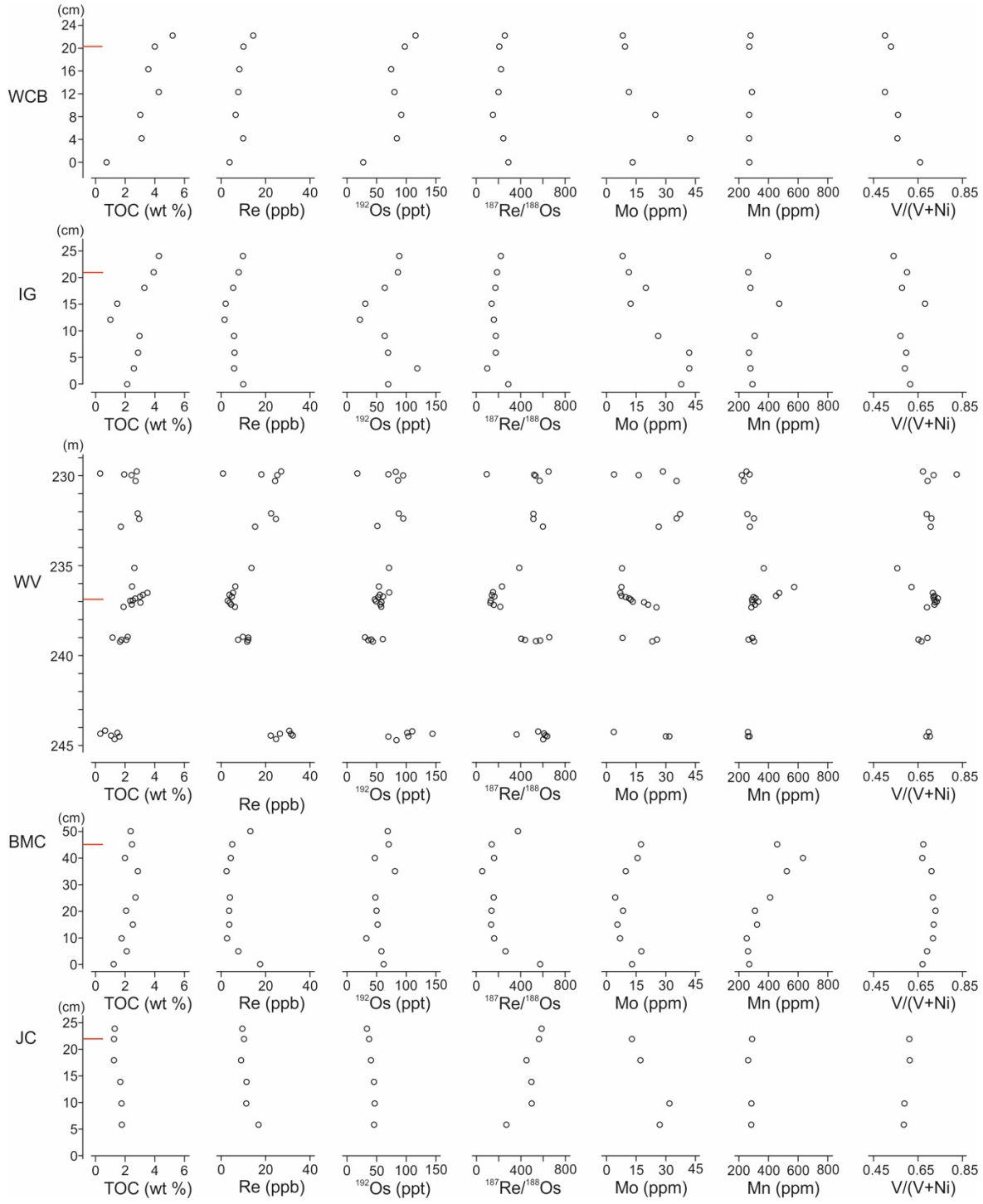

Figure 3.5 Stratigraphical plots of TOC, Re, ^{192}Os, $^{187}Re/^{188}Os$, Mo, Mn, and V/(V+Ni). Red line indicates the F–F boundary. No relationships are observed between trace metal redox proxies, Re and ^{192}Os abundances, $^{187}Re/^{188}Os$, and TOC values.

Samples with the same amount of TOC possess significant variation in their Re and Os abundances (up to 30 times for Re and 6 times for Os). At the F–F boundary, the ^{192}Os/TOC ratios for each section are generally identical, but the Re/TOC ratios vary greatly. Overall, no linear relationship exists for Re/TOC and ^{192}Os/TOC. The West Valley 777 unit (F–F boundary) exhibits very limited Re/Os fractionation (~20 units) whereas the other three units above and below the F–F boundary and other F–F sections exhibit a relatively large range in ^{187}Re/^{188}Os values (200–400). In terms of organic matter composition, the 777 unit is dominated by solid bitumen (~90 %) and has the most limited spread in the HI–OI index plot compared with the other sections (Figs. 3.3 and 3.8). The other sections have more variable organic matter composition, especially the JC section (the most proximal section), which shows the largest ^{187}Re/^{188}Os fractionation. High Re and ^{192}Os abundances are present only in strata that are interpreted as having accumulated in a highly reduced environment (Fig. 3.5). However, samples that are interpreted as having accumulated in reduced environments also have low Re and Os abundances (Fig. 3.5). The ^{187}Re/^{188}Os values are variable within one redox environment and the ^{187}Re/^{188}Os values and their variablity decrease with an increase in oxygen in the water column (Fig. 3.5). The OI values are predominantly below 20 and show no specific relationship with ^{187}Re/^{188}Os within or across the studied locations (Fig. 3.8). There is no correlation between Re and ^{192}Os abundances and Mo concentration (Fig. 3.5). The overall ^{187}Re/^{188}Os values show no clear correlation with the clastic input proxies (Si/Al and Ti/Al). However, when each F–F section is investigated individually, ^{187}Re/^{188}Os values have a negative correlation with the clastic input proxies. The samples with more clastic input exhibit a correlation with lower ^{187}Re/^{188}Os values in that section (Fig. 3.9).

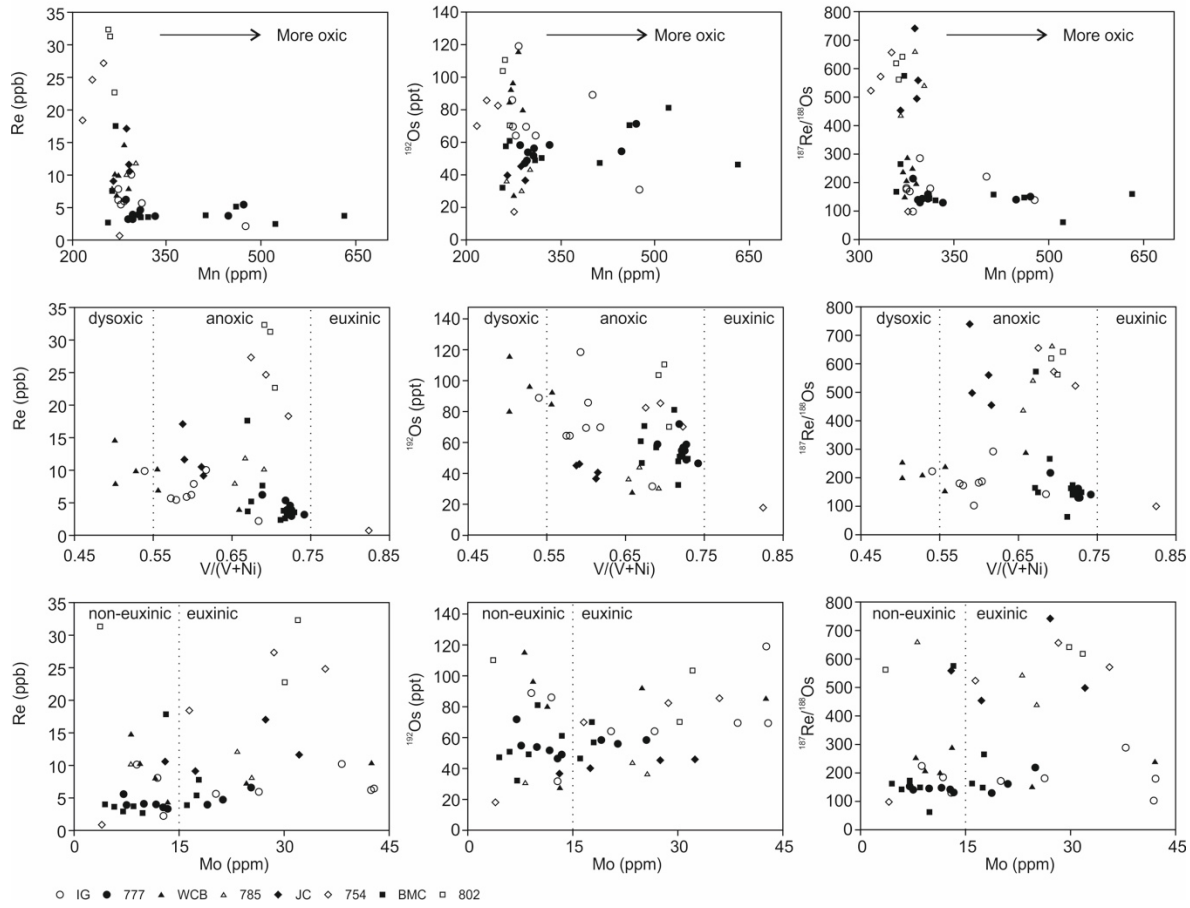

Figure 3.6 Plots of Re, ^{192}Os and ^{187}Re/^{188}Os versus Mn, Mo, and V/(V+Ni) for the JC: Joint Creek, BMC: Beaver Meadow Creek, WCB: Walnut Creek Bank, IG: Irish Gulf, and WV: West Valley sections.

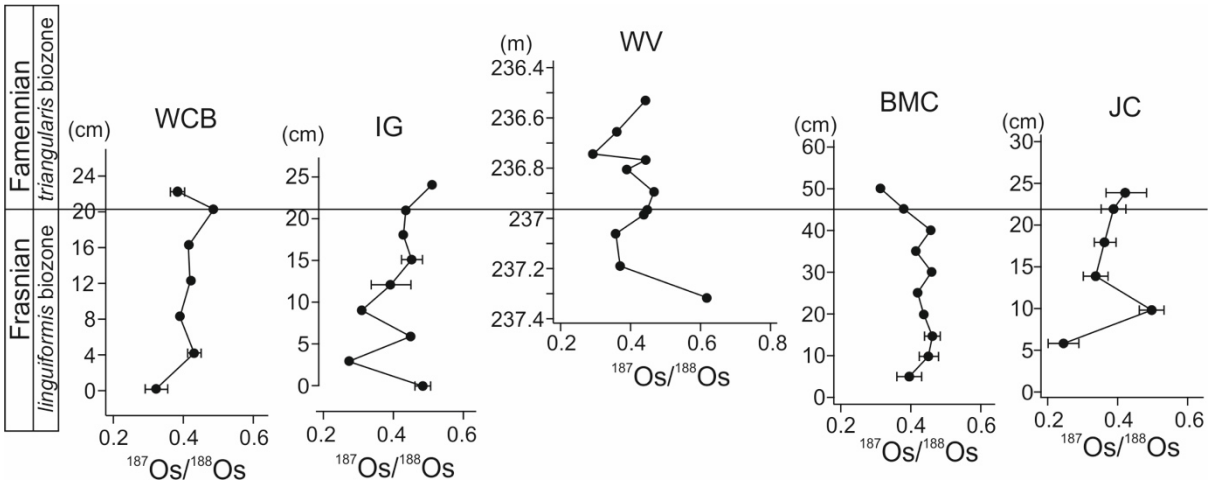

Figure 3.7 Initial ^{187}Os/^{188}Os isotope stratigraphy for the Frasnian–Famennian interval in New York. Sections are presented in order of proximity to the paleoshoreline = JC: Joint Creek, BMC: Beaver Meadow Creek, WCB: Walnut Creek Bank, IG: Irish Gulf, WV: West Valley; from proximal to distal: JC, BMC, WV, IG, WCB. Biostratigraphy constraints are from Klapper et al. (1993) and Over (1997, 2002). Typically the range of uncertainty (2σ) of the initial ^{187}Os/^{188}Os is smaller than the symbol size.

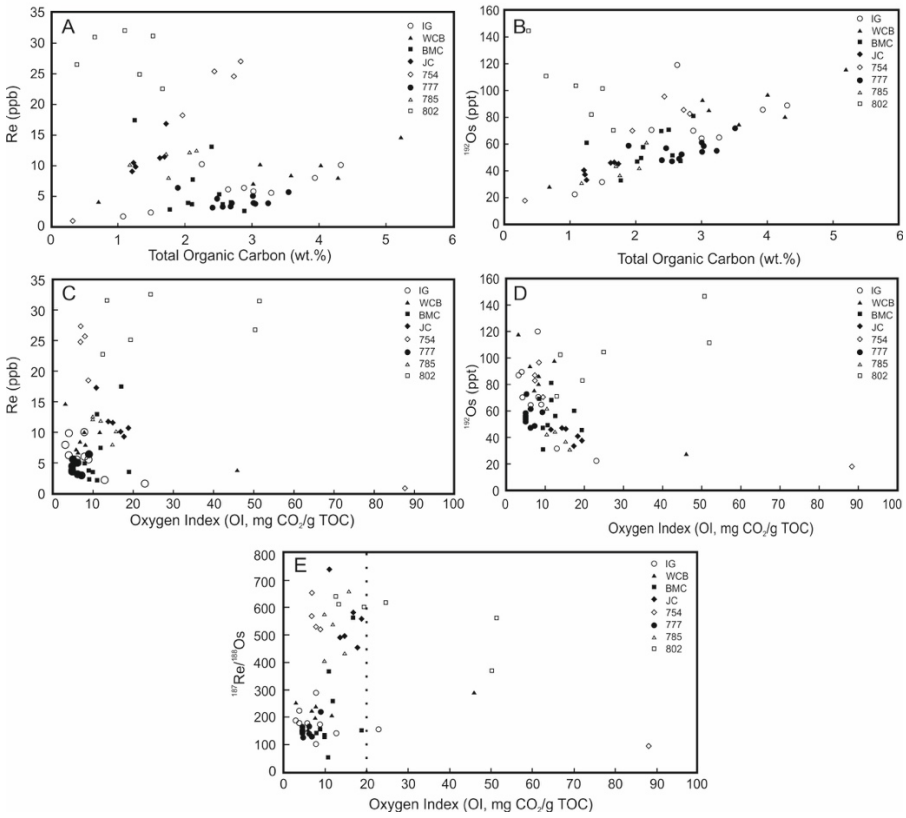

Figure 3.8 Plots of total organic carbon (TOC) versus Re (A) and ^{192}Os (B), and plots of oxygen index (OI) versus Re (C), ^{192}Os (D), and ^{187}Re/^{188}Os (E) for the JC: Joint Creek, BMC: Beaver Meadow Creek, WCB: Walnut Creek Bank, IG: Irish Gulf, and WV: West Valley sections.

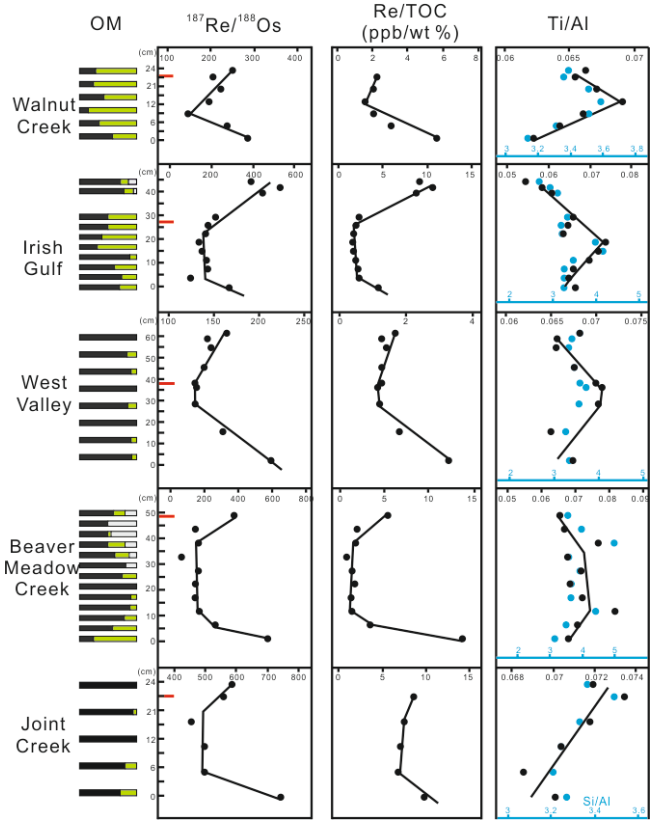

Figure 3.9 Summary of results from organic matter (OM) analysis, Re/TOC ratios, and clastic input proxies (Ti/Al and Si/Al). OM color represents organic matter types. Green: *Tasmanites*, black: Solid bitumen, gray: Inertinite. Red bar represents the Frasnian–Famennian boundary.

3.5 Discussion

3.5.1 Wildfire and fire type

Inertinite as a record of wildfire events can provide vital implications for the evolution of Earth systems and the level of atmospheric oxygen (Glasspool and Scott, 2010; Scott and Glasspool, 2006). The stratigraphic occurrence and relative enrichment of inertinite within each section could be controlled by proximity of the depositional site to a terrigenous source. The proximal sections have increased inertinite abundance relative to the distal sections and this may be caused by increased detrital input. However, overall the inertinite has no obvious relationship with the clastic input proxies (e.g., Ti/Al, Si/Al; Fig. 3.2). The inertinite abundance thus suggests a wildfire event occurred at the Frasnian–Famennian interval (Glasspool and Scott, 2010).

Wildfires can be divided into the following three groups: 1) ground fire 2) surface fire; and 3) crown fire; with different burning material and different burning temperatures. Inertinite reflectance is related to the burning temperature as shown by experimental analysis (Scott, 2000; Scott and Glasspool, 2005; Scott and Glasspool, 2007). Based on experimental data, the inertinite reflectance values reported here (1.74 – 3.16 %) correlate to burning temperatures between 400 – 500 °C (Scott and Glasspool, 2007). This temperature range is indicative of a surface fire, suggesting that the fuel type across the F–F boundary interval would have mainly been herbaceous and shrubby plants (Cressler, 2001; Hudspith et al., 2014).

3.5.2 Implication for the rise of atmospheric O_2 level during the early Late Devonian

A wildfire event depends on the combination of fuel and O_2 and the source of heat. Throughout geological time, lightning is considered to be the most common source of heat for ignition (Scott and Glasspool, 2006). However, the correlation of the mercury data with inertinite abundance within the F–F

interval may suggest that the volcanism may have acted as a source of ignition (Racki et al., 2018). The expansion of terrestrial vegetation (forest) during the Middle Devonian gave rise to a potential ready supply of fuel that could be ignited (Kenrick and Crane, 1997; Stein et al., 2012). However, the hitherto absence of evidence of a fossilized charcoal record, specifically during the Late Frasnian to Early Famennian (this study), has resulted in the prediction of low levels of atmospheric O_2 (17 %) during this time interval (Berner, 2003; Rimmer et al., 2015; Scott and Glasspool, 2006). In contrast, the presence of abundant inertinite (average 11.9 %, volume percentage on a mineral-free basis; this study), provides evidence for wildfires and suggests higher atmospheric O_2 levels during the Latest Frasnian.

Glasspool and Scott (2010) provided an equation to calculate the atmospheric oxygen level, plus uncertainty, from percentage inertinite abundance. The best estimation is given by:

$$pO_2 = 18.113 * (\text{Inert}\%^{0.1273}) \quad (1)$$

where Inert% is the mean value of volume percent of inertinite abundances on a mineral-matter-free basis. And the 1 standard deviation (s.d.) uncertainty is given by:

$$pO_2 = 19.293 * (\text{Inert}\%^{0.1376}) \quad (2)$$

$$pO_2 = 17.723 * (\text{Inert}\%^{0.1185}) \quad (3)$$

where the mean inertinite abundance value as (1) are used for (2) and (3).

The maximum uncertainty (shaded area in Fig. 3.10) is given by:

$$pO_2 = 18.633 * (\text{Inert}\%^{0.0985}) \quad (4)$$

$$pO_2 = 17.998 * (\text{Inert}\%^{0.1427}) \quad (5)$$

using mean – 1 s.d. value for (4) and mean + 1 s.d. for (5). Results of these calculations are listed in appx. Table 3.2.

The average inertinite volume percentage data (11.9 %) estimate the pO_2 level for the F–F boundary interval to be 24.8 %. Even though this pO_2 level might be an overestimate, because not every inertinite may represent fossilized charcoal (Rimmer et al., 2015), the pO_2 value is in agreement with the proposed higher estimated value pO_2 (~20 – 21 %; Glasspool and Scott; 2010) (Fig. 3.10). As such the

atmospheric O_2 level may have reached the present level (21 %) by the Latest Frasnian – Early Famennian (Berner et al., 2003; Berner, 2009), rather than during the Early Mississippian as predicted by previous models (Berner et al, 2006; Berner, 2009).

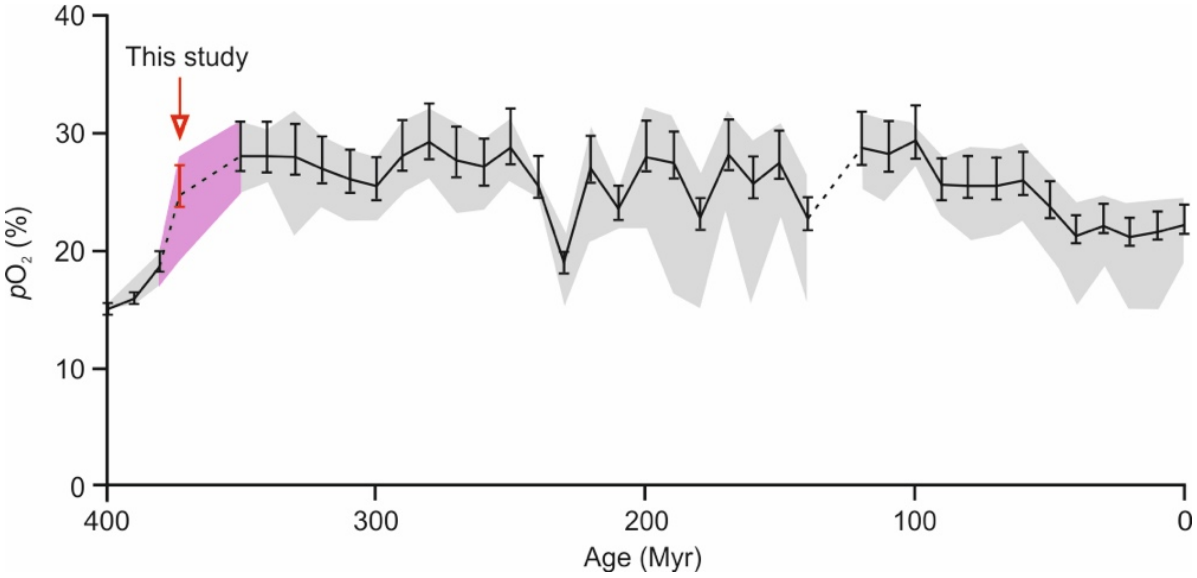

Figure 3.10 Modelled pO_2 level from inertinite abundance modified after Glasspool and Scott (2010). See text for discussion. Line; best estimate on the basis of late Palaeozoic pO_2 maxima of 30%. Ranges of uncertainty ("error bars") are 1 standard deviation (s.d.) from mean. Shaded area; estimate of maximum uncertainty ("error") assuming Phanerozoic pO_2 maxima of 35 % + 1 s.d. (upper margin) and 25 % - 1 s.d. (lower margin).

Additionally, during the F–F interval the atmospheric O_2 level may have been affected by the enhanced orogeny activity coupled with sea-level fall that may have caused increased continental weathering and organic carbon burial (Averbuch et al., 2003; Berner et al., 2003; Bond and Wignall, 2008; Johnson et al., 1985). The latter, in turn, could have driven an increased nutrition flux to the oceans that would have boosted marine productivity, and led to elevated carbon burial and pCO_2 drawdown (Berner et al., 2003; Huang et al., 2018). All these factors together may have resulted in the elevating the atmospheric O_2 level (Berner et al., 2003; Huang et al., 2018). Interestingly, the timing of higher O_2 levels within the F–F interval correlates with the radiation of vascular plants and evolution of large animals with a higher O_2 demand (Dahl et al., 2010).

3.5.3 Implications for the Frasnian–Famenian mass extinction

The F–F mass extinction has been proposed to have been triggered by an impact and (or) volcanism (Claeys and Casier, 1994; Racki et al., 2018). Volcanism interpreted from Hg data (Racki et al., 2018) and associated weathering of mafic material would have resulted in the delivery of unradiogenic osmium to the ocean that would have caused an unradiogenic excursion in the marine osmium isotope record (Peucker-Ehrenbrink and Ravizza, 2000). However, previous Os-isotope data (Gordon et al., 2009; Percival et al., 2019; Turgeon et al., 2007), together with the data presented in this paper, show no evidence of an unradiogenic osmium isotope excursion (Fig. 3.7). A possible scenario is that the Hg was not injected into the atmosphere directly from volcanic degassing, but derived from the thermal alteration of organic rich layers during magma emplacement (Svensen et al., 2004). Further, as previously stated (Gordon et al., 2009; Percival et al., 2019; Turgeon et al., 2007) our Os isotope records do not support the impact scenario either, as a impact body would also result in an unradiogenic Os excursion of the marine osmium isotope record (Peucker-Ehrenbrink and Ravizza, 2000). Nevertheless, it is not possible to rule out the scenario of a comet impactor with a very limited meteoritic dust budget that left no elemental spike in the geological record (Jansa, 1993). To date evidence for a wildfire during the F–F interval is supported by organic geochemistry proxy data (coronene, benzo(ghi)perylene and benzo(e)pyrene) from two sections in Belgium that represent deposition in an epicontinental setting on the southern periphery of the Laurussian continent (Fig. 3.1, Kaiho et al., 2013). However, this wildfire scenario is questioned by possible secondary process (such as weathering) causing the maxima of the combustion proxies and the discrepancy between the lack of charcoal record and high combustion proxies (Marynowski and Racki, 2015; Kaiho, 2015). Although inertinite may originate from processes (e.g., organic matter degradation by bacterial and fungal activity) other than a wildfire (Rimmer et al., 2015), it is unlikely that these processes are the sole cause of all the inertinite observed in this study (Scott and Glasspool, 2007; Glasspool and Scott, 2010 and references therein). Therefore,

the inertinite data from the New York sections (this study), and potentially the coronene, benzo(ghi)perylene and benzo(e)pyrene data from Belgium suggest a potential wildfire event across the F–F boundary interval. However, at which scale did the wildfire burn and to what extent did it contribute to the biotic crisis require further research. However, our evidence of elevated O_2 level supports the hypothesis of enhanced mountain-building and continent-weathering that, in turn, may have lead to increased marine productivity and carbon burial that resulted in the drawdown of pCO_2 (Averbuch et al., 2003; Berner et al., 2003, Percival et al., 2019). In turn, the pCO_2 drawdown and associated climate cooling may have caused the F–F biotic crisis (Averbuch et al., 2003; Berner et al., 2003; Huang et al., 2018).

3.5.4 Further insights to $^{187}Re/^{188}Os$ fractionation in organic-rich sedimentary rocks

In addition to the evaluation and implications of O_2 levels throughout the F–F interval, the organic petrology and geochemistry, coupled with the major and trace element provide further insight to the fractionation of Re and Os in organic-rich sedimentary rocks. Our data suggest that Re and Os fractionation has no relationship with the redox/euxinic environment (Figs. 3.5 and 3.6) and thus excludes deposition under reduced oxygen conditions as the cause of Re and Os fractionation (Selby et al., 2009; Harris et al., 2013). The correlation of $^{187}Re/^{188}Os$ ratios with the terrestrial input proxies (Si/Al and Ti/Al) in each section suggests that a more variable depositional environment is likely to have yielded more variable Re and Os fractionation (Fig. 3.9). Samples with homogeneous organic matter composition have relatively limited Re and Os fractionation (Figs. 3.3 and 3.9). In contrast, the other samples sets that have more variable organic matter composition have larger Re and Os fractionations (Figs. 3.3 and 3.9). This suggest that the organic matter composition/type and its variability may be the mechanism that controls Re and Os fractionation. These findings concur with the findings from previous research that a variable deposition environment together with heteorgenous organic matter composition may control the Re and Os fractionation (Cumming

et al., 2012; Harris et al., 2013).

3.6 Conclusions

The presence of inertinite in the Upper Devonian strata within the F–F boundary interval suggests a wildfire event occurred at this time. The inertinite data also provide an estimate of the O_2 level (~ 25 %) that is much higher and ~25 Myrs earlier than previously estimated. Additionally, the Os isotope records do not provide any evidence of extraterrestrial impact event or volcanic activity as a trigger for the F–F mass extinction. However, the size of the wildfire and the possible link with the F–F mass extinction still need further research. Our estimated high O_2 level supports the hypothesis that pCO_2 drawdown and associated climate cooling may have played an important role in the F–F biotic crisis.

3.7 References

ASTM, D2797 Standard practice for preparing coal samples for microscopical analysis by reflected light. In Petroleum products, lubricants, and fossil fuels; Gaseous fuels; coal and coke, sec. 5, v. 05.06, ASTM International: West Conshohocken, PA, 2015.

ASTM, D7708 Standard test method for microscopical determination of the reflectance of vitrinite dispersed in sedimentary rocks. In Petroleum products, lubricants, and fossil fuels; Gaseous fuels; coal and coke, sec. 5, v. 05.06, ASTM International: West Conshohocken, PA, 2015.

Averbuch, O., Tribovillard, N., Devleeschouwer, X., Riquier, L., Mistiaen, B., van Vliet-Lanoe, B., 2005. Mountain building-enhanced continental weathering and organic carbon burial as major causes for climatic cooling at the Frasnian-Famennian boundary (c. 376 Ma)? Terra Nova 17, 25-34.

Berner, R. A., 2006, GEOCARBSULF: A combined model for Phanerozoic atmospheric O_2 and CO_2. Geochimica et Cosmochimica Acta 70, 5653-5664.

Berner, R. A., 2009, Phanerozoic atmospheric oxygen: New results using the GEOCARBSULF model. American Journal of Science 309, 603-606.

Berner, R. A., Beerling, D. J., Dudley, R., Robinson, J. M., Wildman, R. A., 2003. Phanerozoic atmospheric oxygen. Annual Review of Earth and Planetary Sciences 31, 105-134.

Bond, D., Wignall, P. B., Racki, G., 2004. Extent and duration of marine anoxia during the Frasnian–Famennian (Late Devonian) mass extinction in Poland, Germany, Austria and France. Geological Magazine 141, 173-193.

Bond, D. P. G., Wignall, P. B., 2008. The role of sea-level change and marine anoxia in the Frasnian–Famennian (Late Devonian) mass extinction. Palaeogeography, Palaeoclimatology, Palaeoecology 263, 107-118.

Claeys, P., Casier, J. G., Margolis, S. V., 1992. Microtektites and Mass Extinctions: Evidence for a Late Devonian Asteroid Impact. Science 257, 1102-1104.

Claeys, P., Casier, J. G., 1994. Microtektite-like impact glass associated with the Frasnian-Famennian boundary mass extinction. Earth and Planetary Science Letters 122, 303-315.

Cressler, W. L., 2001, Evidence of earliest known wildfires. Palaios 16, 171-174.

Cumming, V. M., Selby, D., Lillis, P. G., 2012. Re–Os geochronology of the lacustrine Green River Formation: Insights into direct depositional dating of lacustrine successions, Re–Os systematics and paleocontinental weathering. Earth and Planetary Science Letters 359, 194-205.

Dahl, T. W., Hammarlund, E. U., Anbar, A. D., Bond, D. P. G., Gill, B. C., Gordon, G. W., Knoll, A. H., Nielsen, A. T., Schovsbo, N. H., and Canfield, D. E., 2010, Devonian rise in atmospheric oxygen correlated to the radiations of terrestrial plants and large predatory fish. Proceedings of the National Academy of Sciences 107, 17911-17915.

Espitalié, J.; Deroo, G.; Marquis, F., 1985, Rock-Eval pyrolysis and its applications. Revue de l'Institut français du Pétrole 40, 563-579.

Glasspool, I. J., Scott, A. C., 2010. Phanerozoic concentrations of atmospheric oxygen reconstructed from sedimentary charcoal. Nature Geoscience 3, 627-630.

Gordon, G.W., Rockman, M., Turekian, K.K., Over, J., 2009. Osmium isotopic evidence against an impact at the Frasnian-Famennian boundary. 309, 420-430.

Harris, N.B., Mnich, C.A., Selby, D., Korn, D., 2013. Minor and trace element and Re–Os chemistry of the Upper Devonian Woodford Shale, Permian Basin, west Texas: Insights into metal abundance and basin processes. Chemical Geology 356, 76-93.

Hatch, J. R., Leventhal, J. S., 1992. Relationship between inferred redox potential of the depositional environment and geochemistry of the Upper Pennsylvanian (Missourian) Stark Shale Member of the Dennis Limestone, Wabaunsee County, Kansas, U.S.A. Chemical Geology 99, 65-82.

Huang, C., Joachimski, M.M., Gong, Y., 2018. Did climate changes trigger the Late Devonian Kellwasser Crisis? Evidence from a high-resolution conodont $\delta^{18}O_{PO4}$ record from South China. Earth and Planetary Science Letters 495, 174-184.

Hudspith, V. A., Belcher, C. M., Yearsley, J. M., 2014. Charring temperatures are driven by the fuel types burned in a peatland wildfire. Frontiers in Plant Science 5, 1-12.

Jansa, L. F., 1993. Cometary impacts into ocean: their recognition and the threshold constraint for biological extinctions. Palaeogeography, Palaeoclimatology, Palaeoecology 104, 271-286.

Joachimski, M. M., Breisig, S., Buggisch, W., Talent, J. A., Mawson, R., Gereke, M., Morrow, J. R., Day, J., Weddige, K., 2009. Devonian climate and reef evolution: Insights from oxygen isotopes in apatite. Earth and Planetary Science Letters 284, 599-609.

Joachimski, M. M., Buggisch, W., 2002. Conodont apatite $\delta^{18}O$ signatures indicate climatic cooling as a trigger of the Late Devonian mass extinction. Geology 30, 711-714.

Johnson, J. G., Klapper, G., Sandberg, C. A., 1985. Devonian eustatic fluctuations in Euramerica. Geological Society of America Bulletin 96, 567-587.

Kaiho, K., Yatsu, S., Oba, M., Gorjan, P., Casier, J.-G., Ikeda, M., 2013. A forest fire and soil erosion event during the Late Devonian mass extinction. Palaeogeography, Palaeoclimatology, Palaeoecology 392, 272-280.

Kaiho, K., 2015. Reply to the comment on Kaiho et al., "A forest fire and soil erosion event during the Late Devonian mass extinction" [Palaeogeogr. Palaeoclimatol. Palaeoecol. 392 (2013): 272–280]. Palaeogeography, Palaeoclimatology, Palaeoecology 417, 573-575.

Kenrick, P., Crane, P. R., 1997. The origin and early evolution of plants on land. Nature 389, 33.

Klapper, G., Feist, R., Becker, R. T., House, M. R., 1993. Definition of the Frasnian Famennian Stage Boundary. Episodes 16, 433-441.

Marynowski, L., Racki, G., 2015. Comment on the Kaiho et al., paper "A forest fire and soil erosion event during the Late Devonian mass extinction" [Palaeogeography, Palaeoclimatology, Palaeoecology 392 (2013): 272–280]. Palaeogeography, Palaeoclimatology, Palaeoecology 417, 569-572.

Over, D. J., 1997. Conodont biostratigraphy of the Java Formation (Upper Devonian) and the Frasnian-Famennian boundary in western New York State, *in* Klapper, G., Murphy, M. A., and Talent, J. A., eds., Paleozoic Sequence Stratigraphy, Biostratigraphy, and Biogeography: Studies in Honor of J. Granville ("Jess") Johnson, Geological Society of America 321, 161-177.

Over, D. J., 2002. The Frasnian/Famennian boundary in central and eastern United States. Palaeogeography, Palaeoclimatology, Palaeoecology 181, 153-169.

Percival, L.M.E., Davies, J.H.F.L., Schaltegger, U., De Vleeschouwer, D., Da Silva, A.C., Föllmi, K.B., 2018. Precisely dating the Frasnian–Famennian boundary: implications for the cause of the Late Devonian mass extinction. Scientific Reports 8, 9578.

Percival, L.M.E., Selby, D., Bond, D.P.G., Rakociński, M., Racki, G., Marynowski, L., Adatte, T., Spangenberg, J.E., Föllmi, K.B., 2019. Pulses of enhanced continental weathering associated with multiple Late Devonian climate perturbations: Evidence from osmium-isotope compositions. Palaeogeography, Palaeoclimatology, Palaeoecology.

Peucker-Ehrenbrink, B., Ravizza, G., 2000. The marine osmium isotope record. Terra Nova 12, 205-219.

Racki, G., Rakociński, M., Marynowski, L., and Wignall, P. B., 2018, Mercury enrichments and the Frasnian-Famennian biotic crisis: A volcanic trigger proved?. Geology 46, 543-546.

Rimmer, S. M., Hawkins, S. J., Scott, A. C., Cressler, W. L., 2015. The rise of fire: Fossil charcoal in late Devonian marine shales as an indicator of expanding terrestrial ecosystems, fire, and atmospheric change. American Journal of Science 315, 713-733.

Sageman, B.B., Murphy, A.E., Werne, J.P., Ver Straeten, C.A., Hollander, D.J., Lyons, T.W., 2003. A tale of shales: the relative roles of production, decomposition, and dilution in the accumulation of organic-rich strata, Middle–Upper Devonian, Appalachian basin. Chemical Geology 195, 229-273.

Scott, A. C., 2000. The pre-Quaternary history of fire. Palaeogeography, Palaeoclimatology, Palaeoecology 164, 281-329.

Scott, A. C., Glasspool, I. J., 2005. Charcoal reflectance as a proxy for the emplacement temperature of pyroclastic flow deposits. Geology 33, 589-592.

Scott, A. C., Glasspool, I. J., 2006. The diversification of Paleozoic fire systems and fluctuations in atmospheric oxygen concentration. Proceedings of the National Academy of Sciences 103, 10861-10865.

Scott, A. C., and Glasspool, I. J., 2007. Observations and experiments on the origin and formation of inertinite group macerals. International Journal of Coal Geology 70, 53-66.

Scott, C., Lyons, T. W., 2012. Contrasting molybdenum cycling and isotopic properties in euxinic versus non-euxinic sediments and sedimentary rocks: Refining the paleoproxies. Chemical Geology 324, 19-27.

Selby, D., Mutterlose, J., Condon, D. J., 2009. U–Pb and Re–Os geochronology of the Aptian/Albian and Cenomanian/Turonian stage boundaries: Implications for timescale calibration, osmium isotope seawater composition and Re–Os systematics in organic-rich sediments. Chemical Geology 265, 394-409.

Smoliar, M. I., Walker, R. J., Morgan, J. W., 1996. Re-Os ages of group IIA, IIIA, IVA, and IVB iron meteorites. Science 271, 1099.

Stanley, S. M., 2016. Estimates of the magnitudes of major marine mass extinctions in earth history. Proceedings of the National Academy of Sciences 113, E6325-E6334.

Stein, W.E., Berry, C.M., Hernick, L.V., Mannolini, F., 2012. Surprisingly complex community discovered in the mid-Devonian fossil forest at Gilboa. Nature 483, 78.

Svensen, H., Planke, S., Malthe-Sørenssen, A., Jamtveit, B., Myklebust, R., Rasmussen Eidem, T., Rey, S. S., 2004. Release of methane from a volcanic basin as a mechanism for initial Eocene global warming. Nature 429, 542.

Turgeon, S. C., Creaser, R. A., Algeo, T. J., 2007. Re–Os depositional ages and seawater Os estimates for the Frasnian–Famennian boundary: Implications for weathering rates, land plant evolution, and extinction mechanisms. Earth and Planetary Science Letters 261, 649-661.

Wedepohl, K. H., 1971. Environmental influences on the chemical composition of shales and clays. Physics and Chemistry of the Earth 8, 307-333.

Chapter 4

Climate Perturbations of the Paleocene–Eocene Thermal Maximum Driven by Comet Impact and Volcanism*

*A version of this chapter has been submitted to Geology co-authored with Daniel E. Horton, Clay Tabor, Bradley B. Sageman, Lawrence M. E. Percival, Benjamin C. Gill and David Selby.

4.1 Introduction

The Paleocene–Eocene Thermal Maximum (PETM, ~55.9 Ma) was characterized by the rapid release of several thousand gigatons (≥ 3,000–10,000 Gt) of isotopically light carbon into the ocean and atmosphere, causing rapid global warming (Gingerich, 2003; Gutjahr et al., 2017; Schmitz and Pujalte, 2003; Wing et al., 2005; Wright and Schaller, 2013; Zachos et al., 2001; Zeebe et al., 2009). The main evidence for this carbon-cycle perturbation is a negative excursion in the carbon-isotope composition of both organic and inorganic matter (up to 3 ‰) in global PETM stratigraphic records (Bowen et al., 2015; Gutjahr et al., 2017; Wright and Schaller, 2013; Zachos et al., 2001; Zeebe et al., 2009). Commonly proposed sources of the carbon include volcanic gas emissions related to the emplacement of the North Atlantic Igneous Province (NAIP; Gutjahr et al., 2017; Saunders, 2016), metamorphism of organic-rich rocks by magmatic sills (Svensen et al., 2004), melting of methane hydrates and/or permafrost (DeConto et al., 2012; Dickens et al., 1995), and oxidation of marine sedimentary organic matter (Higgins and Schrag, 2006). An extraterrestrial impact has also been proposed as an alternative/additional contributor to the PETM, with iridium (Ir) enrichments identified in Western Slovenia (Dolenec et al., 2000) and Zumaya, Spain (Schmitz et al., 1997). Although these Ir anomalies have also been interpreted to be of volcanic origin (Schmitz et al., 2004), additional support for an extraterrestrial impact during the Paleocene–Eocene (P–E) transition was recently interpreted based on glass spherules (microtektites and microkrystites) and

shocked-quartz found at the base of the negative carbon-isotope excursion (CIE) in three stratigraphic records from the North Atlantic Ocean - Wilson Lake and Millville, New Jersey – both expanded continental shelf sites with organic-rich silty sediments (ODP 174AX: Schaller et al., 2016); and Blake Nose - a condensed sequence of carbonate-rich pelagic sediments (ODP Hole 1051B; Schaller et al., 2016).

To further investigate the potential roles and temporal relationships of the proposed volcanism and impact events, we present new high-resolution osmium isotope (Os_i) stratigraphy from the PETM interval of the Millville and Blake Nose cores (see Fig. 4.1), coupled with mercury (Hg), pyrite sulfur (S), platinum group element (PGE: Pt-Pd-Ir-Ru) and Total Organic Carbon (TOC) data. We also present an Earth system model simulation to investigate the climate feedbacks resulting from sulfur emissions associated with the postulated impact event.

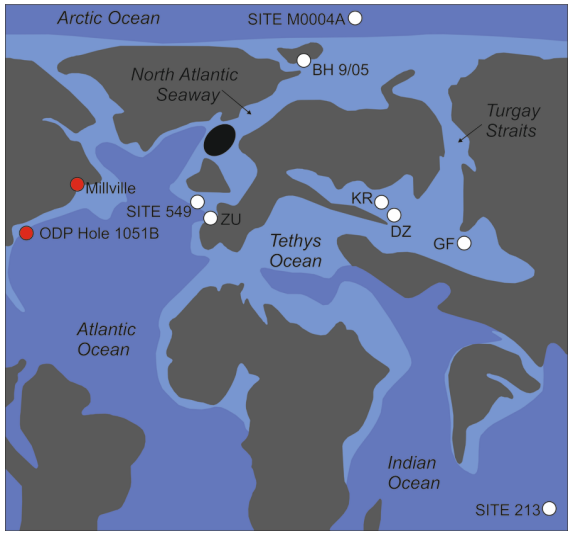

Figure 4.1 Map of sample locations. Red circles are for this study and white circles are for previous studies (Dickson et al., 2015; Wieczorek et al., 2013). KR: Kheu River, Karbardino-Balkaria; DZ: Dzhengutay, Dagestan; GF: Guru-Fatima, Tajikistan; ZU: Zumaya, Spain; site numbers refer to Deep Sea Drilling Program (Sites 213 and 549) and Integrated Ocean Drilling Program (Site M0004A) cores. The black ellipse represents the zone of transient uplift associated with the North Atlantic Igneous Province mantle plume. Base map after Dickson et al. (2015).

4.2 Methods

Before crushing, all samples were polished to eliminate contamination from cutting and drilling marks. The samples were then air dried at 60°C for ~12 hours, broken into chips with no metal contact. Samples were crushed to a fine powder (~30 μm) in a Zirconia ceramic dish using a shatterbox.

4.2.1 Re–Os analysis

Re–Os isotope analysis was carried out at the Durham Geochemistry Centre (Laboratory for Sulphide and Source Rock Geochronology and Geochemistry) at Durham University. For sample digestion, a Cr^{VI}–H_2SO_4 solution was employed to preferentially dissolve the organic fraction of the samples and thus liberate hydrogenous Re and Os, avoiding the contamination from detrital Re and Os (Selby and Creaser, 2003). About 1 g sample powder with a known amount of ^{190}Os and ^{185}Re tracer (spike) solution and 8 ml of 0.25 g/g Cr^{VI}–H_2SO_4 solution were digested in a sealed carius tube for 48 h at 220°C. Rhenium was isolated from the acid using NaOH-C_3H_6O solvent extraction and then purified by anion chromatography. Osmium was purified using solvent extraction ($CHCl_3$), micro-distillation and anion chromatography methods. The isolated Re and Os fractions were loaded onto Ni and Pt filaments, respectively (Selby et al., 2007). Isotopic measurements were determined by using negative thermal ionization mass spectrometry (N-TIMS) (Creaser et al., 1991) in the Arthur Holmes Laboratory at Durham University.

Total procedural blanks during this study were 12.5 ± 4.5 pg and 0.12 ± 0.06 pg (1σ S.D., n = 3) for Re and Os, respectively, with an average $^{187}Os/^{188}Os$ value of 0.34 ± 0.20 (n = 3).

The initial $^{187}Os/^{188}Os$ were calculated using the equation:

$$^{187}Os/^{188}Os_{initial} = {}^{187}Os/^{188}Os_{measured} - (^{187}Re/^{188}Os_{measured}*(EXP(\lambda * t)-1)).$$

λ is ^{187}Re decay constant $1.666e^{-11}a^{-1}$ (Smoliar et al., 1996), t is the P–E boundary age (55.9 Ma; Charles et al., 2011).

4.2.2 Platinum group element analysis

Powder samples were digested for PGE analysis using a modified method from Chu et al. (2014). 1g of powdered shale was loaded into carious tube with a mixed Ir-Ru-Pt-Pd tracer (spike) solution and aqua-regia (3 ml 11 N HCl and 6 ml 16 N HNO_3). The carius tubes were heated to 220°C for 72 h. After digestion the samples were centrifuged and the aqua-regia solution was dried. The samples were then purified by anion exchange column and Eichrom-LN column. Briefly this anion exchange chromatography involved loading 1 cm^3 of AG-1x8 (100–200 mesh) anion resin onto the column and cleaning with 10 ml of Milli-Q, 10 ml of 6 N HNO_3, 10 ml of 15.5 N HNO_3 and 10 ml 11 N HCl. The column was then rinsed with 2 ml of Milli-Q and preconditioned with 2 ml of 1 N HCl and 2 ml of 0.5 N HCl. The samples were dissolved with 10 ml 0.5 N HCl and then loaded onto the column. After eluting matrix elements with 10 ml of 1 N HCl and 4 ml of 0.8 N HNO_3, Ir, Pt and Ru were stripped with 20 ml of 15.5 N HNO_3. The column was rinsed in 2 ml of Milli-Q and then Pd was eluted in 40 ml of 11 N HCl. The Ir-Pt-Ru and Pd cuts were dried and dissolved in 1 ml 1 N HCl. The Ir-Pt and Pd fractions were further purified to remove Zr and Hf, respectively, using the 2-ml Eichrom-LN column. The column was cleaned with 4 ml Milli-Q, 8 ml 6 N HCl, 4 ml 2 N HF, 4 ml 6 N HCl and 4 ml 2 N HF. Then the column was rinsed with 4 ml Milli-Q and equilibrated with 4 ml 1 N HCl. The Pd cut was loaded onto the column and collected in 4ml 1 N HCl. Then the Ir-Pt-Ru fraction was loaded onto the column and eluted in 5 ml 1 N HCl. The Pd and Ir-Pt-Ru fractions were then dried and dissolved in 1 ml 0.5 N HCl. Ir-Pt-Ru and Pd solutions were measured by inductively coupled plasma mass spectrometry (ICP-MS) on a ThermoFinnigan Element 2 at Durham University. Mixed solutions of natural PGEs and solutions of Hf, Zr, Y and Mo (all at 1 ng/g concentrations) were used to quantify the degree of mass fractionation and the production rates of HfO^+, ZrO^+, YO^+, and MoO^+ (which possess oxides of equivalent mass to isotopes of Ir^+, Pt^+ and Pd^+) before and after the analysis. Two full procedural blanks

were analysed throughout the period of this study. Ir: 0.24 and 1.17 pg, Ru: 13.96 and 25.68 pg, Pt: 323.82 and 430.85 pg, Pd: 23.27 and 47.99 pg. All PGE data is listed in Table appx. 4.5 and plotted in Figure 4.4. The low reproducibility of the repeated analysis might be caused by the nugget effect. The PGEs are probably not homogenous within 1 g of sample powder.

4.2.3 Hg analysis

Mercury (Hg) concentrations were determined on a Mercury Analyzer RA 915 F coupled to a PYRO-915+ Pyrolyzer (Lumex) at the University of Lausanne (Switzerland), broadly following the method outlined in Percival et al. (2017). Mercury in the solid sample was volatilized by direct thermal evaporation, and the resultant gas analysed by atomic absorption spectrometry (see Sholupov and Ganeyev, 1995). 100 ± 2 mg of powdered sample was used per analysis, with at least two measurements per sample to check repeatability, which was typically better than ± 10%. The measurements were calibrated using the Certified Reference Material NCS DC73309 (Chinese stream sediment) as a standard, which has a concentration of 72 ± 9 ppb. Four standards were measured at the start of an analytical run, with a further standard measured after each subsequent set of ten unknown measurements to check for machine drift.

4.2.4 Total organic carbon (TOC) analysis

Powdered samples were analysed for weight percent concentration of total carbon (TC) by combustion at 950 °C in a stream of O_2. Total inorganic carbon (TIC) was analysed by acidification using 10% phosphoric acid. Sample carbon converted to CO_2 by each preparation method is quantified by coulometric titration (Huffman, 1977; Engleman et al., 1985). TOC is calculated as the difference between wt% TC and TIC. The TIC value is converted to wt% calcium carbonate by stoichiometric calculation (wt% TIC × 8.333), with the assumption that negligible quantities of inorganic carbon were present as minerals other than calcium carbonate.

4.2.5 Pyrite sulfur analysis

Pyrite sulfur was extracted from powdered samples using the chromium reduction of procedure of Canfield et al., (1986). For this study, between 0.3 and 1 g of sample powder was reacted with ~40 mL of 1 M chromous chloride solution and heated for two hours in a specialized distillation line under nitrogen atmosphere. The sulfur liberated from the sample was precipitated as zinc sulfide and later converted to silver sulfide (Ag_2S). This precipitate was dried and weighed to quantify to the pyrite sulfur contents of the sample. Reproducibility was within 5% for all repeat extractions of a subset of the samples.

4.2.6 Simulation of the comet impact

Climate model simulations use the Community Earth System Model (CESM), maintained by the National Center for Atmospheric Research (Gent et al., 2011; Hurrell et al., 2013). CESM is a state-of-the-art Earth system model that well simulates present-day climate. Here we use a fully coupled configuration of CESM with dynamic high-top atmosphere (WACCM4; Marsh et al., 2013); ocean (POP2; Danabasoglu et al., 2011); land (CLM4; Lawrence et al., 2011); and sea ice (CICE4; Hunke and Lipscomb, 2008) components. The atmosphere and land are on a 1.9° x 2.5° grid, and the ocean and sea ice are on a nominal 1° grid. The atmosphere model has 66 vertical levels that reach the thermosphere, and the ocean model has 60 vertical levels. Within WACCM4, we include the Community Aerosol and Radiation Model for Atmospheres (CARMA; Toon et al., 1988; Bardeen et al., 2008). Aerosol size distribution is able to evolve in CARMA, which is useful for accurately simulating large aerosol injections (Bardeen et al., 2017). Several WACCM4 modifications are made for model stability but have minimal impact on the model climatology (see Bardeen et al., 2017 for details). Simulations start with year 2000 climate conditions. We run the control and impact simulation for 25 years each and emit all SO_2 over the course of 1 day on January 1 of the 5^{th} year. Sulfates have a spherical particle treatment with 30 size bins and a minimum dry radius of 0.3432 nm. We emit impact SO_2 as a globally uniform gaussian distribution centered at 50

km with a half-width of one atmospheric scale height, similar to the emission recommendation of Toon et al. (2016).

4.3 Results

At Millville, Hg concentrations are ~10 ppb below the P–E boundary, but double across that horizon to 20–25 ppb, and remain elevated up section. The Hg/TOC values show a similar trend to the Hg abundance, with an increase across the P–E boundary (40 to 60 ppb / wt. %) and elevated ratios maintained up section (~60 ppb / wt. %), implying that the Hg enrichment results from an external flux of Hg from volcanism, or localized changes in organic-matter burial/preservation (Percival et al., 2018; Sanei et al., 2012). At Blake Nose, the Hg concentration is about 2–4 ppb below the P–E boundary, which increases slightly to ~7 ppb across that horizon. Two further Hg excursions of 30 and 20 ppb are also present above the P–E boundary at Blake Nose, which appear in the Hg/TOC ratios. Elevated Hg and Hg/TOC at the base of and within the main body of the PETM CIE is broadly consistent with previous investigations, although individual sedimentary records appear to show different patterns of these enrichments (Keller et al., 2018; Jones et al., 2019). Recent studies indicated that Hg enrichments could also be associated with increased sulfur/pyrite contents (Shen et al., 2019; Them et al. 2019). However, the Hg concentrations and Hg/TOC ratios exhibit no relationship with pyrite-S content at either site (Figs. 4.2 and 4.3).

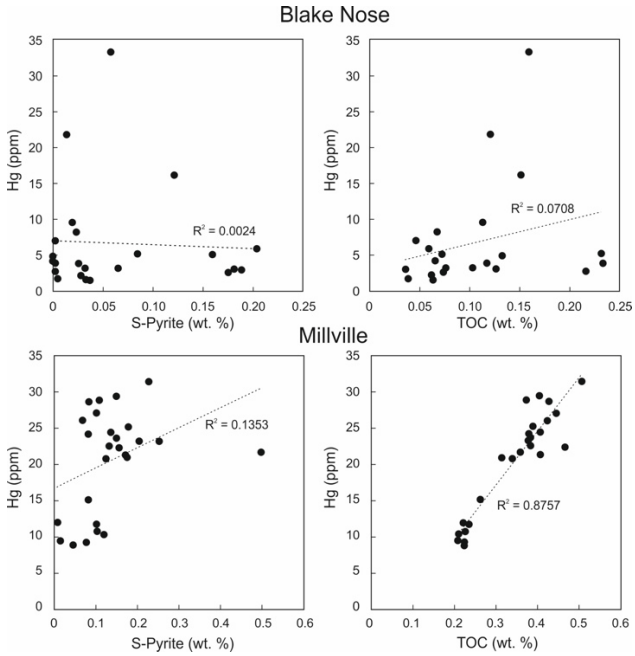

Figure 4.2 Relationships between Hg and TOC and S-pyrite. At both sites, Hg contents have no relationship with S-Pyrite contents. At Millville, TOC has a strong relation with Hg. No relationship is found between Hg and TOC at Blake Nose.

Measured Re and Os abundances are significantly enriched in the relatively organic-rich sediments of Millville (Re: 5.3–11.4 ppb, Os: 92.1–321.9 ppt) compared to the carbonate-rich pelagic sediments from Hole 1051B (Re: 0.04–0.23 ppb; Os: 26.8–146.2 ppt; appx. Table 4.1 and 4.2). The common Os isotope (^{192}Os), which represents the best estimate of Os complexed by organic matter at the time of deposition, becomes significantly enriched in the sedimentary units across the P–E boundary at Millville and Blake Nose (Fig. 4.3; appx. Table 4.1 and 4.2), with concentrations above pre-background values sustained well into the main body of PETM CIE. The ^{187}Os/^{188}Os values calculated at the time of deposition (Os_i) at the two sites range from 0.30 to 0.42, which are in good agreement with Os_i data from other P–E sections (Dickson et al., 2015; Wieczorek et al., 2013). At Millville, the Os_i values are relatively unradiogenic (0.33–0.38) below the P–E boundary, with a shift towards an even more unradiogenic composition (0.38 to 0.30) at the boundary itself. The Os_i then rapidly returns to the pre-excursion values (0.38), followed by a gradual trend towards a more radiogenic composition up-section (0.38 to 0.42; Fig. 4.3). At Blake Nose, the Os_i values are unradiogenic

(0.36–0.37) below the P–E boundary, with a nominal decrease (0.36 to 0.35) across the P–E boundary, followed by a nominal increase to 0.36 and then a decrease to 0.35 (Fig. 4.3). However, it should be noted that all variations in Os_i at Blake Nose are within analytical uncertainty.

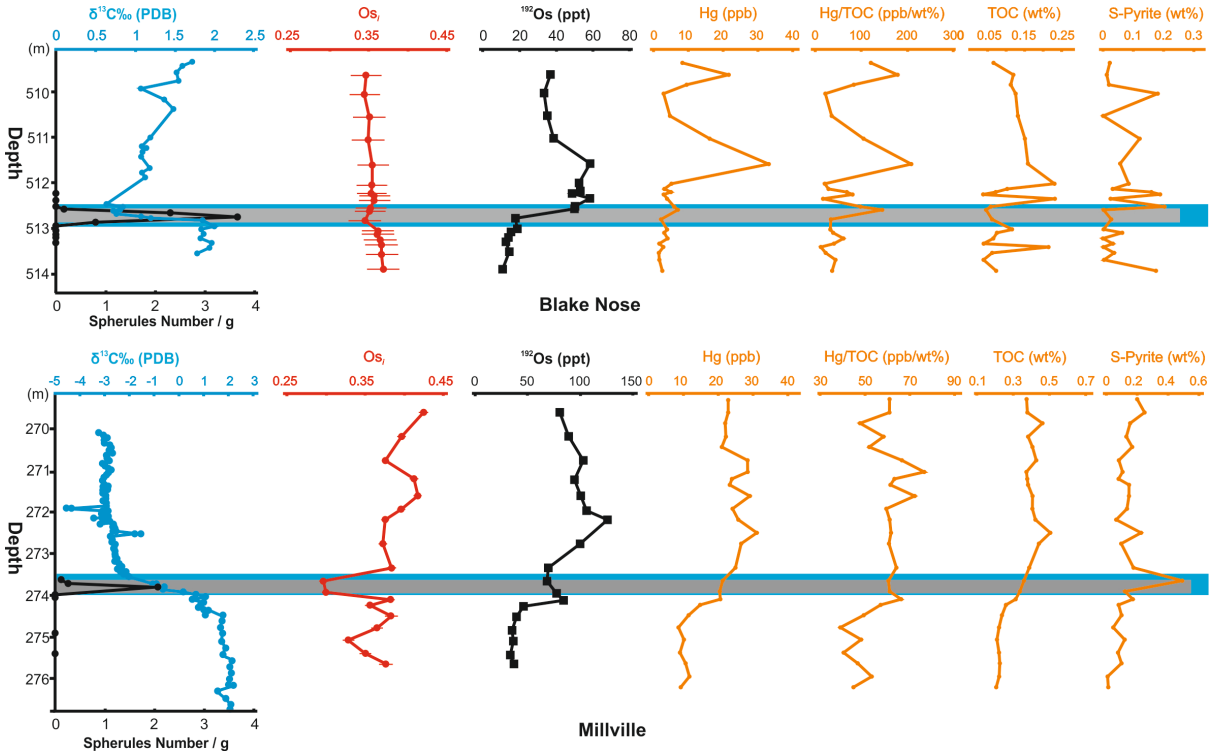

Figure 4.3 Summary of carbon isotope, Os_i, ^{192}Os, Hg, TOC (total organic carbon), pyrite sulfur, and Hg/TOC data. Carbon isotope data for Blake Nose are from Katz et al. (1999). Carbon-isotope data for Millville site is from Wright and Schaller (2013). Spherule data is from Schaller et al. (2016). Blue zone marks the base of the negative carbon isotope excursion at the P–E boundary; gray zone marks the interval where spherules are present.

No PGE anomaly is observed at the P–E boundary (Ir: 0.02–0.11 ppb, Ru: 0.10–3.04 ppb, Pd: 0.69–2.57 ppb, Pt: 0.29–2.78 ppb; Fig. 4.4; appx. Table 4.5), with the PGE values generally being lower than that reported from the Cretaceous–Paleogene boundary (Goderis et al., 2013). Further, the Ir values are lower than that of the Zumaya (0.037–0.423 ppb) and Slovenia (0.1–2.3 ppb) sections.

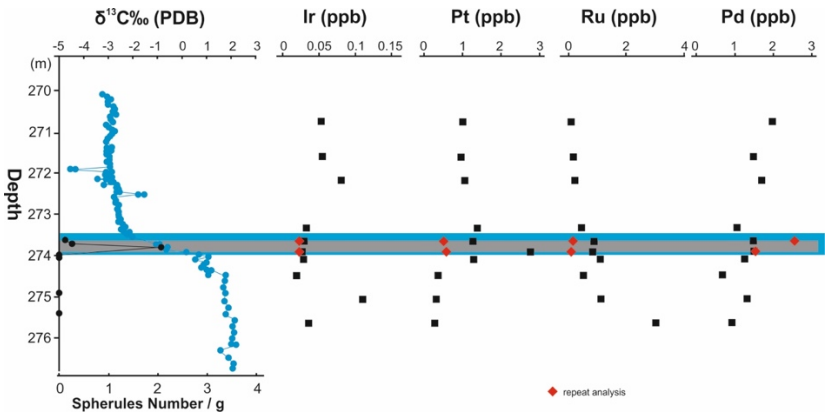

Figure 4.4 PGEs results for Millville site. Carbon isotope data is from Wright and Schaller (2013). Spherules data is from Schaller et al. (2016). Blue zone represents the interval for carbon isotope excursion at the P–E boundary; grey zone represents the interval where spherules are present.

4.4 Discussion

4.4.1 Geological events at the Paleocene-Eocene boundary

In the studied sections, Hg concentrations and Hg/TOC exhibit no relationship with pyrite sulfur content (Figs. 4.2 and 4.3; appx. Table 4.3 and 4.4), suggesting a lack of a local redox control on the Hg contents. As such, the Hg data may imply that the enrichment in Hg in the marine record results from volcanic related processes (Sanei et al., 2012; Shen et al., 2019; Jones et al., 2019). To date, there are no constraints on the potential delivery of Hg to the Earth's surface by an extraterrestrial impact body. However, if an influx of impact-derived Hg did occur and was preserved in the PETM geological record, then a single pulse of Hg enrichment would be expected. By contrast, the Hg and Hg/TOC exhibit consistently elevated (Millville) and repeated peaks (Blake Nose) at and above the P–E boundary (Fig. 4.3). The differences in the Hg and Hg/TOC profiles between Millville and Blake Nose is challenging to fully understand, nevertheless, the overall Hg enrichment and elevated Hg/TOC values are more likely a result of potentially episodic (Storey et al., 2007), large-scale volcanism, that was likely associated with the NAIP (Keller et al., 2018), or related to thermogenic emissions (Jones et al., 2019; Svensen et al., 2004), as previously hypothesized.

The short-lived unradiogenic shift in Os_i at the P–E boundary (Dickson et al., 2015; Schmitz et al., 2004; Wieczorek et al., 2013; this study) could have been caused by an increase in unradiogenic Os input, or reduced radiogenic input from decreased weathering (Peucker-Ehrenbrink and Ravizza, 2000). A reduction in weathering rates during a hyperthermal period seems unlikely as the weathering of silicate rocks is considered a negative feedback mechanism to buffer the increase of atmospheric CO_2 (Walker et al., 1981).

To date, unradiogenic Os_i shifts of a similar magnitude in PETM strata have been linked to volcanism (Dickson et al., 2015; Wieczorek et al., 2013). Although the Hg enrichment in our studied sections correlates with the Os_i unradiogenic shift at the P–E boundary, elevated Hg (Hg/TOC) values still appear above the P–E boundary, whereas Os_i returns to pre-shift values abruptly (Fig. 4.3; Dickson et al., 2015; Wieczorek et al., 2013). The discrepancy between Hg and Os_i trends may have resulted from a combination of magmatic and thermogenic Hg emissions (Jones et al., 2019). However, the coincidence of shifts to more unradiogenic Os_i values in the same stratigraphic intervals where silicate glass spherules (microtektites and microkrystites) and shocked quartz are reported (Millville and Blake Nose; Fig. 4.3), argues for an extraterrestrial source as an alternative/additional contribution to the Os influx to the ocean. However, it is not clear how much of the Os was derived from the impactor, and how much from volcanism. Furthermore, because there is no enrichment in the other PGEs (Pt, Pd, Ir, Ru) within the spherule horizon, the impact body is interpreted to be a comet that was volatile-rich and likely with lower PGEs contents compared to most other extraterrestrial bodies. This hypothesis is consistent with the vesicular volatile degassing structure of the shocked quartz (Schaller et al., 2016). Thus, a comet impact may not leave a recognizable elemental enrichment in the impact interval (Jansa, 1993). As such, the small unradiogenic Os_i shift at the PETM could reflect osmium derived from a comet impact.

4.4.2 Estimation of the comet size and component abundance

The impactor size can be estimated based on the sedimentary osmium isotope record and the oceanic Os inventory, as well as the impactor composition (Paquay et al., 2008). Estimating the size of the impactor at the PETM (Schaller et al., 2016) is difficult, given the uncertainty in the comet's chemical composition and that the Os_i excursion could be potentially driven by both volcanism and the impactor itself. No comet Os abundance data is yet available. Research suggests that the comet can be described as a dirty snowball, possible with equal mass of ice and dust (Cochran et al., 2015). Analyses of the cometary dust returned by the spacecraft mission suggest similarity between cometary dust and CI chondrite material (Wooden et al., 2017). Here we model the comet composed of equal mass of ice and dust, of which the dust is represented by CI chondrite material. Thus, the Os abundance of comet can be calculated as:

$$[Os]_{comet} = ½ \times [Os]_{CI}$$

where $[Os]_{comet}$ is the Os concentration of comet and the $[Os]_{CI}$ is the Os concentration of CI chondrite.

With the Os abundance of CI chondrite (490 ppb, Wasson and Kallemeyn, 1988), we obtain the Os abundance of the comet to be 245 ppb. The estimation here is based on the assumption that all Os from the comet is soluble and the time required for the impact-induced Os to mix with the global ocean Os is brief, on the order of several thousand years. Assuming that Os concentration of Late Palaeocene seawater is the same as that of the modern ocean, the seawater Os reservoir before an impact event can be determined by knowing the Os concentration in modern seawater (~10 pg/Kg) and the estimated mass of the seawater (~1.4×10^{21} kg). The product of these give the mass of the Os in the seawater before an impact [mass Os_{sw} (ng)] (1.4×10^{19} ng[18]).

The mass of Os derived from the impactor can be calculated as:

$$[\text{mass } Os_{comet}] = (f/1- f) \times [\text{mass } Os_{sw}]$$

where $f = (^{187}Os/^{188}Os_{postimpact} - {}^{187}Os/^{188}Os_{preimpact})/ (^{187}Os/^{188}Os_{comet} - {}^{187}Os/^{188}Os_{preimpact})$.

At Millville, Os_i shift from pre-impact value of 0.38 to post impact value of 0.3. With the seawater Os inventory as 1.4×10^{19} ng and meteoritic Os isotope composition ($^{187}Os/^{188}Os_{comet}$) as ~0.127, we can get the impact-derived Os amount 6.32×10^{18} ng.

The mass of the comet (m_{comet}) is determined by

$m_{comet} = [\text{mass } Os_{comet}]/[Os]_{comet}$

where $[Os]_{comet}$ is the comet Os concentration.

Then with the Os abundance of comet calculated before (245 ppb), we get the mass of the comet as 2.6×10^{13} kg. The diameter (D) of the comet is determined assuming a spherical comet:

$D = 2 \times (¾ \times m_{comet}/p_{comet}/\pi)^{½}$

where p_{comet} is the density of the comet.

The diameter is calculated to be ~3.3 km. Impact-derived Ir [mass Ir_{comet}] can be determined by

$[\text{mass } Ir_{comet}] = [Ir]_{comet} \times m_{comet}$

where $[Ir]_{comet}$ is the comet Ir abundance.

Ir flux can be determined with the surface area of the Earth (5.1×10^{18} cm^2) to be 1.16 ng/cm^2. In a similar way, we can estimate the comet carbon concentration $[C]_{comet}$ and sulfur concentration $[S]_{comet}$. By assuming that all the carbon will form CO_2 and all the sulfur will form SO_2, we can get the amount of CO_2 and SO_2 injected to the atmosphere by the comet.

The estimated maximum diameter of the impactor is ~3.3 km, if we assume that the impact body is responsible for the full manifestation of the observed unradiogenic Os_i (~0.08 at Millville) shift. However, it cannot be ruled out that the impactor was smaller if part of the Os_i shift resulted from other means (i.e., volcanism, see discussion above). The Os content of the comet is estimated to be 6.32×10^{18} ng, which is about 7.9% of the K-Pg impactor (8 ×

10^{19} ng Os; Paquay et al., 2008). The Ir content of this comet is estimated to be 5.93×10^{18} ng. This amount equals a global Ir flux of 1.16 ng/cm^2, which is just 2% of that across the Cretaceous–Paleogene boundary (55 ng/cm^2; Paquay et al., 2008). The low flux could explain why only small Ir spikes are found in other P–E sections (Dolenec et al., 2000; Schmitz et al., 1997), and none observed in the records studied here.

4.4.3 Climate perturbations caused by comet impact

Additional impactor-driven Earth system impacts include formation and stratospheric disbursement of sulfate aerosols, known to cause short-lived climate cooling following volcanic eruptions. We estimate that a 3.3 km diameter comet would contain ~0.76 Gt of sulfur, ~3000 times the current atmospheric sulfur mass (Kring et al., 1996). To assess the climatic impact of cometary magnitude stratospheric sulfate, we use the WACCM chemistry-climate model to simulate a baseline climate and a climate perturbed by an impactor. In our impactor simulation, we assume land-based impact and full conversion of sulfur to SO_2, i.e., we instantaneously add 1.52 Gt of SO_2 to the upper atmosphere, two orders of magnitude greater than recent annual global volcanic SO_2 emissions (0.023 Gt/yr; Carn et al., 2017). Simulations indicate global cooling of the oceans and land within 2 years of the impact (global average sea surface temperature drops ~2.2 °C; land average temperature ~3.5 °C; Fig. 4.5A, B and Fig. 4.6). Temperatures require more than a decade to recover to pre-impact values. Cooling also leads to a 7% decrease in global precipitation shortly after the impact (Fig. 4.5C and Fig. 4.6).

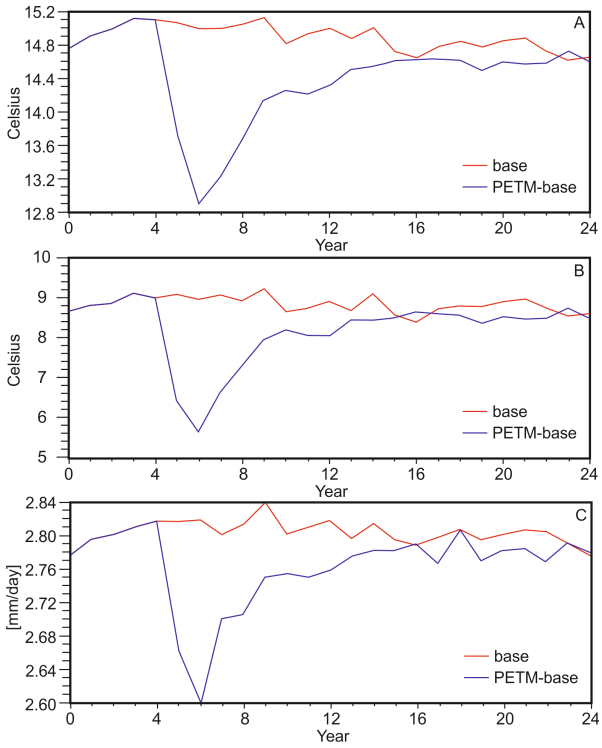

Figure 4.5 Modelled impact results of sea surface global weighted annual temperature (A), land weighted average temperature (B), and global weighted average precipitation (C). Impact was introduced in the 5th year.

Although the data suggest that both large-scale volcanism and a comet impact are associated with the P–E interval, it remains unclear to what extent they contributed to the carbon influx required to drive the PETM hyperthermal. Our model estimates the cometary carbon to be ~0.4 Gt, which is far less than the amount needed (≥3,000–10,000 Gt) to drive the PETM (Cui et al., 2011; Gutjahr et al., 2017; Zeebe et al., 2009). Thus, a comet alone cannot account for the carbon influx needed to drive the CIE and associated climate change of the PETM. As such, other sources of light carbon are needed to drive the PETM. However, it should be noted that the 0.4 Gt carbon from the comet would have been brought into the Earth system instantly and escalated pCO_2 rapidly, which may have increased the importance of that input, depending on the duration of PETM onset and the exact rate of terrestrial carbon emissions that contributed to it. It has also been speculated that an impactor may have triggered the release of other carbon reservoirs such as destabilization of gas hydrates, causing further rapid injection of greenhouse gas into the environment (Cramer and Kent, 2005).

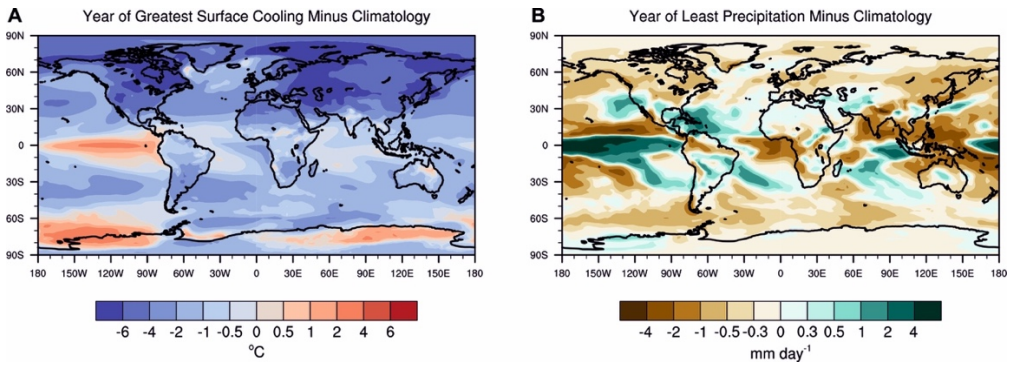

Figure 4.6 Maps showing climate modelling results.

4.5 Conclusion

Our study suggests that both a comet (~ 3.3 km diameter) impact event and volcanism are associated with climate perturbations during the Paleocene–Eocene. Carbon from the comet alone cannot account for the full manifestation of the CIE. However, the comet impact may have caused transient global cooling and reduced precipitation. Comet impact, large scale volcanism, and other sources of carbon (dissolution of methane hydrates and thermogenic volatiles, etc.) might have jointly caused the environmental disruption at the P–E boundary.

4.6 References

Bardeen, C. G., Garcia, R. R., Toon, O. B., Conley, A. J., 2017. On transient climate change at the Cretaceous−Paleogene boundary due to atmospheric soot injections. Proceedings of the National Academy of Sciences 114, E7415-E7424.

Bardeen, C. G., Toon, O. B., Jensen, E. J., Marsh, D. R., Harvey, V. L., 2008. Numerical simulations of the three-dimensional distribution of meteoric dust in the mesosphere and upper stratosphere: Journal of Geophysical Research113, D17.

Bowen, G. J., Maibauer, B. J., Kraus, M. J., Rohl, U., Westerhold, T., Steimke, A., Gingerich, P. D., Wing, S. L., Clyde, W. C., 2015. Two massive, rapid releases of carbon during the onset of the Palaeocene-Eocene thermal maximum. Nature Geosci 8, 44-47.

Canfield, D. E., Raiswell, R., Westrich, J. T., Reaves, C. M., Berner, R. A., 1986. The use of chromium reduction in the analysis of reduced inorganic sulfur in sediments and shales. Chemical Geology 54, 149-155.

Carn, S. A., Fioletov, V. E., McLinden, C. A., Li, C., and Krotkov, N. A., 2017. A decade of global volcanic SO_2 emissions measured from space. Scientific Reports 7, 44095.

Charles, A. J., Condon, D. J., Harding, I. C., Pälike, H., Marshall, J. E. A., Cui, Y., Kump, L., and Croudace, I. W., 2011. Constraints on the numerical age of the Paleocene-Eocene boundary. Geochemistry, Geophysics, Geosystems 12, n/a-n/a.

Chu, Z., Yan, Y., Chen, Z., Guo, J., Yang, Y., Li, C., Zhang, Y., 2015. A Comprehensive Method for Precise Determination of Re, Os, Ir, Ru, Pt, Pd Concentrations and Os Isotopic Compositions in Geological Samples. Geostandards and Geoanalytical Research 39, 151-169.

Cochran, A. L., Levasseur-Regourd, A.-C., Cordiner, M., Hadamcik, E., Lasue, J., Gicquel, A., Schleicher, D. G., Charnley, S. B., Mumma, M. J., Paganini, L., Bockelée-Morvan, D., Biver, N., Kuan, Y.-J., 2015. The Composition of Comets. Space Science Reviews 197, 9-46.

Cramer, B. S., Kent, D. V., 2005. Bolide summer. The Paleocene/Eocene thermal maximum as a response to an extraterrestrial trigger. Palaeogeography, Palaeoclimatology, Palaeoecology 224, 144-166.

Creaser, R. A., Papanastassiou, D. A., Wasserburg, G. J., 1991. Negative thermal ion mass spectrometry of osmium, rhenium and iridium. Geochimica et Cosmochimica Acta 55, 397-401.

Cui, Y., Kump, L. R., Ridgwell, A. J., Charles, A. J., Junium, C. K., Diefendorf, A. F., Freeman, K. H., Urban, N. M., Harding, I. C., 2011. Slow release of fossil carbon during the Palaeocene–Eocene Thermal Maximum. Nature Geoscience 4, 481.

Danabasoglu, G., Bates, S. C., Briegleb, B. P., Jayne, S. R., Jochum, M., Large, W. G., Peacock, S., Yeager, S. G., 2011. The CCSM4 Ocean Component. Journal of Climate 25, 1361-1389.

DeConto, R. M., Galeotti, S., Pagani, M., Tracy, D., Schaefer, K., Zhang, T., Pollard, D., Beerling, D. J., 2012. Past extreme warming events linked to massive carbon release from thawing permafrost. Nature 484, 87.

Dickens, G. R., O'Neil, J. R., Rea, D. K., Owen, R. M., 1995. Dissociation of oceanic methane hydrate as a cause of the carbon isotope excursion at the end of the Paleocene. Paleoceanography 10, 965-971.

Dickson, A. J., Cohen, A. S., Coe, A. L., Davies, M., Shcherbinina, E. A., Gavrilov, Y. O., 2015. Evidence for weathering and volcanism during the PETM from Arctic Ocean and Peri-Tethys osmium isotope records. Palaeogeography, Palaeoclimatology, Palaeoecology 438, 300-307.

Dolenec, T., Pavšič, J., Lojen, S., 2000. Ir anomalies and other elemental markers near the Palaeocene–Eocene boundary in a flysch sequence from the Western Tethys (Slovenia). Terra Nova 12, 199-204.

Engleman, E. E., Jackson, L. L., Norton, D. R., 1985. Determination of carbonate carbon in geological materials by coulometric titration. Chemical Geology 53, 125-128.

Gent, P. R., Danabasoglu, G., Donner, L. J., Holland, M. M., Hunke, E. C., Jayne, S. R., Lawrence, D. M., Neale, R. B., Rasch, P. J., Vertenstein, M., Worley, P. H., Yang, Z.-L., Zhang, M., 2011. The Community Climate System Model Version 4. Journal of Climate 24, 4973-4991.

Gingerich, P.D., 2003. Mammalian responses to climate change at the Paleocene-Eocene boundary: Polecat Bench record in the northern Bighorn Basin, Wyoming, *in* Wing, S.L., Gingerich, P.D., Schmitz, B., and Thomas, E., eds., Causes and Consequences of

Globally Warm Climates in the Early Paleogene: Boulder, Colorado. Geological Society of America Special Paper 369, 463–478.

Goderis, S., Tagle, R., Belza, J., Smit, J., Montanari, A., Vanhaecke, F., Erzinger, J., Claeys, P., 2013. Reevaluation of siderophile element abundances and ratios across the Cretaceous–Paleogene (K–Pg) boundary: Implications for the nature of the projectile. Geochimica et Cosmochimica Acta 120, 417-446.

Gutjahr, M., Ridgwell, A., Sexton, P. F., Anagnostou, E., Pearson, P. N., Pälike, H., Norris, R. D., Thomas, E., Foster, G. L., 2017. Very large release of mostly volcanic carbon during the Palaeocene–Eocene Thermal Maximum. Nature 548, 573.

Higgins, J. A., Schrag, D. P., 2006. Beyond methane: Towards a theory for the Paleocene–Eocene Thermal Maximum. Earth and Planetary Science Letters 245, 523-537.

Huffman, E. W. D., 1977. Performance of a new automatic carbon dioxide coulometer. Microchemical Journal 22, 567-573.

Hunke, E. C., Lipscomb, W. H., 2008. CICE: The Los Alamos sea ice model, documentation and software user's manual.

Hurrell, J. W., Holland, M. M., Gent, P. R., Ghan, S., Kay, J. E., Kushner, P. J., Lamarque, J. F., Large, W. G., Lawrence, D., Lindsay, K., Lipscomb, W. H., Long, M. C., Mahowald, N., Marsh, D. R., Neale, R. B., Rasch, P., Vavrus, S., Vertenstein, M., Bader, D., Collins, W. D., Hack, J. J., Kiehl, J., Marshall, S., 2013. The Community Earth System Model: A Framework for Collaborative Research. Bulletin of the American Meteorological Society 94, 1339-1360.

Jansa, L. F., 1993. Cometary impacts into ocean: their recognition and the threshold constraint for biological extinctions. Palaeogeography, Palaeoclimatology, Palaeoecology 104, 271-286.

Jones, M. T., Percival, L. M. E., Stokke, E. W., Frieling, J., Mather, T. A., Riber, L., Schubert, B. A., Schultz, B., Tegner, C., Planke, S., Svensen, H. H., 2019. Mercury anomalies across the Palaeocene–Eocene Thermal Maximum. Clim. Past 15, 217-236.

Katz, M. E., Pak, D. K., Dickens, G. R., Miller, K. G., 1999. The Source and Fate of Massive Carbon Input During the Latest Paleocene Thermal Maximum. Science 286, 1531-1533.

Keller, G., Mateo, P., Punekar, J., Khozyem, H., Gertsch, B., Spangenberg, J., Bitchong, A. M., Adatte, T., 2018. Environmental changes during the Cretaceous-Paleogene mass extinction and Paleocene-Eocene Thermal Maximum: Implications for the Anthropocene. Gondwana Research 56, 69-89.

Kring, D. A., Melosh, H. J., Hunten, D. M., 1996. Impact-induced perturbations of atmospheric sulfur. Earth and Planetary Science Letters 140, 201-212.

Lawrence, D. M., Oleson, K. W., Flanner, M. G., Fletcher, C. G., Lawrence, P. J., Levis, S., Swenson, S. C., Bonan, G. B., 2011. The CCSM4 Land Simulation, 1850–2005: Assessment of Surface Climate and New Capabilities. Journal of Climate 25, 2240-2260.

Ludwig, K. R., 1980, Calculation of uncertainties of U-Pb isotope data. Earth and Planetary Science Letters 46, 212-220.

Marsh, D. R., Mills, M. J., Kinnison, D. E., Lamarque, J.-F., Calvo, N., Polvani, L. M., 2013. Climate Change from 1850 to 2005 Simulated in CESM1(WACCM). Journal of Climate 26, 7372-7391.

Paquay, F. S., Ravizza, G. E., Dalai, T. K., Peucker-Ehrenbrink, B., 2008. Determining Chondritic Impactor Size from the Marine Osmium Isotope Record. Science 320, 214-218.

Pidwirny, M., 2006. "Introduction to the Oceans". Fundamentals of Physical Geography, 2nd Edition.

Percival, L. M. E., Ruhl, M., Hesselbo, S. P., Jenkyns, H. C., Mather, T. A., Whiteside, J. H., 2017. Mercury evidence for pulsed volcanism during the end-Triassic mass extinction. Proceedings of the National Academy of Sciences 114, 7929-7934.

Percival, L. M. E., Jenkyns, H. C., Mather, T. A., Dickson, A. J., Batenburg, S. J., Ruhl, M., Hesselbo, S. P., Barclay, R., Jarvis, I., Robinson, S. A., Woelders, L., 2018. Does large igneous province volcanism always perturb the mercury cycle? Comparing the records of Oceanic Anoxic Event 2 and the end-Cretaceous to other Mesozoic events. American Journal of Science 318, 799-860.

Peucker-Ehrenbrink, B., Ravizza, G., 2000. The marine osmium isotope record. Terra Nova 12, 205-219.

Ravizza, G. E., 2001. Platinum Group Elements and their Isotopes in the Ocean, in Steele, J. H., ed., Encyclopedia of Ocean Sciences (Second Edition): Oxford, Academic Press, 494-503.

Sanei, H., Grasby, S. E., Beauchamp, B., 2012. Latest Permian mercury anomalies. Geology 40, 63-66.

Saunders, A. D., 2016. Two LIPs and two Earth-system crises: the impact of the North Atlantic Igneous Province and the Siberian Traps on the Earth-surface carbon cycle. Geological Magazine 153, 201-222.

Schaller, M. F., Fung, M. K., Wright, J. D., Katz, M. E., Kent, D. V., 2016. Impact ejecta at the Paleocene-Eocene boundary. Science 354, 225-229.

Schmitz, B., Asaro, F., Molina, E., Monechi, S., von Salis, K., Speijer, R. P., 1997. High-resolution iridium, $\delta^{13}C$, $\delta^{18}O$, foraminifera and nannofossil profiles across the latest Paleocene benthic extinction event at Zumaya, Spain. Palaeogeography, Palaeoclimatology, Palaeoecology 133, 49-68.

Schmitz, B., Peucker-Ehrenbrink, B., Heilmann-Clausen, C., Åberg, G., Asaro, F., Lee, C.-T. A., 2004. Basaltic explosive volcanism, but no comet impact, at the Paleocene–Eocene boundary: high-resolution chemical and isotopic records from Egypt, Spain and Denmark. Earth and Planetary Science Letters 225, 1-17.

Schmitz, B., Pujalte, V., 2003. Sea-level, humidity, and land-erosion records across the initial Eocene thermal maximum from a continental-marine transect in northern Spain. Geology 31, 689-692.

Selby, D., Creaser, R. A., 2003. Re–Os geochronology of organic rich sediments: an evaluation of organic matter analysis methods. Chemical Geology 200, 225-240.

Selby, D., Creaser, R. A., Fowler, M. G., 2007. Re–Os elemental and isotopic systematics in crude oils. Geochimica et Cosmochimica Acta 71, 378-386.

Shen, J., Algeo, T. J., Chen, J., Planavsky, N. J., Feng, Q., Yu, J., Liu, J., 2019. Mercury in marine Ordovician/Silurian boundary sections of South China is sulfide-hosted and non-volcanic in origin. Earth and Planetary Science Letters 511, 130-140.

Sholupov, S. E., Ganeyev, A. A., 1995. Zeeman atomic absorption spectrometry using high frequency modulated light polarization. Spectrochimica Acta Part B: Atomic Spectroscopy 50, 1227-1236.

Smoliar, M. I., Walker, R. J., Morgan, J. W., 1996. Re-Os ages of group IIA, IIIA, IVA, and IVB iron meteorites. Science 271, 1099.

Storey, M., Duncan, R. A., Tegner, C., 2007. Timing and duration of volcanism in the North Atlantic Igneous Province: Implications for geodynamics and links to the Iceland hotspot. Chemical Geology 241, 264-281.

Svensen, H., Planke, S., Malthe-Sørenssen, A., Jamtveit, B., Myklebust, R., Rasmussen Eidem, T., Rey, S. S., 2004. Release of methane from a volcanic basin as a mechanism for initial Eocene global warming. Nature 429, 542.

Them, T. R., Jagoe, C. H., Caruthers, A. H., Gill, B. C., Grasby, S. E., Gröcke, D. R., Yin, R., Owens, J. D., 2019. Terrestrial sources as the primary delivery mechanism of mercury to the oceans across the Toarcian Oceanic Anoxic Event (Early Jurassic). Earth and Planetary Science Letters 507, 62-72.

Toon, O. B., Bardeen, C., Garcia, R., 2016. Designing global climate and atmospheric chemistry simulations for 1 and 10 km diameter asteroid impacts using the properties of ejecta from the K-Pg impact. Atmos. Chem. Phys. 16, 13185-13212.

Toon, O. B., Turco, R. P., Westphal, D., Malone, R., Liu, M., 1988. A Multidimensional Model for Aerosols: Description of Computational Analogs. Journal of the Atmospheric Sciences 45, 2123-2144.

Walker, J. C. G., Hays, P. B., Kasting, J. F., 1981. A negative feedback mechanism for the long-term stabilization of Earth's surface temperature. Journal of Geophysical Research: Oceans 86, 9776-9782.

Wasson, J. T. Kallemeyn, G. W., 1988. Compositions of chondrites. Philosophical Transactions of the Royal Society of London. Series A, Mathematical and Physical Sciences 325, 535-544.

Wieczorek, R., Fantle, M. S., Kump, L. R., Ravizza, G., 2013. Geochemical evidence for volcanic activity prior to and enhanced terrestrial weathering during the Paleocene Eocene Thermal Maximum. Geochimica et Cosmochimica Acta 119, 391-410.

Wing, S. L., Harrington, G. J., Smith, F. A., Bloch, J. I., Boyer, D. M., Freeman, K. H., 2005. Transient Floral Change and Rapid Global Warming at the Paleocene-Eocene Boundary. Science 310, 993-996.

Wooden, D. H., Ishii, H. A., Zolensky, M. E., 2017. Cometary dust: the diversity of primitive refractory grains. Philosophical transactions. Series A, Mathematical, physical, and engineering sciences 375, 20160260.

Wright, J. D., Schaller, M. F., 2013. Evidence for a rapid release of carbon at the Paleocene-Eocene thermal maximum. Proceedings of the National Academy of Sciences 110, 15908-15913.

Zachos, J., Pagani, M., Sloan, L., Thomas, E., Billups, K., 2001. Trends, Rhythms, and Aberrations in Global Climate 65 Ma to Present. Science 292, 686-693.

Zeebe, R. E., Zachos, J. C., Dickens, G. R., 2009. Carbon dioxide forcing alone insufficient to explain Palaeocene–Eocene Thermal Maximum warming. Nature Geoscience 2 576.

Chapter 5

Conclusions and future research

This thesis addresses the application of Re–Os isotope system, coupled with other geochemical proxies on three key intervals in Earth's history: the Wuchiapingian–Changhsingian boundary, the Frasnian–Famennian boundary and the Paleocene–Eocene boundary. For the reason that this thesis was written as a series of papers, each chapter has its own specific discussion, implications and conclusion section. This chapter briefly brings together the key conclusions and implications of each chapter and suggests possible directions for future research.

5.1 Os isotope stratigraphy of the Wuchiapingian–Changhsingian boundary

New Os isotope stratigraphy of four Wuchiapingian–Changhsingian boundary sections in South China (Lianyuan, Meishan and Shangsi) and the Canadian Arctic (Buchanan Lake) shows two unradiogenic Os isotope excursion. The first unradiogenic Os isotope excursion (Late Wuchiapingian) is only detected in Lianyuan and Meishan sections while the second unradiogenic Os isotope shift (Early Changhsingian) is measured in all four sections and is considered a global signature. Given the lack of evidence of any extraterrestrial impact and/or glaciation events, the osmium isotope excursions are interpreted to be caused by unradiogenic Os input from volcanism that may be linked with the Emeishan LIP (Shen et al., 2019). As there is no known mass extinction event associated with the WCB volcanism, it was likely associated with a small-scale eruption. As such, any climate perturbation caused by the volcanism may have been rapidly overturned back to pre-eruption conditions.

The new Os isotope data, indicating a volcanic event, suggest that the injection of isotopically light carbon from volcanic degassing may have been an additional mechanism that caused the Wuchiapingian–Changhsingian boundary carbon isotope excursions. Furthermore,

this study also demonstrated that osmium isotopes can be used to evaluate the extent of ancient volcanism, which is commonly linked with climate perturbation and biotic crisis events.

Further research using other geochemical proxies (for example: Hg concentration and its isotopes, Mo and U isotopes) on more global sections would provide a more complete understanding of the volcanism, and the paleoclimate and palaeoceanography changes around the Wuchiapingian–Changhsing boundary.

5.2 Wildfire, O_2 level and mass extinction at the Frasnian–Famennian boundary

Previously, the Late Devonian has been suggested to have a low atmosphere oxygen level due to the lack of an inertinite record at the Frasnian–Famennian boundary (Berner, 2006; Rimmer et al., 2015; Scott and Glasspool, 2006). Our finding of inertinite at this time interval suggests a wildfire event and thus demonstrates a significantly higher atmospheric oxygen level than previously proposed (~25 %).

The high-resolution osmium isotope data does not support the temporal association of volcanism or extraterrestrial impact during the Frasnian–Famennian boundary interval. In addition, the high level of oxygen supports the hypothesis that enhanced orogeny and sea level fall may have led to enhanced weathering of the continent coupled with a decrease in the pCO_2 level. This perturbation may have led to climate cooling that ultimately contributed to the Frasnian–Famennian mass extinction (Huang et al., 2018).

This study also provides supporting evidence of previous studies that suggests that the redox/euxinic environment may not control Re and Os fractionation in organic-rich sediments (Selby et al., 2009). Rather, a variable deposition environment with heterogenous organic matter composition may be the fundamental control behind fractionation of Re and Os (Harris et al., 2013).

Future research: organic petrology investigations across the Frasnian–Famennian boundary interval globally may provide additional records of charcoal to support the wildfire

event and further constrain the extent and size of wildfire(s) during the Late Devonian. Other combustion proxy (e.g., coronene, benzo[ghi]perylene and benzo[e]pyrene) studies would also help to investigate the wildfire event hypothesis across the Frasnian–Famennian interval. Lastly, further investigation and understanding of the mechanisms that control Re and Os fractionation will help with the sample selection and successful dating of organic rich sedimentary rocks with the Re–Os geochronology. A thorough characterization of organic matter type, redox environments, terrestrial inputs and the mineral composition would aid in fully understanding of the mechanisms that control Re and Os fractionation.

5.3 Climate perturbations at the Paleocene–Eocene interval

Many mechanisms have been proposed to account for the Paleocene–Eocene thermal maximum (see 1.3 for details). Mercury enrichments are found at and above the P–E boundary and in both Millville and Blake Nose drill cores and the lack of relationship between Hg and pyrite sulfur suggest that the Hg is not controlled by the local redox environment. The enrichment of Hg suggests volcanism is a possible source of isotopically light carbon that drove the hyperthermal event. Osmium isotope excursions are only found at the P–E interval that correlate with the Hg enrichment. In contrast, no Os isotope excursion is associated with the Hg enrichments above the P–E boundary. Given the correlation between Os isotope excursion and impact induced shocked quartz and glass spherules (microtektites and microkrystites) the P–E interval, the osmium isotope excursion is better explained to be of impact origin rather than volcanism. As such, the Hg enrichment may result from thermal alteration of organic-rich layers due to magmatic intrusions of the North Atlantic Igneous Province, rather than direct input from volcanic outgassing (Svensen et al., 2004).

The lack of platinum group element enrichment suggests that the impact body may be a comet, which would have resulted in limited meteoritic dust. Based on the osmium isotope record, the comet is estimated to be ~3.3 km diameter (Paquay et al., 2008). The cometary

carbon is estimated to be ~0.4 Gt and thus cannot account for the hyperthermal event. Climate simulation (Community Earth System Model) suggests that the cometary sulfur may cause transient climate cooling and reduced precipitation. As such, the climate perturbations during the Paleocene–Eocene boundary may have been caused by a culmination of large scale volcanism, comet impact and other sources of carbon (e.g., dissolution of methane hydrates and thermogenic volatiles, etc.).

Currently the impact evidence only comes from shock quartz and spherules identified from three North America sections (Schaller et al., 2016), future research finding more impact evidence from global sections would further support the impact scenario and also aid to locate the impact crater. In theory, the hyperthermal event would result in a radiogenic shift in osmium isotope record by enhanced continental weathering (Peucker-Ehrenbrink and Ravizza, 2000; Walker et al., 1981). However, this is not detected in the record of the Blake Nose core. Further application of osmium isotope on more complete sections with high-resolution chronology control would better understand the dynamics during the P–E hyperthermal event. Multiple redox proxies (redox sensitive metals, Mo and U isotope, etc.) characterization could help the understanding of the timing relationships between volcanism, an impact event and redox change.

5.4 References

Berner, R.A., 2006. GEOCARBSULF: A combined model for Phanerozoic atmospheric O_2 and CO_2. Geochimica et Cosmochimica Acta 70, 5653-5664.

Harris, N.B., Mnich, C.A., Selby, D., Korn, D., 2013. Minor and trace element and Re–Os chemistry of the Upper Devonian Woodford Shale, Permian Basin, west Texas: Insights into metal abundance and basin processes. Chemical Geology 356, 76-93.

Huang, C., Joachimski, M.M., Gong, Y., 2018. Did climate changes trigger the Late Devonian Kellwasser Crisis? Evidence from a high-resolution conodont $\delta^{18}O_{PO4}$ record from South China. Earth and Planetary Science Letters 495, 174-184.

Paquay, F.S., Ravizza, G.E., Dalai, T.K., Peucker-Ehrenbrink, B., 2008. Determining Chondritic Impactor Size from the Marine Osmium Isotope Record. Science 320, 214-218.

Peucker-Ehrenbrink, B., Ravizza, G., 2000. The marine osmium isotope record. Terra Nova 12, 205-219.

Rimmer, S.M., Hawkins, S.J., Scott, A.C., Cressler, W.L., 2015. The rise of fire: Fossil charcoal in late Devonian marine shales as an indicator of expanding terrestrial ecosystems, fire, and atmospheric change. American Journal of Science 315, 713-733.

Schaller, M.F., Fung, M.K., Wright, J.D., Katz, M.E., Kent, D.V., 2016. Impact ejecta at the Paleocene-Eocene boundary. Science 354, 225-229.

Scott, A.C., Glasspool, I.J., 2006. The diversification of Paleozoic fire systems and fluctuations in atmospheric oxygen concentration. Proceedings of the National Academy of Sciences 103, 10861-10865.

Selby, D., Mutterlose, J., Condon, D. J., 2009. U–Pb and Re–Os geochronology of the Aptian/Albian and Cenomanian/Turonian stage boundaries: Implications for timescale calibration, osmium isotope seawater composition and Re–Os systematics in organic-rich sediments. Chemical Geology 265, 394-409.

Shen, S., Zhang, H., Zhang, Y., Yuan, D., Chen, B., He, W., Mu, L., Lin, W., Wang, W., Chen, J., Wu, Q., Cao, C., Wang, Y., Wang, X.J.S.C.E.S., 2019. Permian integrative stratigraphy and timescale of China. Science China-Earth Sciences 62, 154-188.

Svensen, H., Planke, S., Malthe-Sørenssen, A., Jamtveit, B., Myklebust, R., Rasmussen Eidem, T., Rey, S.S., 2004. Release of methane from a volcanic basin as a mechanism for initial Eocene global warming. Nature 429, 542.

Walker, J.C.G., Hays, P.B., Kasting, J.F., 1981. A negative feedback mechanism for the long-term stabilization of Earth's surface temperature. Journal of Geophysical Research: Oceans 86, 9776-9782.

Appendix

Table 2.1 Re–Os and $\delta^{13}C_{org}$ data for Lianyuan section.

Depth (m)	Re (ppb)	±	Os (ppt)	±	^{192}Os (ppt)	±	^{187}Re/^{188}Os	±	^{187}Os/^{188}Os	±	rho	Os_i	±	$\delta^{13}C_{org}$(VPDB)
12.7	11.72	0.03	70.9	0.7	15.7	0.1	1489.8	13.4	6.8	0.1	0.875	0.48	0.003	-24.73
11.2	8.10	0.02	46.4	0.5	9.8	0.1	1639.8	22.0	7.4	0.1	0.923	0.46	0.004	-24.46
10.8	3.23	0.01	20.9	0.3	4.8	0.1	1325.8	35.2	6.1	0.2	0.942	0.49	0.009	-24.91
10.2	8.46	0.02	47.2	0.5	10.0	0.1	1679.9	21.9	7.4	0.1	0.930	0.24	0.002	-25.88
9.4	30.63	0.07	155.9	1.2	30.2	0.2	2020.2	11.8	8.8	0.1	0.756	0.25	0.001	-24.71
9.3	3.31	0.01	19.0	0.4	4.1	0.1	1617.2	50.2	7.3	0.2	0.957	0.40	0.009	-24.79
9	27.22	0.07	148.2	1.7	31.1	0.4	1741.7	24.2	7.5	0.1	0.936	0.16	0.002	-22.86
8.4	29.74	0.08	202.1	1.8	49.7	0.5	1189.7	11.2	5.3	0.1	0.867	0.28	0.002	-23.95
7.6	6.71	0.02	120.5	0.7	41.0	0.3	325.8	2.1	1.8	0.0	0.684	0.38	0.002	-23.1
7	6.99	0.02	93.7	0.6	29.6	0.2	470.0	3.4	2.5	0.0	0.725	0.49	0.003	-23.48
6	6.76	0.02	132.2	0.8	45.5	0.3	295.6	1.9	1.7	0.0	0.681	0.41	0.002	-23.51
5.6	6.56	0.02	128.7	0.7	44.3	0.3	295.0	1.9	1.7	0.0	0.682	0.41	0.002	-23.77
5.1	5.78	0.02	152.3	0.8	54.9	0.3	209.5	1.3	1.2	0.0	0.649	0.35	0.002	-23.47
5	3.34	0.01	106.8	0.7	39.4	0.3	168.4	1.5	1.0	0.0	0.685	0.32	0.002	-23.76
4.8	10.18	0.03	209.1	1.0	73.3	0.3	276.4	1.4	1.5	0.0	0.638	0.32	0.001	-24.01
4.6	16.49	0.04	237.0	1.2	78.4	0.3	418.2	2.0	2.0	0.0	0.627	0.25	0.001	-23.05
4.4	24.52	0.06	296.1	1.7	94.1	0.4	518.3	2.7	2.4	0.0	0.670	0.22	0.001	-23.28
4.2	10.54	0.03	248.8	1.5	90.2	0.7	232.5	1.8	1.2	0.0	0.693	0.20	0.001	-24.87
4	1.96	0.01	58.2	0.6	20.4	0.3	191.4	3.0	1.5	0.0	0.711	0.68	0.009	-23.72
3.8	0.55	0.01	25.5	0.6	9.0	0.4	121.7	5.3	1.5	0.1	0.702	0.95	0.035	-23.68
3.2	0.34	0.01	29.4	0.6	10.5	0.4	63.8	2.9	1.3	0.1	0.662	1.06	0.039	-23.42
2.4	0.15	0.01	18.4	0.7	6.5	0.5	46.9	4.3	1.4	0.2	0.648	1.17	0.086	-22.56
1.65	0.23	0.01	28.8	0.6	10.3	0.4	43.7	2.2	1.4	0.1	0.609	1.18	0.045	-22.15
1	0.23	0.01	29.9	0.6	10.6	0.4	42.7	2.1	1.4	0.1	0.609	1.21	0.046	-22.31

All uncertainties are given at 2σ level.
Os_i values are determined using the Wuchiapingian–Changhsingian boundary age of 254.14 Ma (Shen et al., 2019b).
Rho is the associated error correlation.

Table 2.2 Re–Os data for Meishan section.

Depth (m)	Re (ppb)	±	Os (ppt)	±	^{192}Os (ppt)	±	^{187}Re/^{188}Os	±	^{187}Os/^{188}Os	±	rho	Os_i	±
-37.29	115.73	0.29	657.8	4.5	136.3	0.5	1689.7	7.3	7.7	0.04	0.584	0.63	0.07
-39.22	94.15	0.23	737.1	4.6	188.6	0.7	993.0	4.3	4.8	0.03	0.571	0.62	0.04
-41.41	131.02	0.32	877.5	5.7	206.7	0.7	1261.3	5.5	5.9	0.03	0.580	0.55	0.05
-42.39	7.69	0.02	51.5	0.4	12.3	0.1	1240.0	7.5	5.7	0.04	0.697	0.41	0.07
-43.10	18.04	0.05	143.1	0.9	36.2	0.1	990.4	4.6	5.0	0.03	0.596	0.76	0.05
-44.94	5.96	0.02	48.4	0.4	12.6	0.1	938.8	7.0	4.6	0.04	0.632	0.61	0.07
-46.19	2.37	0.01	22.2	0.2	6.3	0.1	747.7	7.0	3.6	0.04	0.769	0.44	0.07
-46.41	44.92	0.14	325.2	2.1	80.2	0.3	1114.6	5.4	5.3	0.03	0.554	0.57	0.05
-46.95	4.56	0.01	26.8	0.3	6.0	0.1	1510.9	14.2	6.6	0.07	0.791	0.17	0.13
-47.24	44.75	0.11	346.7	2.2	88.3	0.3	1008.2	4.5	4.9	0.03	0.598	0.61	0.04
-47.97	3.68	0.01	24.9	0.2	5.9	0.1	1239.6	11.9	5.8	0.07	0.787	0.55	0.12
-48.80	67.94	0.17	474.6	3.0	114.9	0.4	1176.4	5.0	5.5	0.03	0.569	0.55	0.05
-49.90	124.66	0.31	804.7	5.2	185.8	0.7	1334.6	5.7	6.2	0.03	0.579	0.51	0.05
-50.65	95.57	0.24	710.8	4.5	178.8	0.6	1063.5	4.6	5.0	0.03	0.576	0.53	0.05
-52.39	4.67	0.01	66.8	0.5	21.1	0.1	441.5	3.1	2.5	0.02	0.661	0.62	0.04
-54.87	1.35	0.00	40.9	0.5	14.5	0.3	185.1	3.8	1.4	0.04	0.704	0.63	0.06
-65.81	1.97	0.01	36.1	0.4	12.0	0.2	327.0	4.7	2.0	0.04	0.705	0.61	0.06

All uncertainties are given at 2σ level.
Os_i values are determined using the Wuchiapingian–Changhsingian boundary age of 254.14 Ma (Shen et al., 2019b).
Rho is the associated error correlation.

Table 2.3 Re–Os data for Shangsi section.

Depth (m)	Re (ppb)	±	Os (ppt)	±	^{192}Os (ppt)	±	^{187}Re/^{188}Os	±	^{187}Os/^{188}Os	±	rho	Os_i	±
94.25	0.78	0.00	10.9	0.1	3.5	0.1	442.2	6.6	2.32	0.04	0.818	0.44	0.05
92.1	21.15	0.06	190.1	1.2	52.2	0.2	805.5	3.7	3.98	0.02	0.561	0.56	0.04
89.4	20.00	0.05	153.0	1.0	39.1	0.2	1017.7	4.8	4.84	0.03	0.605	0.53	0.03
87.9	18.74	0.05	153.5	1.0	40.2	0.2	928.2	4.4	4.56	0.03	0.611	0.62	0.03
86.65	120.26	0.31	1051.2	6.1	296.8	1.0	805.9	3.5	3.67	0.02	0.540	0.25	0.03
85.8	79.12	0.20	459.2	3.2	96.3	0.3	1635.1	7.2	7.56	0.04	0.585	0.63	0.05
85.5	23.61	0.06	213.3	1.3	58.2	0.2	807.6	3.5	4.07	0.02	0.579	0.64	0.04
84.05	16.77	0.04	130.8	0.9	33.1	0.1	1009.1	4.8	4.98	0.03	0.590	0.70	0.05
83.1	153.59	0.38	933.0	6.2	207.5	0.7	1472.6	6.3	6.69	0.03	0.580	0.45	0.06
82.6	124.07	0.30	1060.9	6.3	285.3	1.0	865.2	3.8	4.23	0.02	0.580	0.56	0.04
80.9	841.76	2.06	3460.3	26.5	483.6	1.7	3462.5	14.5	15.11	0.07	0.570	0.42	0.10
79.6	122.20	0.30	699.6	4.9	147.2	0.5	1651.4	7.2	7.50	0.04	0.583	0.50	0.05
78.3	146.66	0.36	603.3	4.8	84.1	0.3	3471.3	15.7	15.18	0.08	0.616	0.46	0.10
76.7	678.04	1.68	2722.8	21.7	366.3	1.3	3682.3	15.8	15.99	0.08	0.564	0.37	0.11
75.4	1017.76	2.48	3932.2	31.2	476.3	1.6	4250.8	17.8	18.59	0.09	0.567	0.56	0.12

All uncertainties are given at 2σ level.
Os_i values are determined using the Wuchiapingian–Changhsingian boundary age of 254.14 Ma (Shen et al., 2019b).
Rho is the associated error correlation.

Table 2.4 Re–Os data for Buchanan Lake section.

Depth (m)	Re (ppb)	±	Os (ppt)	±	^{192}Os (ppt)	±	^{187}Re/^{188}Os	±	^{187}Os/^{188}Os	±	rho	Os_i	±
-70	25.912	0.063	230.6	1.4	61.9	0.2	832.4	3.7	4.25	0.02	0.592	0.72	0.03
-72	6.331	0.016	164.0	0.9	57.4	0.3	219.6	1.3	1.51	0.01	0.630	0.58	0.01
-75	2.841	0.007	129.3	0.8	48.3	0.4	117.1	1.1	0.94	0.01	0.680	0.44	0.01
-80	0.761	0.003	95.7	1.0	36.7	0.7	41.2	0.9	0.70	0.02	0.697	0.52	0.02
-85	1.707	0.005	158.6	1.3	61.1	0.8	55.6	0.8	0.68	0.01	0.694	0.44	0.01
-87	0.136	0.002	142.4	2.6	57.1	2.3	4.7	0.2	0.35	0.02	0.663	0.33	0.02
-90	1.859	0.005	168.1	1.3	65.0	0.9	56.9	0.8	0.65	0.01	0.694	0.41	0.01
-92	0.597	0.003	153.8	2.9	60.8	2.4	19.5	0.8	0.47	0.03	0.703	0.39	0.03
-93	9.343	0.023	240.9	1.3	84.9	0.5	219.0	1.3	1.44	0.01	0.631	0.52	0.01
-94	0.282	0.002	96.8	0.8	37.6	0.5	14.9	0.2	0.62	0.01	0.620	0.56	0.01
-96	1.005	0.003	100.4	1.1	38.1	0.8	52.5	1.1	0.81	0.02	0.699	0.58	0.02
-98	0.945	0.003	106.4	1.2	40.4	0.8	46.5	1.0	0.79	0.02	0.698	0.59	0.02
-101	0.141	0.002	94.3	1.8	36.7	1.5	7.6	0.3	0.59	0.03	0.666	0.56	0.03
-102	0.109	0.002	73.0	1.4	28.4	1.1	7.6	0.3	0.60	0.03	0.641	0.57	0.03
-103	10.152	0.025	213.3	1.1	73.0	0.3	276.5	1.5	1.70	0.01	0.623	0.53	0.01
-106	1.215	0.004	101.8	0.9	38.5	0.5	62.8	0.9	0.83	0.02	0.692	0.57	0.02

All uncertainties are given at 2σ level.
Os_i values are determined using the Wuchiapingian–Changhsingian boundary age of 254.14 Ma (Shen et al., 2019b).
Rho is the associated error correlation.

Table 3.1 Organic petrology data. Inertinite abundance data is calculated as volume percent on a whole rock basis.

Sample ID	Depth (cm)	Mineral	Solid Bitumen	Tasmanites	Inertinites	Inertinite abundance-whole rock (%)
B1-03	70	486	11	2	1	0.2
B1-02	65	487	11	1	1	0.2
B1-01	60	488	10	1	1	0.2
BMC_1_02	50	490	6	2	2	0.4
BMC_5	45	478	11	0	11	2.2
BMC_10	40	482	9	1	8	1.6
BMC_15	35	490	5	3	2	0.4
BMC_20	30	492	5	2	1	0.2
BMC_21	29	484	13	0	3	0.6
BMC_22	28	492	6	2	0	0
BMC_23	27	493	6	1	0	0
BMC_24	26	490	10	0	0	0
BMC_25	25	492	8	0	0	0
BMC_30	20	490	9	1	0	0
BMC_35	15	491	8	1	0	0
BMC_40	10	486	11	3	0	0
BMC_45	5	488	7	5	0	0
BMC_51	0	496	1	3	0	0
754	22982	490	5	4	1	0.2
754_4	22992	498	1	1	0	0
754_6	22997	486	8	5	1	0.2
754_8	23002	485	13	0	2	0.4
755_8	23033	486	11	2	1	0.2
761_6	23214	475	20	3	2	0.4
762_6	23241	482	8	7	3	0.6
764	23287	490	6	3	1	0.2
771_6	23515	493	5	0	2	0.4
774_10.5	23618	494	6	0	0	0
776	23652	464	35	0	1	0.2
776_9.5	23677	487	13	0	0	0
776_11	23680	488	10	2	0	0
777_2.5	23689	489	10	1	0	0
777_5.3	23696	487	13	0	0	0
777_6	23698	487	11	2	0	0
777_9	23706	270	8	0	0	0
778_2	23719	479	19	2	0	0
778_7	23731	488	11	1	0	0

To be continued.

Continue:

784_1.5	23900	458	0	42	0	0
784_5.5	23910	483	17	0	0	0
784_6.5	23913	403	2	1	0	0
784_8	23917	495	0	5	0	0
784_10	23922	491	9	0	0	0
801_3	24422	488	0	12	0	0
801_7	24432	336	5	11	0	0
801_9	24437	422	5	2	0	0
802	24445	425	2	16	0	0
802_1.5	24449	487	1	12	0	0
802_9	24468	493	2	5	0	0
ZL-16-01	313	478	13	8	1	0.2
ZL-15-03	308	478	15	6	1	0.2
ZL_15_01	300	472	14	12	2	0.4
ZL_13_01	250	468	15	15	2	0.4
ZL_12-01	245	464	26	7	3	0.6
ZL_06_06	110.25	469	18	12	1	0.2
ZL_06_04	107.75	456	24	18	2	0.4
ZL_06_03	106.5	453	35	12	0	0
ZL_06_02	105.25	463	14	18	5	1
ZL-01-03	45	486	10	2	2	0.4
ZL-01-02	43	485	14	3	1	0.2
ZLV_01	24	485	14	3	1	0.2
ZLV_02	21	314	4	4	0	0
ZLV_04	15	314	4	4	0	0
ZLV_07	6	472	11	17	0	0
ZLV_09	0	484	5	11	0	0
WCB_B3_02	96	474	8	15	3	0.6
WCB_B3_04	92	472	7	15	6	1.2
WCB_B3_06	88	474	4	20	2	0.4
WCB_B3_08	84	466	15	18	1	0.2
WCB_B2_01	66	469	11	19	1	0.2
WCB_B2_07	62	459	10	27	4	0.8
WCB_B2_09	59	472	9	17	2	0.4
WCB_B1_02	28	461	23	13	3	0.6
WCB_FF_02	20	460	11	29	0	0
WCB_FF_04	16	470	7	23	0	0
WCB_FF_06	12	461	8	31	0	0
WCB_FF_08	8	479	7	14	0	0
WCB_FF_10	4	471	4	25	0	0
WCB_FF_12	0	468	14	18	0	0

To be continued.

Continue:

JPC_D8	360	494	3	3	0	0
JPC_D6	355	492	4	4	0	0
JPC_D3	350	489	8	3	0	0
JPC_D1	345	494	4	2	0	0
JPC_FF_02	22	493	5	2	0	0
JPC_FF_04	18	495	4	1	0	0
JPC_FF_06	14	489	11	0	0	0
JPC_FF_08	10	482	17	1	0	0
JPC_FF_10	6	493	7	0	0	0

Table 3.2 Inertinite abundance data calculated as volume percent on mineral-free basis.

Sample ID	Mineral	Solid Bitumen	Tasmanites	Inertinite	Inertinite abundance-mineral free (%)
B1-03	486	11	2	1	7.1
B1-02	487	11	1	1	7.7
B1-01	488	10	1	1	8.3
BMC_1_02	490	6	2	2	20.0
BMC_5	478	11	0	11	50.0
BMC_10	482	9	1	8	44.4
BMC_15	490	5	3	2	20.0
BMC_20	492	5	2	1	12.5
BMC_21	484	13	0	3	18.8
754	490	5	4	1	10.0
754_6	486	8	5	1	7.1
754_8	485	13	0	2	13.3
755_8	486	11	2	1	7.1
761_6	475	20	3	2	8.0
762_6	482	8	7	3	16.7
764	490	6	3	1	10.0
771_6	493	5	0	2	28.6
776	464	35	0	1	2.8
ZL-16-01	478	13	8	1	4.5
ZL-15-03	478	15	6	1	4.5
ZL_15_01	472	14	12	2	7.1
ZL_13_01	468	15	15	2	6.3
ZL_12-01	464	26	7	3	8.3
ZL_06_06	469	18	12	1	3.2
ZL_06_04	456	24	18	2	4.5
ZL_06_02	463	14	18	5	13.5
ZL-01-03	486	10	2	2	14.3
ZL-01-01	485	14	3	1	5.6
ZLV_01	485	14	3	1	5.6
WCB_B3_02	474	8	15	3	11.5
WCB_B3_04	472	7	15	6	21.4
WCB_B3_06	474	4	20	2	7.7
WCB_B3_08	465	15	18	1	2.9
WCB_B2_01	469	11	19	1	3.2
WCB_B2_07	459	10	27	4	9.8
WCB_B2_09	472	9	17	2	7.1
WCB_B1_02	461	23	13	3	7.7
average					11.9
s.d.					10.4

To be continued.

Continue:

value used for pO_2 % calculation		pO_2 %	formular	
average	11.90	24.8	(1)	
average	11.90	27.1	(2)	
average	11.90	23.8	(3)	
Average – s.d.	1.52	19.4	(4)	shaded area
Average + s.d.	22.34	28.0	(5)	shaded area

Table 3.3 Inertinite reflectance data.

Sample ID	Inertinite reflectance (%)	No. of measurements	s.d.
B1-03	1.98	101	0.93
B1-02	1.94	32	0.63
B1-01	1.74	100	0.93
BMC_1_02	1.91	100	0.63
BMC_5	3.17	100	1.35
BMC_10	2.64	100	1.1
BMC_15	2.05	100	1.04
BMC_20	1.86	100	0.99
BMC_21	2.08	100	1.27
754_6	2.85	104	0.9
754_8	2.78	100	0.78
755_8	2.25	100	0.71
761_6	2.89	100	1
762_6	3.16	100	1.11
764	2.83	100	1.27
771_6	2.26	100	0.86
ZL-16-01	2.07	101	0.88
ZL-15-03	2.14	100	0.68
ZL_15_01	2.36	100	0.71
ZL_13_01	2.93	100	1.06
ZL_12-01	2.31	100	0.85
ZL_06_02	2.95	100	0.87
WCB_B3_02	2.69	100	1.09
WCB_B3_04	2.72	100	0.82
WCB_B3_06	2.19	100	1.09
WCB_B3_08	2.55	100	0.88
WCB_B2_01	2.54	100	1.09
WCB_B2_07	2.11	100	0.92
WCB_B2_09	2.90	100	1.27
WCB_B1_02	2.42	100	0.77

Table 3.4 Re–Os abundance and isotope data. Initial Os isotope composition (Os_i) is calculated at 371.93.2 Ma (Percival et al., 2018). All uncertainties are at 2σ level. Rho (ρ) is the associated error correlation (Ludwig, 1980).

Sample ID	Re (ppb)	±	Os (ppt)	±	^{192}Os (ppt)	±	$^{187}Re/^{188}Os$	±	$^{187}Os/^{188}Os$	±	rho	Os_i[a]	±
WCB-FF-01	14.57	0.04	345.93	1.94	115.36	0.57	251.34	1.38	1.95	0.01	0.63	0.39	0.02
WCB-FF-02	9.95	0.06	283.33	1.41	96.36	0.41	205.36	1.55	1.77	0.01	0.39	0.49	0.02
WCB_FF_04	8.32	0.02	219.24	1.11	74.25	0.31	222.83	1.10	1.81	0.01	0.60	0.42	0.02
WCB_FF_06	7.90	0.03	232.14	1.16	80.00	0.35	196.40	1.08	1.64	0.01	0.57	0.42	0.02
WCB_FF_08	6.95	0.02	258.94	1.22	92.47	0.42	149.51	0.80	1.32	0.01	0.59	0.39	0.01
WCB_FF_10	10.10	0.03	253.18	1.32	84.84	0.37	236.75	1.19	1.91	0.01	0.61	0.43	0.02
WCB-FF-12	3.97	0.02	84.01	0.55	27.56	0.17	286.58	2.11	2.11	0.02	0.60	0.33	0.03
BMC_1_02	13.16	0.03	223.71	1.22	69.43	0.27	377.08	1.75	2.66	0.01	0.60	0.31	0.03
BMC_5	5.23	0.01	197.32	1.10	70.70	0.43	147.05	0.97	1.29	0.01	0.65	0.38	0.02
BMC_10	3.82	0.01	133.33	0.77	46.87	0.29	162.09	1.09	1.46	0.01	0.65	0.46	0.02
BMC_15	2.55	0.01	214.31	1.02	81.30	0.49	62.40	0.41	0.80	0.01	0.65	0.42	0.01
BMC_25	3.88	0.01	136.11	0.79	47.85	0.29	161.30	1.07	1.46	0.01	0.65	0.46	0.02
BMC_30	3.64	0.01	139.15	0.81	49.68	0.32	145.86	1.02	1.33	0.01	0.65	0.42	0.02
BMC_35	3.59	0.01	142.35	0.80	50.92	0.31	140.36	0.93	1.31	0.01	0.65	0.44	0.02
BMC_40	2.77	0.01	93.25	0.55	32.61	0.20	169.07	1.13	1.51	0.01	0.66	0.46	0.02
BMC_45	7.69	0.02	175.21	1.13	57.51	0.35	265.88	1.75	2.10	0.02	0.65	0.45	0.03
BMC_51	17.59	0.04	221.66	1.33	61.01	0.23	573.67	2.58	3.96	0.02	0.59	0.39	0.04
JPC_FF_01	9.98	0.02	124.39	0.99	33.92	0.21	585.35	3.93	4.07	0.04	0.66	0.43	0.06
JPC_FF_02	10.59	0.03	135.55	0.87	37.59	0.16	560.15	2.82	3.87	0.02	0.62	0.39	0.04
JPC_FF_04	9.25	0.02	137.11	0.84	40.42	0.17	455.17	2.28	3.20	0.02	0.61	0.37	0.03
JPC_FF_06	11.53	0.03	159.81	0.99	46.09	0.20	497.82	2.49	3.43	0.02	0.61	0.34	0.04
JPC_FF_08	11.72	0.03	165.02	1.01	46.94	0.19	496.54	2.51	3.59	0.02	0.58	0.50	0.04
JPC_FF_10	17.16	0.04	180.39	1.15	46.08	0.18	740.68	3.41	4.85	0.03	0.59	0.25	0.05

To be Continued.

Continue:

776.00	5.47	0.01	202.30	1.05	71.76	0.37	151.52	0.87	1.38	0.01	0.64	0.44	0.02
776_5	3.86	0.01	152.03	1.04	54.87	0.48	139.99	1.27	1.23	0.02	0.68	0.36	0.02
776_8.5	5.09	0.01	171.26	1.09	61.20	0.46	165.38	1.31	1.32	0.01	0.67	0.29	0.02
776_9.5	3.92	0.01	152.08	0.90	54.25	0.36	143.63	1.02	1.33	0.01	0.66	0.44	0.02
776_11	3.86	0.01	145.36	0.86	52.03	0.35	147.53	1.06	1.30	0.01	0.66	0.39	0.02
777_2.5	3.30	0.01	131.82	0.92	47.04	0.41	139.39	1.27	1.33	0.02	0.68	0.46	0.02
777_5.3	3.10	0.01	132.57	0.91	47.76	0.42	129.09	1.18	1.25	0.02	0.68	0.44	0.02
777_6	3.23	0.01	136.38	0.93	49.10	0.43	131.07	1.19	1.25	0.02	0.68	0.44	0.02
777_9	3.81	0.01	160.69	1.08	58.45	0.51	129.67	1.17	1.16	0.01	0.68	0.36	0.02
778_2	4.55	0.01	158.88	0.95	56.48	0.38	160.24	1.14	1.36	0.01	0.66	0.37	0.02
778_7	6.32	0.02	175.69	0.97	58.57	0.28	214.64	1.15	1.95	0.01	0.63	0.62	0.02
ZLV_01	9.96	0.02	265.64	1.36	89.10	0.38	222.43	1.09	1.90	0.01	0.61	0.51	0.02
ZLV_02	7.95	0.02	247.83	1.25	86.00	0.40	183.92	0.96	1.58	0.01	0.62	0.44	0.02
ZLV_03	5.56	0.01	184.27	1.02	64.53	0.36	171.53	1.05	1.50	0.01	0.65	0.43	0.02
ZLV_04	2.25	0.01	89.05	0.71	31.76	0.34	141.22	1.56	1.34	0.02	0.69	0.46	0.03
ZLV_05	1.71	0.00	61.33	0.76	21.80	0.44	156.10	3.21	1.37	0.04	0.70	0.40	0.06
ZLV_06	5.79	0.01	182.11	1.04	64.31	0.39	179.15	1.17	1.42	0.01	0.66	0.31	0.02
ZLV_07	6.30	0.02	200.60	1.07	69.65	0.35	179.95	1.02	1.58	0.01	0.64	0.46	0.02
ZLV_08	6.04	0.01	317.75	1.50	119.12	0.67	100.95	0.62	0.90	0.01	0.65	0.28	0.01
ZLV_09	10.11	0.02	216.87	1.18	69.95	0.30	287.53	1.41	2.27	0.01	0.61	0.49	0.02
754.00	27.16	0.07	312.74	1.95	82.56	0.32	654.41	2.96	4.45	0.02	0.60		
754_4	0.87	0.00	48.54	0.71	17.84	0.48	97.46	2.66	1.07	0.04	0.70		
754_6	18.37	0.04	250.37	1.60	70.12	0.31	521.07	2.61	3.76	0.02	0.62		
754_8	25.52	0.06	345.66	2.34	95.38	0.45	532.30	2.81	3.93	0.03	0.63		
755_8	24.61	0.06	309.52	1.88	85.82	0.34	570.55	2.64	3.88	0.02	0.61		
761_6	22.63	0.06	307.89	1.76	87.43	0.31	514.99	2.23	3.61	0.02	0.58		

To be continued:

Continue:

762_6	24.74	0.06	332.76	1.89	95.26	0.34	516.64	2.24	3.52	0.02	0.58
764.00	15.61	0.04	190.26	1.19	51.37	0.20	604.46	2.81	4.18	0.02	0.60
771_6	13.84	0.03	233.03	1.32	71.07	0.28	387.27	1.81	2.84	0.02	0.60
774_10.5	6.43	0.02	164.82	0.96	54.85	0.29	233.27	1.34	1.97	0.01	0.64
784_1.5	10.08	0.02	115.92	1.52	30.49	0.42	658.01	9.24	4.50	0.09	0.70
784_5.5	12.49	0.03	199.73	1.96	60.94	0.64	407.86	4.43	2.83	0.04	0.69
784_6.5	7.97	0.02	126.69	1.55	36.40	0.50	435.69	6.12	3.48	0.07	0.70
784_8	12.11	0.03	152.31	1.65	41.75	0.44	577.17	6.28	4.01	0.06	0.69
784_10	11.83	0.03	156.47	1.67	43.56	0.46	540.43	5.88	3.83	0.06	0.69
801_3	31.14	0.08	394.47	3.74	110.60	0.96	560.20	5.06	3.75	0.05	0.68
801_7	31.37	0.08	375.73	3.65	101.90	0.89	612.41	5.53	4.13	0.05	0.68
801_9	26.64	0.06	459.79	3.89	144.51	1.26	366.72	3.32	2.53	0.03	0.68
802.00	32.21	0.08	384.99	2.29	103.89	0.37	616.85	2.70	4.19	0.02	0.58
802_1.5	22.63	0.09	262.63	1.59	70.34	0.26	640.07	3.41	4.28	0.02	0.48
802_9	24.90	0.06	303.64	3.31	82.55	0.87	600.19	6.52	4.10	0.06	0.69
ZL-01-04	10.56	0.03	175.16	1.13	53.05	0.27	396.21	2.24	2.91	0.02	0.64
ZL-01-03	25.81	0.06	340.74	1.96	95.24	0.34	539.13	2.32	3.78	0.02	0.58
ZL-01-02	22.38	0.05	336.27	1.84	99.29	0.35	448.42	1.94	3.18	0.02	0.58

[a]Only the samples close to the F–F interval were calculated for Os_i.

Table 3.5 Major element data.

Sample ID	Al2O3 %	SiO2 %	TiO2 %	Si %	Ti %	Al %	Si/Al	Ti/Al
WCB B3-02	13.665	66.263	0.857	30.973	0.514	7.232	4.283	0.071
WCB B3-08	15.386	60.254	0.868	28.164	0.520	8.143	3.459	0.064
WCB 02-01	12.813	58.414	0.775	27.304	0.464	6.781	4.026	0.068
WCB B2-09	14.535	63.342	0.865	29.607	0.518	7.693	3.849	0.067
WCB 01-02	17.226	55.885	0.858	26.122	0.514	9.117	2.865	0.056
WCB-FF-01	15.288	58.642	0.893	27.366	0.535	8.087	3.384	0.066
WCB-FF-02	15.647	59.476	0.904	27.755	0.542	8.277	3.353	0.065
WCB_FF_04	15.402	61.266	0.912	28.591	0.547	8.148	3.509	0.067
WCB_FF_06	14.948	60.678	0.912	28.316	0.547	7.907	3.581	0.069
WCB_FF_08	15.550	61.949	0.907	28.910	0.544	8.226	3.514	0.066
WCB_FF_10	16.064	60.241	0.911	28.112	0.546	8.498	3.308	0.064
WCB-FF-12	17.036	60.367	0.937	28.171	0.562	9.012	3.126	0.062
BMC B1-03	15.46	62.857	0.919	29.381	0.551	8.182	3.591	0.067
BMC B1-02	15.223	63.683	0.928	29.767	0.556	8.057	3.695	0.069
BMC B1-01	15.636	62.791	0.916	29.350	0.549	8.275	3.547	0.066
BMC_1_02	14.722	59.209	0.853	27.631	0.511	7.788	3.548	0.066
BMC_5	13.807	61.615	0.820	28.754	0.491	7.304	3.937	0.067
BMC_10	11.374	64.052	0.774	29.891	0.464	6.017	4.968	0.077
BMC_15	14.406	58.430	0.864	27.267	0.518	7.621	3.578	0.068
BMC_25	14.297	63.597	0.908	29.679	0.544	7.563	3.924	0.072
BMC_30	15.275	63.269	0.928	29.526	0.556	8.080	3.654	0.069
BMC_35	15.205	63.029	0.969	29.414	0.581	8.043	3.657	0.072
BMC_40	13.603	68.075	0.987	31.768	0.592	7.196	4.415	0.082
BMC_45	15.804	62.663	0.992	29.243	0.595	8.360	3.498	0.071
BMC_51	16.888	60.082	1.017	28.038	0.610	8.934	3.138	0.068
JPC D8	18.129	60.901	1.009	28.466	0.605	9.595	2.967	0.063
JPC D6	18.621	59.361	0.972	27.747	0.583	9.855	2.815	0.059
JPC D3	17.849	59.961	0.956	28.027	0.573	9.447	2.967	0.061
JPC D-01	16.493	63.474	0.968	29.669	0.580	8.729	3.399	0.066
JPC_FF_01	16.343	62.322	1.038	29.084	0.622	8.645	3.364	0.072
JPC_FF_02	16.091	63.684	1.044	29.719	0.626	8.512	3.491	0.074
JPC_FF_04	16.701	63.095	1.057	29.444	0.633	8.835	3.333	0.072
JPC_FF_06	16.721	61.486	1.039	28.693	0.623	8.845	3.244	0.070
JPC_FF_08	16.950	61.687	1.026	28.787	0.615	8.967	3.211	0.069
JPC_FF_10	16.702	61.891	1.034	28.882	0.620	8.835	3.269	0.070
754	14.224	63.922	0.868	29.830	0.520	7.524	3.964	0.069
754_4	20.019	56.993	0.902	26.597	0.541	10.59	2.511	0.051
754_6	13.395	67.403	0.858	31.455	0.514	7.086	4.439	0.073
754_8	13.561	66.814	0.892	31.180	0.535	7.174	4.346	0.075
755_8	12.933	67.171	0.830	31.346	0.497	6.842	4.582	0.073

To be continued.

Continue:

761_6	16.014	60.869	0.899	28.451	0.539	8.475	3.357	0.064
762_6	13.650	65.291	0.896	30.469	0.537	7.221	4.220	0.074
764	14.851	64.465	0.872	30.084	0.523	7.856	3.829	0.067
771_6	15.569	60.942	0.889	28.440	0.533	8.236	3.453	0.065
774_10.5	12.260	62.273	0.787	29.061	0.472	6.486	4.481	0.073
776	14.198	60.448	0.838	28.209	0.502	7.511	3.756	0.067
776_5	13.546	62.930	0.878	29.367	0.526	7.166	4.098	0.073
776_8.5	15.141	61.560	0.911	28.728	0.546	8.010	3.587	0.068
776_9.5	15.857	61.000	0.919	28.467	0.551	8.388	3.394	0.066
776_11	15.957	60.388	0.922	28.181	0.553	8.441	3.338	0.065
777_2.5	15.790	61.854	0.942	28.865	0.565	8.353	3.456	0.068
777_5.3	15.417	62.735	0.953	29.276	0.571	8.156	3.590	0.070
777_6	15.010	63.465	0.936	29.617	0.561	7.940	3.730	0.071
777_9	15.356	62.361	0.953	29.102	0.571	8.123	3.582	0.070
778_2	16.399	60.846	0.941	28.395	0.564	8.675	3.273	0.065
778_7	16.333	61.842	0.973	28.860	0.583	8.640	3.340	0.067
784_1.5	15.727	63.323	0.996	29.551	0.597	8.320	3.552	0.072
784_5.5	15.126	64.451	0.995	30.077	0.596	8.002	3.759	0.075
784_6.5	15.005	64.091	0.978	29.909	0.586	7.938	3.768	0.074
784_8	15.515	63.768	0.993	29.758	0.595	8.207	3.626	0.073
784_10	15.381	61.653	0.975	28.771	0.584	8.137	3.536	0.072
801_3	16.819	62.897	0.962	29.352	0.577	8.897	3.299	0.065
801_7	16.896	61.223	0.984	28.571	0.590	8.938	3.197	0.066
801_9	20.082	58.137	0.993	27.131	0.595	10.62	2.554	0.056
802	15.905	63.100	1.013	29.447	0.607	8.414	3.500	0.072
802_1.5	17.334	59.010	0.987	27.538	0.592	9.170	3.003	0.065
802_9	14.994	65.491	1.009	30.562	0.605	7.932	3.853	0.076
ZL-16-01	14.387	64.657	0.87	30.222	0.521	7.614	3.969	0.068
ZL-15-01	13.853	65.129	0.873	30.443	0.523	7.332	4.152	0.071
ZL-13-01	15.733	60.513	0.909	28.285	0.545	8.327	3.397	0.065
ZL-12-01	15.806	61.458	0.933	28.727	0.559	8.365	3.434	0.067
ZL-06-06	17.424	58.98	0.902	27.568	0.541	9.222	2.990	0.059
ZL-06-02	16.379	60.152	0.9	28.116	0.539	8.669	3.243	0.062
ZL-01-04	18.608	57.094	0.893	26.644	0.535	9.844	2.707	0.054
ZL-01-03	17.042	56.753	0.878	26.485	0.526	9.015	2.938	0.058
ZL-01-02	16.271	57.101	0.869	26.647	0.521	8.607	3.096	0.061
ZLV_01	15.061	57.064	0.876	26.630	0.525	7.967	3.342	0.066
ZLV_02	16.427	59.199	0.937	27.626	0.562	8.690	3.179	0.065
ZLV_03	15.849	58.010	0.888	27.071	0.532	8.384	3.229	0.063
ZLV_04	14.429	65.154	0.942	30.405	0.565	7.633	3.983	0.074
ZLV_05	14.275	67.898	0.908	31.686	0.544	7.551	4.196	0.072

To be continued.

Continue:

ZLV_06	15.625	61.166	0.963	28.544	0.577	8.266	3.453	0.070
ZLV_07	16.414	60.910	0.954	28.425	0.572	8.683	3.274	0.066
ZLV_08	16.272	60.374	0.934	28.175	0.560	8.608	3.273	0.065
ZLV_09	16.590	61.240	0.973	28.579	0.583	8.776	3.256	0.066

Table 3.6 Trace element data.

Sample ID	Mn (ppm)	V (ppm)	Ni (ppm)	Mo (ppm)	V/(V+Ni)
WCB-FF-01	283.24	127.71	126.42	8.04	0.50
WCB-FF-02	274.07	129.10	115.21	9.29	0.53
WCB_FF_06	289.53	118.66	117.48	11.37	0.50
WCB_FF_08	271.11	118.75	94.44	24.71	0.56
WCB_FF_10	269.39	120.04	95.65	42.35	0.56
WCB-FF-12	275.15	123.76	64.22	13.14	0.66
BMC_5	459.79	102.73	49.45	17.64	0.68
BMC_10	631.36	84.08	41.26	16.10	0.67
BMC_15	521.85	108.31	43.77	9.97	0.71
BMC_25	412.34	105.32	41.56	4.57	0.72
BMC_30	309.54	113.88	42.34	8.63	0.73
BMC_35	320.66	113.92	44.37	5.90	0.72
BMC_40	258.11	97.71	38.38	7.06	0.72
BMC_45	264.45	114.67	51.58	17.87	0.69
BMC_51	270.16	127.12	62.54	13.31	0.67
JPC_FF_02	292.84	115.94	73.46	13.10	0.61
JPC_FF_04	265.60	118.95	74.48	17.39	0.61
JPC_FF_08	290.42	125.78	87.17	32.17	0.59
JPC_FF_10	287.41	120.80	84.63	27.24	0.59
754.00	250.18	113.23	54.46	28.46	0.68
754_4	276.03	155.46	33.13	3.92	0.82
754_6	217.43	106.15	40.87	16.50	0.72
755_8	232.99	103.95	45.78	35.73	0.69
761_6	255.77	125.68	56.19	37.10	0.69
762_6	300.25	110.12	44.72	35.32	0.71
764.00	273.83	109.29	44.88	26.48	0.71
771_6	365.14	121.69	95.92	7.71	0.56
774_10.5	570.69	97.16	58.38	7.63	0.62
776.00	471.01	106.60	41.80	7.04	0.72
776_5	448.03	101.10	38.94	7.53	0.72
776_9.5	297.88	119.38	45.57	9.88	0.72
776_11	306.92	119.86	46.48	11.70	0.72
777_2.5	291.69	119.83	41.64	12.74	0.74
777_6	295.87	114.17	43.01	13.34	0.73
777_9	331.82	116.19	43.72	18.97	0.73
778_2	307.47	124.62	47.58	21.20	0.72
778_7	284.70	122.68	55.17	25.25	0.69
784_1.5	287.28	116.86	52.09	8.23	0.69
784_6.5	264.41	110.66	58.46	25.41	0.65
784_10	301.80	119.39	59.37	23.29	0.67

To be continued:

Continue:

801_3	261.53	126.52	54.35	3.67	0.70
802.00	258.11	131.52	58.56	31.91	0.69
802_1.5	267.71	142.64	59.54	30.02	0.71
ZL-01-04	376.23	140.02	50.83	4.75	0.73
ZL-01-03	398.43	134.24	88.19	18.61	0.60
ZL-01-02	374.25	132.02	90.40	20.54	0.59
ZLV_01	399.97	117.50	100.41	8.77	0.54
ZLV_02	272.18	127.99	84.97	11.74	0.60
ZLV_03	277.22	122.85	89.63	20.04	0.58
ZLV_04	474.36	106.55	49.41	12.47	0.68
ZLV_06	309.82	117.03	87.30	26.29	0.57
ZLV_07	272.58	123.11	82.80	42.39	0.60
ZLV_08	282.15	121.04	83.50	42.08	0.59
ZLV_09	293.54	119.44	74.31	38.03	0.62

Table 3.7 Bitumen reflectance data.

Sample ID	BRo (%)	No. of measurements	s.d.
B1-03	0.56	50	0.073
B1-02	0.66	62	0.158
B1-01	0.53	51	0.084
BMC_1_02	0.66	50	0.158
BMC_5	0.64	50	0.167
BMC_10	0.73	50	0.083
BMC_15	0.56	50	0.076
BMC_20	0.60	51	0.098
BMC_21	0.56	70	0.016
BMC_22	0.65	50	0.115
BMC_25	0.55	50	0.080
BMC_30	0.56	100	0.112
BMC_35	0.54	50	0.106
BMC_40	0.60	53	0.118
BMC_45	0.59	50	0.106
BMC_51	0.57	33	0.076
754_6	0.60	25	0.163
755_8	0.62	27	0.146
761_6	0.61	81	0.086
762_6	0.61	25	0.146
771_6	0.66	25	0.141
776	0.58	25	0.078
776_9.5	0.68	30	0.118
776_11	0.60	26	0.104
777_2.5	0.64	26	0.099
777_5.3	0.58	25	0.070
777_6	0.56	26	0.066
777_9	0.56	26	0.096
778_7	0.60	25	0.125
784_1.5	0.63	25	0.106
784_5.5	0.66	30	0.072
784_8	0.61	26	0.113
801_7	0.64	28	0.160
801_9	0.63	23	0.180
802	0.63	20	0.140
802_9	0.53	14	0.139
ZL-16-01	0.73	25	0.220
ZL_06_04	0.70	25	0.165
ZL_06_02	0.62	25	0.167
ZL-01-03	0.67	50	0.104

To be continued:

Continue:

ZL-01-02	0.65	50	0.090
ZLV_02	0.60	25	0.070
ZLV_04	0.63	25	0.127
WCB_B3_02	0.49	30	0.056
WCB_B3_04	0.46	50	0.058
WCB_B3_06	0.49	30	0.099
WCB_B3_08	0.62	50	0.091
WCB_B2_01	0.55	70	0.116
WCB_B2_07	0.48	50	0.092
WCB_B2_09	0.46	50	0.093
WCB_B1_02	0.57	30	0.090
WCB_FF_02	0.50	59	0.089
WCB_FF_06	0.59	30	0.096
WCB_FF_08	0.43	30	0.069
WCB_FF_10	0.50	30	0.107
WCB_FF_12	0.51	30	0.081
JPC_D8	0.67	50	0.142
JPC_D6	0.68	50	0.106
JPC_D3	0.57	30	0.137
JPC_D1	0.55	50	0.061
JPC_FF_02	0.69	50	0.087
JPC_FF_04	0.72	50	0.088
JPC_FF_06	0.69	52	0.109
JPC_FF_08	0.70	30	0.077
JPC_FF_10	0.67	50	0.082

Table 3.8 TOC and programmed pyrolysis data.

Sample ID	TOC	S1	S2	S3	Tmax (°C)	HI	OI	PI	S2/S3	S1/TOC*100
WCB-FF-01	5.23	2.09	20.21	0.16	442	388	3	0.09	126	40
WCB-FF-02	4.03	1.89	16.45	0.5	443	408	12	0.1	33	47
WCB_FF_04	3.59	1.75	13.19	0.24	443	367	7	0.12	55	49
WCB_FF_06	4.3	1.93	17.39	0.35	443	404	8	0.1	50	45
WCB_FF_08	3.03	1.44	11.23	0.19	443	371	6	0.11	59	48
WCB_FF_10	3.13	1.59	14.15	0.26	446	452	8	0.1	54	51
WCB-FF-12	0.69	1.03	1.57	0.32	442	228	46	0.4	5	149
BMC_1_02	2.4	1.28	4.94	0.27	440	206	11	0.21	18	53
BMC_5	2.51	1.25	5.11	0.21	442	204	8	0.2	24	50
BMC_10	2.05	1.11	4.28	0.39	442	209	19	0.21	11	54
BMC_15	2.89	1.5	6.45	0.33	442	223	11	0.19	20	52
BMC_25	2.69	1.73	6.28	0.24	444	233	9	0.22	26	64
BMC_30	2.09	1.44	5.03	0.21	442	241	10	0.22	24	69
BMC_35	2.57	1.8	6.65	0.25	442	259	10	0.21	27	70
BMC_40	1.78	1.16	4.29	0.16	441	241	9	0.21	27	65
BMC_45	2.13	1.36	5.48	0.26	442	257	12	0.2	21	64
BMC_51	1.27	0.73	2.55	0.22	443	201	17	0.22	12	57
JPC_FF_01	1.25	0.5	2.03	0.21	444	161	17	0.2	10	40
JPC_FF_02	1.23	0.52	1.84	0.23	443	150	19	0.22	8	42
JPC_FF_04	1.22	0.54	1.76	0.22	444	144	18	0.23	8	44
JPC_FF_06	1.63	0.64	2.48	0.24	442	152	15	0.21	10	39
JPC_FF_08	1.69	0.68	2.59	0.24	444	153	14	0.21	11	40
JPC_FF_10	1.74	0.68	2.85	0.2	444	164	11	0.19	14	39

To be continued:

Continue:

754	2.83	1.25	6.66	0.19	446	235	7	0.16	35	44
754_4	0.32	0.08	0.13	0.28	437	41	88	0.4	0.5	25
754_6	1.96	0.9	3.57	0.17	444	182	9	0.2	21	46
754_8	2.44	1.18	4.87	0.19	446	200	8	0.19	26	48
755_8	2.74	1.22	6.34	0.18	444	231	7	0.16	35	45
761_6	2.86	1.33	6.71	0.25	443	235	9	0.17	27	47
762_6	3.01	1.3	7.32	0.17	446	243	6	0.15	43	43
764	1.72	0.83	3.25	0.2	445	189	12	0.2	16	48
771_6	2.65	0.99	4.35	0.22	445	164	8	0.18	20	37
774_10.5	2.48	0.97	4.22	0.24	444	170	10	0.19	18	39
776	3.53	1.58	7.16	0.19	447	203	5	0.18	38	45
776_5	3.25	1.68	7.52	0.17	445	231	5	0.18	44	52
776_8.5	3.02	1.61	6.53	0.17	442	216	6	0.2	38	53
776_9.5	3.03	1.47	5.99	0.15	444	198	5	0.2	40	49
776_11	2.71	1.43	5.50	0.14	445	203	5	0.21	39	53
777_2.5	2.57	1.37	5.38	0.15	444	209	6	0.2	36	53
777_5.3	2.41	1.30	4.52	0.18	443	188	7	0.22	25	54
777_6	2.68	1.41	5.77	0.18	445	215	7	0.2	32	53
777_9	3.05	1.65	6.17	0.15	444	202	5	0.21	41	54
778_2	2.48	1.34	5.54	0.12	444	223	5	0.19	46	54
778_7	1.9	1.27	3.77	0.17	445	198	9	0.25	22	67
784_1.5	1.18	0.55	1.98	0.19	446	168	16	0.22	10	47
784_5.5	2.17	1.15	3.85	0.21	445	177	10	0.23	18	53
784_6.5	1.76	0.85	2.8	0.27	442	159	15	0.23	10	48
784_8	2.06	0.87	3.02	0.21	443	147	10	0.22	14	42
784_10	1.71	0.75	2.02	0.2	445	118	12	0.27	10	44

To be continue.

Continue:

801_3	0.65	0.22	0.61	0.33	442	94	51	0.27	2	34
801_7	1.51	0.62	2.17	0.2	443	144	13	0.22	11	41
801_9	0.38	0.14	0.36	0.19	439	95	50	0.28	2	37
802	1.1	0.41	1.35	0.26	443	123	24	0.23	5	37
802_1.5	1.67	0.74	3.46	0.2	445	207	12	0.18	17	44
802_9	1.33	0.61	2.79	0.25	445	210	19	0.18	11	46
ZL-01-04	1.16	0.49	1.8	0.18	445	155	16	0.21	10	42
ZL-01-03	2.44	1.16	4.91	0.15	444	201	6	0.19	33	48
ZL-01-02	2.54	1.22	5.17	0.12	445	204	5	0.19	43	48
ZLV_01	4.3	2.07	11.23	0.18	444	261	4	0.16	62	48
ZLV_02	3.92	1.62	9.51	0.13	448	243	3	0.15	73	41
ZLV_03	3.26	1.61	7.29	0.28	444	224	9	0.18	26	49
ZLV_04	1.46	0.89	3.01	0.19	444	206	13	0.23	16	61
ZLV_05	1.04	0.71	2.02	0.24	441	194	23	0.26	8	68
ZLV_06	2.99	1.68	7.64	0.18	446	256	6	0.18	42	56
ZLV_07	2.85	1.43	6.82	0.12	448	239	4	0.17	57	50
ZLV_08	2.62	1.37	6.57	0.2	446	251	8	0.17	33	52
ZLV_09	2.22	1.3	5.19	0.18	448	234	8	0.2	29	59

Table 4.1 Re-Os data for Millville.

Depth (m)	Re (ppb)	±	Os (ppt)	±	^{192}Os (ppt)	±	^{187}Re/^{188}Os	±	^{187}Os/^{188}Os	±	rho	Os_i	±
269.58	5.84	0.01	206.4	0.9	80.7	0.5	144.0	0.9	0.559	0.005	0.653	0.42	0.006
270.16	7.96	0.02	229.2	0.9	89.6	0.5	176.9	1.0	0.561	0.004	0.635	0.40	0.005
270.74	8.67	0.02	262.8	0.9	103.0	0.5	167.5	0.9	0.532	0.004	0.625	0.38	0.004
271.17	6.44	0.02	241.8	1.0	94.8	0.5	135.3	0.8	0.538	0.004	0.624	0.41	0.005
271.58	9.00	0.02	259.1	0.9	101.0	0.5	177.3	0.9	0.582	0.004	0.624	0.42	0.005
271.91	8.03	0.02	271.6	1.1	106.4	0.6	150.2	0.9	0.536	0.004	0.632	0.40	0.005
272.15	9.38	0.02	321.9	1.2	126.5	0.6	147.5	0.8	0.513	0.004	0.634	0.38	0.004
272.73	10.38	0.03	257.3	0.9	100.5	0.5	205.5	1.1	0.564	0.004	0.581	0.37	0.005
273.31	10.23	0.02	181.8	0.7	70.2	0.3	289.9	1.4	0.654	0.004	0.611	0.38	0.005
273.63	11.40	0.03	177.0	0.6	68.8	0.3	329.6	1.6	0.604	0.004	0.616	0.30	0.005
273.89	7.85	0.02	197.6	0.7	77.9	0.4	200.4	1.1	0.487	0.004	0.635	0.30	0.005
274.07	10.22	0.02	218.2	0.8	84.8	0.4	239.8	1.2	0.606	0.004	0.612	0.38	0.005
274.20	5.64	0.01	119.6	0.5	46.6	0.3	240.6	1.6	0.581	0.005	0.658	0.36	0.006
274.46	5.32	0.01	102.6	0.5	39.8	0.3	266.4	2.1	0.632	0.007	0.674	0.38	0.009
274.75	6.44	0.02	92.1	0.4	35.4	0.2	362.5	2.1	0.703	0.005	0.644	0.37	0.007
275.04	6.11	0.01	95.1	0.4	36.8	0.2	329.8	2.2	0.636	0.005	0.659	0.33	0.008
275.36	6.28	0.02	88.3	0.4	34.0	0.2	368.1	2.2	0.693	0.005	0.640	0.35	0.007
275.62	6.34	0.02	96.6	0.4	37.1	0.2	339.8	2.2	0.693	0.006	0.660	0.38	0.008

All uncertainties are at 2σ level.
Rho is the associated error correlation (Ludwig, 1980).

Table 4.2 Re-Os data for Blake Nose.

Depth (m)	Re (ppb)	±	Os (ppt)	±	^{192}Os (ppt)	±	^{187}Re/^{188}Os	±	^{187}Os/^{188}Os	±	rho	Os_i	±
509.62	0.11	0.002	92.6	1.7	37.1	1.5	6.1	0.3	0.35	0.02	0.647	0.35	0.02
510.03	0.20	0.002	83.4	1.5	33.4	1.3	11.8	0.5	0.36	0.02	0.685	0.35	0.02
510.53	0.14	0.002	87.6	1.6	35.1	1.4	8.1	0.3	0.36	0.02	0.667	0.35	0.02
511.03	0.23	0.002	96.6	1.8	38.7	1.6	11.8	0.5	0.36	0.02	0.690	0.35	0.02
511.58	0.18	0.002	146.1	2.7	58.5	2.4	6.2	0.3	0.36	0.02	0.681	0.36	0.02
512.01	0.17	0.002	131.0	2.4	52.5	2.1	6.3	0.3	0.36	0.02	0.677	0.36	0.02
512.19	0.15	0.002	133.2	2.4	53.4	2.1	5.7	0.2	0.36	0.02	0.671	0.35	0.02
512.25	0.07	0.002	121.7	2.2	48.8	2.0	2.7	0.1	0.36	0.02	0.567	0.36	0.02
512.35	0.08	0.002	146.2	2.7	58.6	2.4	2.7	0.1	0.36	0.02	0.598	0.36	0.02
512.52	0.09	0.002	126.2	2.3	50.6	2.0	3.5	0.2	0.36	0.02	0.617	0.35	0.02
512.58	0.14	0.002	125.1	2.3	50.1	2.0	5.4	0.2	0.36	0.02	0.664	0.35	0.02
512.79	0.16	0.002	44.9	0.8	18.0	0.7	17.9	0.8	0.36	0.02	0.675	0.35	0.02
513.02	0.08	0.002	47.3	0.9	18.9	0.8	8.3	0.4	0.37	0.02	0.599	0.36	0.02
513.09	0.12	0.002	39.1	0.7	15.6	0.6	15.9	0.7	0.38	0.02	0.656	0.36	0.02
513.22	0.07	0.002	35.1	0.6	14.0	0.6	9.9	0.5	0.38	0.02	0.576	0.37	0.02
513.32	0.06	0.002	31.6	0.6	12.7	0.5	9.7	0.5	0.38	0.02	0.553	0.37	0.02
513.54	0.04	0.002	35.7	0.7	14.3	0.6	6.1	0.4	0.37	0.02	0.469	0.37	0.02
513.92	0.04	0.002	26.8	0.5	10.7	0.4	6.9	0.5	0.38	0.02	0.426	0.37	0.02

All uncertainties are at 2σ level.
Rho is the associated error correlation (Ludwig, 1980).

Table 4.3 Mercury, TOC and pyrite sulfur data for Millville.

Depth (m)	Hg (ppb)	TOC (wt. %)	Hg/TOC (ppb/ wt. %)	S-Pyrite (wt. %)
269.26	23.2	0.38	61.34	0.20
269.58	23.2	0.38	61.12	0.25
269.84	22.3	0.47	47.79	0.16
270.16	22.5	0.38	58.46	0.13
270.42	21.3	0.41	52.26	0.17
270.74	28.6	0.43	66.60	0.08
271.01	28.8	0.38	76.69	0.11
271.17	24.2	0.38	63.59	0.08
271.32	23.6	0.38	61.47	0.15
271.58	29.4	0.41	72.33	0.15
271.91	24.4	0.41	59.85	0.14
272.15	26	0.43	61.15	0.07
272.47	31.4	0.51	61.86	0.23
272.73	27	0.45	60.66	0.10
273.31	25.2	0.39	64.49	0.18
273.63	21.6	0.36	59.95	0.50
273.89	20.7	0.34	61.01	0.13
274.07	20.9	0.31	66.36	0.18
274.20	15.1	0.26	57.29	0.08
274.46	11.7	0.24	49.51	0.10
274.75	8.8	0.23	39.08	0.04
275.04	10.3	0.21	48.53	0.12
275.36	9.2	0.23	40.82	0.07
275.62	10.7	0.23	47.03	0.10
275.94	11.9	0.22	53.40	0.01
276.20	9.4	0.21	44.97	0.01

Table 4.4 Mercury, TOC and pyrite sulfur data for Blake Nose.

Depth (m)	Hg (ppb)	TOC (wt. %)	Hg/TOC (ppb/ wt. %)	S-Pyrite (wt. %)
509.36	8.2	0.07	122.07	0.02
509.62	21.7	0.12	179.92	0.01
509.84	9.5	0.11	83.84	0.02
510.03	3	0.13	23.76	0.18
510.53	4.8	0.13	36.24	0.00
511.03	16.1	0.15	106.38	0.12
511.58	33.3	0.16	209.42	0.06
512.01	5.1	0.23	22.06	0.08
512.13	3.1	0.10	30.17	0.03
512.19	5	0.07	68.87	0.16
512.25	2.9	0.04	80.24	0.19
512.35	3.8	0.23	16.31	0.03
512.52	5.8	0.06	97.98	0.20
512.58	6.9	0.05	148.37	0.00
512.79	2.1	0.06	33.81	0.03
513.02	3.8	0.12	32.42	0.00
513.09	3.1	0.08	40.57	0.07
513.22	4.1	0.07	61.96	0.00
513.32	1.6	0.04	41.58	0.03
513.41	2.7	0.22	12.47	0.00
513.54	1.5	0.06	23.80	0.04
513.69	1.7	0.04	44.09	0.00
513.92	2.6	0.07	35.26	0.18

Table 4.5 Platinum group elements data for Millville.

Depth (m)	Ir (ppb)	±	Ru (ppb)	±	Pt (ppb)	±	Pd (ppb)	±
270.74	0.05	0.001	0.10	0.01	1.02	0.01	1.98	0.09
271.58	0.05	0.002	0.16	0.02	0.97	0.01	1.50	0.07
272.15	0.08	0.002	0.23	0.02	1.06	0.01	1.70	0.12
273.31	0.03	0.002	0.45	0.05	1.40	0.02	1.06	0.05
273.63	0.03	0.002	0.90	0.10	1.28	0.02	1.49	0.06
273.63 rpt	0.02	0.001	0.18	0.01	0.53	0.01	2.57	0.28
273.89	0.03	0.002	0.84	0.10	2.78	0.04	1.51	0.06
273.89 rpt	0.02	0.001	0.10	0.01	0.58	0.01	1.54	0.11
274.07	0.03	0.002	1.11	0.17	1.30	0.02	1.27	0.05
274.46	0.02	0.001	0.53	0.04	0.37	0.01	0.69	0.06
275.04	0.11	0.002	1.15	0.19	0.33	0.01	1.33	0.14
275.62	0.04	0.001	3.04	0.55	0.29	0.01	0.94	0.06

Table 4.6 Summary of the data used in quantifying the comet and associated aerosols and the results.

Parameter	Value	Reference and Comment
CI Os concentration	490 ng/g	Wasson and Kallemeyn, 1988
CI C abundance	3.2 wt. %	Wasson and Kallemeyn, 1988
CI S abundance	5.9 wt. %	Wasson and Kallemeyn, 1988
CI Ir abundance	460 ng/g	Wasson and Kallemeyn, 1988
Comet Os abundance	245 ng/g	This study
Comet C abundance	1.6 wt. %	This study
Comet S abundance	2.95 wt. %	This study
Comet Ir abundance	230 ng/g	This study
Comet mass	2.58×10^{13} kg	This study
Comet S mass	0.76 Gt	This study
Comet C mass	0.41 Gt	This study
Comet CO_2 mass	1.51×10^{15} g	assume all C release as CO_2
Comet SO_2 mass	1.52×10^{15} g	assume all S release as SO_2
Comet $^{187}Os/^{188}Os$	0.127	
Comet diameter	3.3 km	This study
Comet density	1.36 g/m^3	Kring et al., 1996
Pre-impact seawater $^{187}Os/^{188}Os$	0.38	This study
Post-impact seawater $^{187}Os/^{188}Os$	0.30	This study
Seawater mass	1.4×10^{21} kg	Ravizza, 2001
Seawater Os concentration	10 pg/Kg	Ravizza, 2001
Seawater Os mass	1.4×10^{19} ng	Ravizza, 2001
Earth surface area	5.1×10^{18} cm^2	Pidwirny, 2006
Comet induced Ir fluence	1.16 ng/cm^2	This study